

**CHARACTERIZATION AND REMOTE  
DETECTION OF ONSHORE  
HYDROCARBON SEEP-INDUCED  
ALTERATION**

**Sanaz Salati**

## **PhD dissertation committee**

### Chair

Prof.dr.ir. A. Veldkamp                      University of Twente, ITC

### Promoter

Prof.dr. F.D. van der Meer                      University of Twente, ITC

### Assistant promoter

Dr. F.J.A. van Ruitenbeek                      University of Twente, ITC

### Members

Prof.dr. C.R. de Souza Filho                      University of Campinas, Brazil

Prof.dr. S.M. de Jong                      Utrecht University

Prof.dr. S.H. Marsh                      University of Nottingham and Brit. Geol. Surv.

Prof.dr. V.G. Jetten                      University of Twente, ITC

Prof.dr. Z. Su                      University of Twente, ITC

ITC dissertation number 245

ITC, P.O. Box 6, 7500 AA Enschede, The Netherlands

ISBN: 978-90-365-3629-5

DOI: 10.3990/1.9789036536295

Printed by: ITC, Enschede, The Netherlands

© Sanaz Salati, Enschede, The Netherlands



**CHARACTERIZATION AND REMOTE  
DETECTION OF ONSHORE  
HYDROCARBON SEEP-INDUCED  
ALTERATION**

DISSERTATION

to obtain  
the degree of doctor at the University of Twente,  
on the authority of the rector magnificus,  
prof.dr. H. Brinksma,  
on account of the decision of the graduation committee,  
to be publicly defended  
on Thursday March 6, 2014 at 14.45 hrs

by

Sanaz Salati  
born on March 5, 1979  
in Tehran, Iran

This dissertation is approved by

**Prof.dr. Freek D., van der Meer**, promoter

**Dr. Frank J.A., van Ruitenbeek**, assistant promoter

## **Acknowledgements**

I have experienced an enjoyable and inspiring time during my PhD research at ITC. This dissertation could not have been completed without the support and advices that I have received from many people. I would like to take this opportunity to express my sincere appreciation to all who contributed to this dissertation.

First and foremost, I would like to extend my deepest gratitude to my promoter Prof. dr. Freek van der Meer. It has been indeed a great fortune to work with you. When I came to ITC, my knowledge about remote sensing and hydrocarbon seep was limited. Your generous support, encouragements, and patience gave me the opportunity to learn and understand various aspects of the current research. I am grateful for your insightful comments and brilliant ideas which helped me to improve this thesis at each step. I have learnt a lot from your intellectual creativity in research, immense knowledge, and working style. All lessons I have learnt from you will lighten up the way in my future career. I am truly, deeply indebted to you.

My heartfelt thanks go to my daily supervisor Dr. Frank van Ruitenbeek. You were always available to discuss the results and papers. I appreciate all your contribution of time and constructive comments to make my PhD research productive. You were patient during my learning phase and encouraging when I made progress. I enjoyed a lot working with you and I am grateful for many inspiring scientific discussions we shared. Special thanks to Dr. Majid Tangestani for his support and continuous encouragement throughout my PhD duration. I appreciate your help during the field work and your valuable contributions in two chapters of this thesis.

I would like to pay my sincere appreciation to Boudewijn de Smeth for his valuable friendship, support, advices, and fruitful comments. I had an excellent working experience in the geochemical laboratory and your devoted working style speeded up my research. Your contribution to this dissertation has been great of value. I am grateful for the strict and valuable comments from Dr. John Carranza. You have been an excellent co-author and a good friend.

I would like to acknowledge the Erasmus Mundus, ITC research fund, and ITC foundation for granting me scholarship, the Shiraz University for providing field facilities, and the Iranian oil company for providing geological maps and information on the location of hydrocarbon seeps. My heartfelt appreciation to Loes Colenbrander, Christie Agema, Theresa van den Boogaard, Marie Chantal Metz, Bettine Geerdink, Roelof Schoppers, Aiko Mulder, Henk Wilbrink, and Marion Pierik for their care and facilitating various issues, which made my life comfortable at ITC.

I could not complete this dissertation without the support of my amazing friends. My heartfelt thanks go to Shirin and Babak for their endless support.

You are an awesome couple. Without your company, I could not pass all those difficult times in my life. Babak, I enjoyed our statistical discussions and I have learnt a lot from you. Shirin, no matter where you have been in this globe, you have always comforted me and made me feel confident. I am deeply grateful for your care and all joyful moments we shared. I would like to extend my deepest appreciation to my dearest friends Xuanmei and Fangyuan for their care, support, company, and sharing life and its adventure. You have been such amazing friends always been there for me. Special thanks to Sharon and Divyani for their valuable friendship and company. I have been fortunate to come across wonderful office mates. Thank you Irena for becoming a very good friend in such a short time and have given me all your support. I am grateful to Marshall and Pablo for their lifelong friendship and sharing many interesting discussions.

Many thanks to Abbas and Sonya for their friendship and making us Persian dishes made me feel home. Special thanks to David for being a good friend and taught me many new things, to Tina for her friendship and her company to find “hot spots” for shopping and eating, to my dear friends Farhang, Aidin, Maral, and Sam for enjoyable moments and yummy foods. Many thanks to Sara, Shadi, Diego, Nick, Anandita, Jack, Martia, Matthew, Otto, Tolga, Hale, Mostafa, Sedighe, Goli, Petra, Amir, Pejman, Hadi, Sonya, Yijian, Chenxiao, Mitra, Razieh, Tanmoy, Nas, Armindo, Maria, Beti, Islam, Effie, Thea, Parinaz, Elnaz, Leila, and John.

My wholeheartedly thanks to my dear mom and my beloved dad who died two years ago. . . . I miss you dad. Without your love and support my life would be a bleak. I am deeply grateful for what you have taught me in life and for letting me go after my wishes. To Zamyad, Hana, Ayda, and Aryanaz for your love and encouragements.

## Contents

List of figures .....	vi
List of Tables .....	v
<b>1. Introduction .....</b>	<b>1</b>
1.1. Problem statement .....	2
1.2. Hydrocarbon seeps and associated alteration.....	3
1.3. Remote sensing of seep-induced alteration.....	4
1.4. Research objectives .....	5
1.5. Study area .....	5
1.5.1. Regional geology .....	6
1.5.2. Petroleum geology .....	7
1.6. Structure of the thesis .....	9
<b>2. Remote sensing of onshore natural hydrocarbon seep-induced alteration .....</b>	<b>11</b>
2.1. Introduction .....	12
2.2. Classification of hydrocarbon seeps at the surface .....	13
2.3. Migration pathways of hydrocarbon seeps .....	14
2.4. Alterations induced by hydrocarbon seeps .....	15
2.5. Remote sensing studies of onshore hydrocarbon seep-induced alteration .....	17
2.6. Discussion and conclusions .....	19
<b>3. Conceptual modelling of onshore hydrocarbon seep occurrence in the Dezful Embayment, SW Iran .....</b>	<b>23</b>
3.1. Introduction .....	25
3.2. Hydrocarbon seeps in the Zagros belt.....	26
3.3. Methods .....	26
3.3.1. Analysis of spatial pattern of hydrocarbon seeps.....	27
3.3.2. Analysis of spatial association between hydrocarbon seeps and geological features .....	29
3.4. Results .....	32
3.4.1. Spatial patterns of hydrocarbon seeps.....	32
3.4.2. Spatial associations of hydrocarbon seeps with structural units .....	35
3.4.3. Spatial association of hydrocarbon seeps with lithological units.....	38
3.4.4. Spatial association of sub-sets of hydrocarbon seeps with structures only in lithological units having positive spatial association .....	40
3.5. Conceptual modeling of occurrence of hydrocarbon seeps in the Dezful Embayment .....	48
3.6. Discussion.....	50
3.7. Concluding remarks.....	51
<b>4. Spectral and geochemical characterization of onshore hydrocarbon seep-induced alteration in the Dezful Embayment, SW Iran .....</b>	<b>53</b>
4.1. Introduction .....	55
4.2. Materials and methods.....	56
4.2.1. Field sampling.....	56
4.2.2. Spectral analysis .....	57

4.2.3. Statistical analysis of spectra .....	58
4.2.4. Geochemical analyses .....	59
4.3. Results .....	60
4.3.1. Characterization of gas seep-induced alteration .....	60
4.3.2. Characterization of oil seep-induced alteration .....	66
4.3.3. Identifying the origin of hydrocarbon seeps by isotopic analysis .....	72
4.4. Discussion .....	75
4.5. Conclusion .....	76
<b>5. Detecting mineralogical boundary of evaporite cap rock using rotation variant template matching .....</b>	<b>79</b>
5.1. Introduction .....	81
5.2. Test area .....	83
5.3. Methods .....	84
5.3.1. RTM algorithm .....	84
5.3.2. Aster data analysis .....	86
5.3.3. Assessment of the spatial accuracy of detected boundaries .....	87
5.4. Results .....	90
5.4.1. Image analyses .....	90
5.4.2. RTM algorithm .....	91
5.4.3. Assessment of the spatial accuracy of detected boundaries .....	95
5.5. Discussion .....	100
5.6. Conclusion .....	102
<b>6. Detecting onshore gas seep-induced alteration from ASTER and WorldView-2 data .....</b>	<b>103</b>
6.1. Introduction .....	105
6.2. Hydrocarbon seep-related alterations in the Mishan marly limestone .....	106
6.3. Remote sensing data .....	108
6.3.1. ASTER data .....	108
6.3.2. Worldview-2 data .....	108
6.3.3. Spectral measurements .....	109
6.4. Methods .....	109
6.4.1. ASTER data processing .....	109
6.4.2. WorldView-2 data processing .....	111
6.4.3. Data integration .....	111
6.4.4. Boosted regression trees classification (BRT) .....	111
6.5. Results .....	113
6.5.1. ASTER data processing .....	113
6.5.2. WorldView-2 .....	117
6.5.3. The BRT classification .....	119
6.6. Discussion .....	124
6.7. Conclusion .....	126
<b>7. Synthesis .....</b>	<b>127</b>
7.1. Introduction .....	128
7.2. Spatial pattern of hydrocarbon seeps .....	128
7.3. Field and laboratory studies .....	129

7.4. Spaceborne study .....	130
7.5. Hydrocarbon seep and alteration; progress made .....	132
7.5.1. Understanding the relationship between the geology and hydrocarbon seeps .....	132
7.5.2. More benefits from remote sensing studies to the oil and gas industry .....	133
7.6 Future work.....	136
Bibliography .....	139
Summary .....	155
Samenvatting .....	157
Biography .....	159
Publications .....	159
ITC Dissertation List .....	162

## List of figures

<b>1.1:</b> Alteration induced by gas seeps in the Gachsaran Formation, SW Iran. ....	3
<b>1.2:</b> Structural setting of the Zagros Fold including locations of oil and gas fields .....	7
<b>1.3:</b> Stratigraphy of sedimentary rocks in the Zagros belt.....	9
<b>1.4:</b> Distribution of hydrocarbon seeps in the Zagros belt and locations of study areas in the various chapters.....	10
<b>2.1: (a)</b> Alteration induced by hydrocarbon microseeps in Wintage sandstones. <b>(b)</b> Unaltered Wintage sandstone, Lisbon Valley, Utha, USA. <b>(c)</b> Bleached and unbleached red beds of Dushanzi anticline and the presence of oil macroseeps in the Tian Shan Mountains, China. ....	16
<b>2.2:</b> Generalized model of hydrocarbon geochemical alteration of sediments adopted from.....	17
<b>2.3:</b> Global distribution of petroleum seeps (Etiopie, 2009) and approximate locations of onshore seep related alterations studied by remote sensing. ....	20
<b>3.1:</b> Distribution of faults, anticline axes, and hydrocarbon seeps in the study area. ....	28
<b>3.2:</b> Distribution of hydrocarbon seeps, source rocks, reservoirs, cap rock and the Mishan Formation. ....	29
<b>3.3:</b> Fry plots and trends of pairs of Fry points of locations mapped hydrocarbon seeps. ....	33
<b>3.4:</b> Fry plots and trends of pairs of Fry points of locations mapped heavy oil or asphalt seeps. ....	34
<b>3.5: (A)</b> Fry plots and trends of pairs of Fry points of locations mapped Gach-e-Tursh. <b>(B)</b> Fry plots and trends of pairs of Fry points of locations mapped sulphur springs. ....	35
<b>3.6:</b> Graphs of cumulative relative frequency of distances at seep locations (D (M)) and non-seep locations (D (N)) around structural units in the Dezful Embayment. D and u D (N) represent spatial association of seeps with structures and confidence band for $\alpha=0.01$ respectively.....	37
<b>3.7:</b> Graphs of cumulative relative frequency of distances at heavy oil or asphalt seep locations (D (M)) and non-heavy oil or asphalt locations (D (N)) around structural units of the three Formations and corresponding graphs of $\beta$ -statistics of differences (D) between the cumulative relative frequency curves, the Dezful Embayment. D and u D (N) represent spatial association of seeps with structures and confidence band for $\alpha=0.01$ respectively.....	41
<b>3.8:</b> Graphs of cumulative relative frequency of distances at heavy oil or asphalt seep locations (D (M)) and non-heavy oil or asphalt locations (D (N)) around thrust faults of three Formations and corresponding graphs of $\beta$ -statistics of differences (D) between the cumulative relative frequency curves, the Dezful Embayment. D and u D (N) represent spatial association of seeps with structures and confidence band for $\alpha=0.01$ respectively.....	42
<b>3.9:</b> Graphs of cumulative relative frequency of distances at Gach-e-tursh locations (D (M)) and non-seep locations (D (N)) around structural units of the Gachsaran and Mishan Formations and corresponding graphs of $\beta$ -statistics of differences (D) between the cumulative relative frequency curves, the Dezful Embayment. D and u D (N) represent spatial association of seeps with structures and confidence band for $\alpha=0.01$ respectively.....	45

<b>3.10:</b> Graphs of cumulative relative frequency of distances at sulphur springs locations (D (M)) and non-seep locations (D (N)) around structural units of the Gachsaran and Mishan Formations and corresponding graphs of $\beta$ -statistics of differences (D) between the cumulative relative frequency curves, the Dezful Embayment. D and u D (N) represent spatial association of seeps with structures and confidence band for $\alpha=0.01$ respectively.....	46
<b>3.11:</b> Conceptual model for the occurrence of onshore hydrocarbon seeps and their alteration products in the Dezful Embayment. ....	50
<b>4.1:</b> Typical gas (a and b) and oil (c and d) seeps in the Gachsaran and Mishan Formations in the Dezful Embayment, SW, Iran. ....	56
<b>4.2:</b> Sampling profiles over gas seeping area (a and b) and over oil seeping area (c and d). ....	57
<b>4.3:</b> Characteristic reflectance spectra and spectral parameters of altered and unaltered the Gachsaran evaporites.....	61
<b>4.4:</b> ROC curve of the predictive power of the BRT model on the presence/absence of gas-induced alterations and relative influences of absorption features on prediction models in the Gachsaran evaporites. ....	62
<b>4.5:</b> Box plots of major oxides and sulfur (S) concentrations in the Gachsaran evaporite samples including gas-induced alteration samples and statistical comparison (t-test) between elemental concentrations from altered and unaltered Gachsaran evaporites. ....	62
<b>4.6:</b> Characteristic reflectance spectra from the gas-induced alterations and unaltered Mishan marly limestone.....	64
<b>4.7:</b> ROC curve of the predictive power of the BRT model on the presence/absence of gas-induced alterations and relative influences of absorption features on prediction models in the Mishan marly limestone.....	65
<b>4.8:</b> Box plots of XRF measured CaO, S, and wet chemical measured gypsum and calcite, and statistical comparison (t-test) between elemental concentrations from altered (marly limestone affected by gas seep) and unaltered Mishan marly limestone. ....	66
<b>4.9:</b> Characteristic reflectance spectra from oil-induced alterations and unaltered Gachsaran evaporites.....	68
<b>4.10:</b> ROC curve of the predictive power of the BRT model on the presence/absence of oil-induced alterations and relative influences of absorption features on prediction models in the Gachsaran.....	69
<b>4.11:</b> Box plots of gypsum and calcite concentrations measured by wet chemical analysis and statistical comparison between major oxides and elemental concentrations from altered (evaporites affected by oil seeps) and unaltered Gachsaran evaporites. ....	70
<b>4.12:</b> Characteristic reflectance spectra from oil-induced alterations in the Mishan Formation and characteristic marly limestone spectrum. ....	71
<b>4.13:</b> Box plots of Cao and K <sub>2</sub> O and statistical comparison between major oxides from unaltered marly limestone and oil seep-induced alterations of Mishan marly limestone.....	72
<b>4.14:</b> (a) Sulfur isotopic composition of altered and unaltered evaporites (affected by gas seep). (b) Sulfur isotopic composition of altered and unaltered marly limestones (affected by gas seep). ....	74
<b>4.15:</b> (a) Carbon and oxygen isotopic composition of altered and unaltered evaporites (affected by oil seep). (b) Carbon and oxygen isotopic composition of altered and unaltered marly limestones (affected by oil seep). ....	75

<b>4.16:</b> Generalized models of oil and gas seeps-induced spectral and geochemical alterations within the evaporites and the marly limestone formations.....	76
<b>5.1:</b> (a) An ASTER (RGB: 468) false color composite image of the study area. (b) Geological map of study area derived from the geological map of the Gachsaran .....	84
<b>5.2:</b> (a) Template design of 5×1 pixels including center pixel (cp); (b) moving over an image; and (c) rotating at every position.....	85
<b>5.3:</b> (a) False color composite (FCC) created from RBD and band ratio images; (b) Image-based stratigraphic column, indicates distributions of minerals. (c) SWIR image mean spectra and the JPL re-sampled library. ....	91
<b>5.4:</b> (a) and (b) Color composite images produced from RTM outputs.....	93
<b>5.5:</b> Profiles of outputs of the RTM algorithm .....	94
<b>5.6:</b> Lithological boundaries interpreted by five experts .....	96
<b>5.7:</b> Rotation variance ( $v_r$ ) images for the template gypsum-calcite. (a) and calcite-illite. (b) as processed by Getis-Ord local spatial autocorrelation. (c) Extracted boundary pixels detected between evaporites and marly-limestone. (d) Extracted detected boundary pixels between marly-limestone and sandstone.....	97
<b>5.8:</b> (a) Fuzzy assessment of spatial accuracy of the detected boundary between the Mishan and Aghajari Formations and the geological map. (b) Fuzzy assessment of spatial accuracy of the detected boundary between the Mishan and Aghajari Formations the map derived from aerial-photo interpretation. (c) Fuzzy membership scores assigned to the cumulative percentage of the detected pixels. ....	99
<b>5.9:</b> (a) Fuzzy comparison of detected boundary between Mishan and Gachsaran units with the geological map. (b) Fuzzy comparison of detected boundary between Mishan and Gachsaran units with the map derived from aerial photo interpretation. (c) Fuzzy membership scores assigned to the cumulative percentage of the detected pixels. ....	100
<b>6.1:</b> (a) Geological map of the study area overlaid on the hill-shaded ASTER GDEM. (b) An ASTER (RGB:468) false color composite image of the study area.....	107
<b>6.2:</b> A photo of the studied area shows the alteration zone and unaltered marly limestone and the generalized model of spectral and geochemical signatures of gas-induced alterations in the Mishan Formation.....	108
<b>6.3:</b> (a) Spectral reflectance curves for selected marly limestone and altered marly limestone from the Mishan Formation resampled to the ASTER imagery and pseudo reflectance spectra of ASTER pixels co-located with field sampling points. (b) FCC of the ASTER overlaid by lithological boundaries. Band combination used is (RGB) 4-6-8. (c) Enlargement showing location of field measurements.....	114
<b>6.4:</b> (a) Mean spectra derived from ASTER imagery compared to the USGS spectral library re-sampled to the ASTER. (b) FCC image created from ASTER bands.....	115
<b>6.5:</b> (a) False color composite created from RBD and band ratios: $b_4/(b_6+b_9)$ for enhancing gypsum (Red), $(b_7+b_9)/b_8$ for enhancing calcite (Green), and $(b_5+b_7)/b_6$ for enhancing clays (Blue). (b) False color composite created from $b_4/(b_6+b_9)$ for enhancing gypsum (Red), $b_4/b_3$ for enhancing ferric iron (Green), and $b_3/b_1$ for enhancing ferrous iron.....	116
<b>6.6:</b> (a) False color composite created from pan-sharpened ASTER VNIR bands (15 m resolution) with WV2 0.5 m panchromatic image, (b) false color composite created from ASTER SWIR bands with WV2 0.5 m panchromatic image .....	116

<b>6.7:</b> (a) Color composite image (R: 6, G: 3, B: 2) created from WV-2 imagery. (b) Enlargement showing location of field measurements. (c) Mean spectra derived from image pixels covering field data. ....	118
<b>6.8:</b> (a) FCC image created from band 2/band1 (in red), band5+band3/band1 (in green), and band4/band7 (in blue); (b) illustrates a FCC of PCA123 from WV2 bands. Red ellipses surround alteration zones and black lines display lithological boundaries; (c) shows the geological map of the study area. ....	119
<b>6.9:</b> (a) Results obtained by the BRT classification with end-members extracted from the purest image pixels of ASTER. (b) Geological map of the study area. ....	120
<b>6.10:</b> (a) Results obtained by the BRT classification with end-members extracted from the purest image pixels of WV-2. (b) BRT classification using ROIs co-located with ground samples. (c) Geological map of the study area. ....	121
<b>6.11:</b> Results obtained by BRT classification of multiple band imagery created from ASTER and WV-2. (a) The BRT classification using ROIs co-located with the purest pixels of ASTER. (b) The BRT classification using ROIs co-located with the purest pixels of WV-2. (c) The BRT classification using ROIs co-located with sampling points. (d) The geological map of the study area. ....	123
<b>7.1:</b> ASTER color composite of Masjid-Soleyman oil field. ....	134
<b>7.2:</b> ASTER color composite of Gachsaran oil field. ....	135
<b>7.3:</b> A schematic model of influence of cap rock heterogeneity on the type of hydrocarbon seeps occur at the surface. ....	136

## List of Tables

<b>2.1</b> Displays remote sensing data and image processing techniques applied to map hydrocarbon seep-induced alterations in sediments.na=not available.....	19
<b>3.1</b> Variation of weights and contrasts for lithologic units with respect to (a) heavy oil or asphalt seeps; (b) Gach-e-tursh; and (c) sulphur springs.....	38
<b>3.2</b> Summary of statistically significant results of analyses of spatial associations between each sub-set of hydrocarbon seeps and individual sets of structural features of the Formations having positive spatial associations with seep.....	47
<b>6.1</b> ASTER band ratios for enhancing mineral features.....	110
<b>6.2</b> Relative contributions (%) of predictor variables and AUC values for the BRT classifications of various scenarios.....	124

# ***1.* Introduction**

### **1.1. Problem statement**

Due to high pressures at depths, hydrocarbons in the subsurface can escape to the surface through fractures in rocks and planes of weakness between geological layers. Petroleum and gas seeps on the surface are direct indicators of accumulations of hydrocarbons in the subsurface and could reflect the migration of hydrocarbons in a sedimentary basin. Natural hydrocarbon seeps are of interest for hydrocarbon exploration. The presence of seeps at the surface is not indicative of the size of a petroleum basin and they may even be located over a non-productive basin. However, it is an indirect evidence of the presence of mature source rocks within a geological system at depth. Furthermore, hydrocarbon seeps are natural sources of gases, which contribute to the greenhouse effect (Moore, 1999).

Escaped hydrocarbons from subsurface reservoirs, either as visible (macroseeps) or invisible (microseeps), change the oxidation-reduction environment at the surface and thereby initiate diagenetic Eh/pH controlled reactions in the rocks and soils. Such changes are favor the formation of mineralogical alterations such as red beds bleaching, clays formation, and formation of secondary carbonates, sulfides, and magnetic minerals (Schumacher, 1996). Hydrocarbon seep-induced alterations have long been popular in petroleum exploration methods but such alterations and processes that cause them are not well-documented in many of petroleum basins especially in the Middle East, which provides most of the oil and gas in the world. In addition, most studies on hydrocarbon seep related alterations have focused on detection of such alterations aimed at confirmation of hydrocarbons generation at the subsurface. Less attention has been paid to the value of alterations on petroleum system evaluation such as getting a better understanding of hydrocarbon seeps migration pathways and permeability of cap rocks at a regional scale in onshore basins. Characterization of hydrocarbon seep-induced alteration within a petroleum basin would allow us to map spatial distributions of those alterations, which could be analogous to the spatial pattern of alterations in the subsurface. Such studies provide a framework for identifying permeable zones and evaluating the efficiency of cap rocks related to petroleum systems.

We are concerned here with the evaluation of the importance of onshore hydrocarbon seeps and their associated alterations in better understanding of oil/gas migration to the surface in relation with various types of seeps. Study of alterations induced by active seeps provides valuable information about the subsurface migration and permeability of cap rocks and brings important clues as to the nature of microseeps. The emphasis of this thesis is on the geological application of reflectance spectroscopy and multispectral image analyses that allow detection of seep-induced alterations and petroleum basin evaluation.

Integration the results obtained from remote sensing studies with geological and geochemical data would allow us to understand processes that caused alterations at the surface.

## 1.2. Hydrocarbon seeps and associated alteration

Hydrocarbon seeps and their surface expressions are commonly found throughout the world in sedimentary basins containing oil and gas reserves. Hydrocarbon macroseeps manifest themselves as the visible presence of oil and gas seeping to the surface; while hydrocarbon microseeps have no visible and direct evidences for their presence, seeping probably occurs vertically or near-vertically from the reservoir to the surface (Abrams, 2005). The presence of hydrocarbon macroseeps (Figure 1.1b) at the surface is direct evidence of hydrocarbon migration in a separate phase. As hydrocarbon moves to the surface, they re-equilibrate to oil and gas. They can be in contact but are often segregated due to different migration pathways such as spillage of oil, capillary leakage of oil and gas, trapping configuration, and cap rock behavior (Matthews, 1996). At the surface, escaped hydrocarbons oxidize and form reducing environment that favor the formation of mineralogical and botanical anomalies. In addition, slightly acidic conditions are created due to the production of  $\text{CO}_2$ ,  $\text{H}_2\text{S}$ , and organic acids (resulted from microbial oxidation of hydrocarbons). Depending on the chemical composition of the surface rocks mineralogical alterations occur in a basin such as red beds bleaching and clay formation, as well as formation of secondary carbonates, sulfides, and magnetic minerals (Schumacher, 1996) (Figure 1.1a).

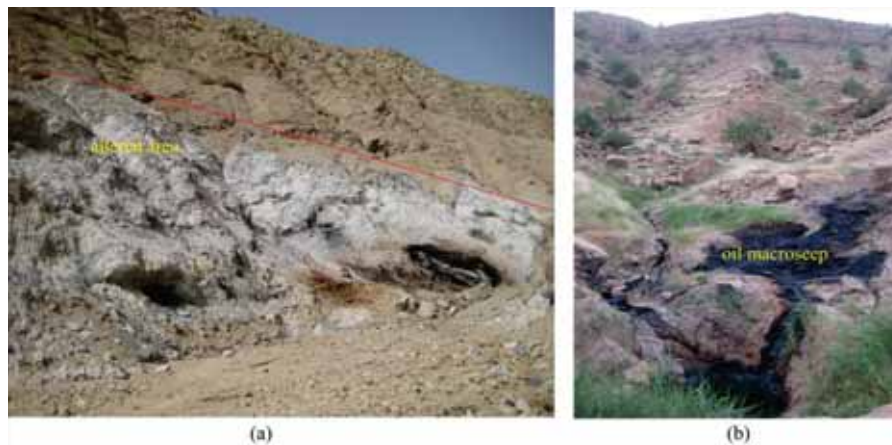


**Figure 1.1:** (a) Alteration induced by gas seeps in the Gachsaran Formation, SW Iran. (b) Presence of oil macroseep in the Gachsaran evaporite formation, SW Iran.

### **1.3. Remote sensing of seep-induced alteration**

On land, hydrocarbon seep-induced alteration has been widely studied by traditional techniques such as geochemical and geophysical analyses. These methods are expensive, and time consuming and only applicable to some observations collected in the field mainly around drilling areas in active petroleum fields. Thus, they cannot be used for mapping alterations and their variations related to different types of seeps and various host lithologies over a large area. Remote sensing holds a great promise as a rapid and cost effective tool for detection hydrocarbon seeps induced alterations. The use of remote sensing techniques for direct detection of hydrocarbon from seeps is problematic but it could be used for detection of indirect evidences which induced by hydrocarbon seeps. The interpretation of remotely sensed image cannot reveal depth, size, quality, and presence of hydrocarbon in reservoirs, but it is cost effective and could increase the probability success in exploration (Saunders et al., 1999). In the VNIR and SWIR bands, iron bearing minerals, carbonates, hydrate and hydroxide minerals such as gypsum and clays display molecular absorption features related to their overtones and combination tones (Hunt, 1977). Those minerals are some of the most common alteration related minerals induced by hydrocarbon seeps (Schumacher, 1996).

Airborne and multispectral remote sensing data such as HyMap and the Advanced Spaceborne Thermal Emission and Reflection Radiometer (ASTER) have been applied to map hydrocarbon seep-induced alterations mostly in sandstone formations of petroleum basins in United State, Brazil, and China (Bowen et al., 2007; Filho, 2002; Khan and Jacobson, 2008; Lammoglia and Filho, 2013; Lammoglia et al., 2008; Petrovic et al., 2008; Petrovic et al., 2012; Shi et al., 2012; van der Meer et al., 2002). To date, no attempt has been made to map hydrocarbon seep related alterations in petroleum basins with different lithologies than sandstone from remote sensing data. In addition, high spatial resolution data with multispectral bands in VNIR, which can be used to mapping the bleaching effects of hydrocarbon seeps at the surface, have been overlooked from remote sensing studies of such alterations. Iron bearing minerals are some of the most common alteration related minerals in bleached areas affected by seeps, which display distinctive spectral features in VNIR wavelengths.

Spectral resolution is the main support in image classification; however, spatial resolution is the main factor in recognition accuracy of the ground objects. Ground control points are needed to provide provision of spatial context of minerals identified with image classification techniques. In areas with spare ground data, it is difficult to provide spatial correspondence between minerals identified from image and field measurements because these measurements may cover few pixels of the imagery. One promising approach in image classification is integrating high spectral resolution data with high spatial

resolution data to solve this challenging task. Integration of ASTER and WorldView-2 (WV2) data for mineral classification would allow us to understand if spatial resolution of WV2 and its multispectral bands in VNIR have any impacts on classification of target minerals.

#### **1.4. Research objectives**

The general objectives of the research presented in this thesis are spectral and geochemical characterization of alteration induced by two subsets of hydrocarbon seeps in evaporite and marly limestone formations at a regional scale and detection of those alterations with remote sensing image. The following objectives are defined:

- Modelling of the occurrence of hydrocarbon seeps in relation to their associations with geological features at a regional scale.
- Spectral and geochemical characterization of alterations associated with different type of seeps (oil and gas) and various lithologies and getting a better understanding of oil and gas migration through the stratigraphy in relation to the various types of seeps in the Zagros belt.
- Mapping boundaries between zones of compositional variations within evaporite cap rock in the Zagros petroleum system with ASTER imagery using a mineralogical boundary detection algorithm, named Rotational Template Matching (RTM).
- Detection of hydrocarbon seep-induced alteration from multispectral ASTER and high spatial resolution WV- 2 data and explore the potential of using high spatial resolution WV-2 imagery for mapping the alteration zone and improving the accuracy of mapping.

#### **1.5. Study area**

The study area is located in the Zagros fold-thrust belt, SW Iran. The co-existence of rich source rocks, excellent reservoirs, efficient seals, large anticlines and rock fractures resulting from the Zagros folding make the Zagros fold-thrust belt an important petroleum province (Bordenave and Hegre, 2005). At least 40-50% of Iranian seeps in the SEEPS database, which was produced by the British Petroleum and described by Clark and Cleverly (1991), can be linked to underlying hydrocarbon accumulations (MacGregor, 1993). The presence of hydrocarbon seeps led to the discovery of the subsurface petroleum in the SW Iran in early 1900s. There are different types of hydrocarbon seeps in the Zagros fold-thrust belt, such as crude oil, heavy oil or asphalt, gas, gas/oil. Gach-e-tursh and sulphur springs are products of the subsurface alteration processes of gas seeps (Clarke and Cleverly, 1991), which are common in the Dezful Embayment. The term Gach-e-tursh, which was introduced by Thomas

(1952), refers to an association of petroleum seep, gypsum, jarosite, sulphuric acid, and sulphur.

### **1.5.1. Regional geology**

The Zagros fold-thrust belt resulted from the continental collision between the Arabian plate and Iranian block (Berberian and King, 1981). This compressive movement began during Late Cretaceous and became widespread following the continent-continent collision in Miocene, which is still active in N-S direction (Falcon, 1974; Sella et al., 2002; Stocklin, 1968). The convergence direction is oblique to NW-SE trend of the orogenic belt. The Zagros fold-thrust belt, which lies south of the Zagros suture (Figure 1.2), is divided into NW-SE trending structural zones (imbricated and simply folded belt) and laterally divided to Lurestan, Dezful embayment and Fars region (Berberian and King, 1981; Carruba et al., 2006; Falcon, 1974; Motiei, 1993; Sherkati and Letouzey, 2004; Stocklin, 1968).

The Dezful Embayment, situated in the central-southern part of the Zagros fold-thrust belt (Figure 1.2), hosts most of the onshore hydrocarbon reservoirs of Iran. This area, which is situated southwest of the Mountain Front Fault (MFF), is dominated by NW-SE trending folds and thrusts. The NW boundary of the Dezful Embayment coincides with the Balarud fault zone (BFZ) and its SE boundary is defined by the Kazerun fault zone (KFZ). The NE-SW-trending BFZ, the N-S-trending KFZ and Izeh fault zone (IFZ), and the NW-SE-trending MFF are seismically active (Berberian, 1995) and have significant influence on hydrocarbon migration and entrapment in the Zagros fold-thrust belt (Beydoun et al., 1992; Bordenave and Hegre, 2005; Hessami et al., 2001; McQuillan, 1991).

The stratigraphy of the study area (Figure 1.3) is defined by a competent group formed by a structural unit between the lower detachment or lower mobile group (the Hormuz salt) and the upper detachment or upper mobile group (the Gachsaran evaporites) (O'Berian, 1957). Salt tectonic played an important role in hydrocarbon migration and entrapment in the Dezful Embayment (Berberian, 1995). The mobile Gachsaran Formation migrated from the crest of anticlines downward and accumulated within synclines, accentuating the asymmetry of the whole structure (Sherkati et al., 2005). This deformation caused severe disharmony between surface structures and the underlying structures (Abdollahi Fard et al., 2011; Alavi, 2004; Bahroudi and Koyi, 2004; Gill and Ala, 1972; Kashfi, 1980; Motiei, 1993; O'Berian, 1957; Sherkati and Letouzey, 2004; Sherkati et al., 2005).

The ongoing late Tertiary folding concurrent with deposition, means that the lower member of the Gachsaran Formation (seal) thin as they overlap and wedge out onto growth folds in the Asmari reservoir (Alavi, 2004; Warren,

2006). The base of the Gachsaran Formation forms a major décollement, which shows the repetition by faulting. Several thrusts produced by slip on the basal Gachsaran Formation displace the Gachsaran evaporites and its overlying units (Alavi, 2004).

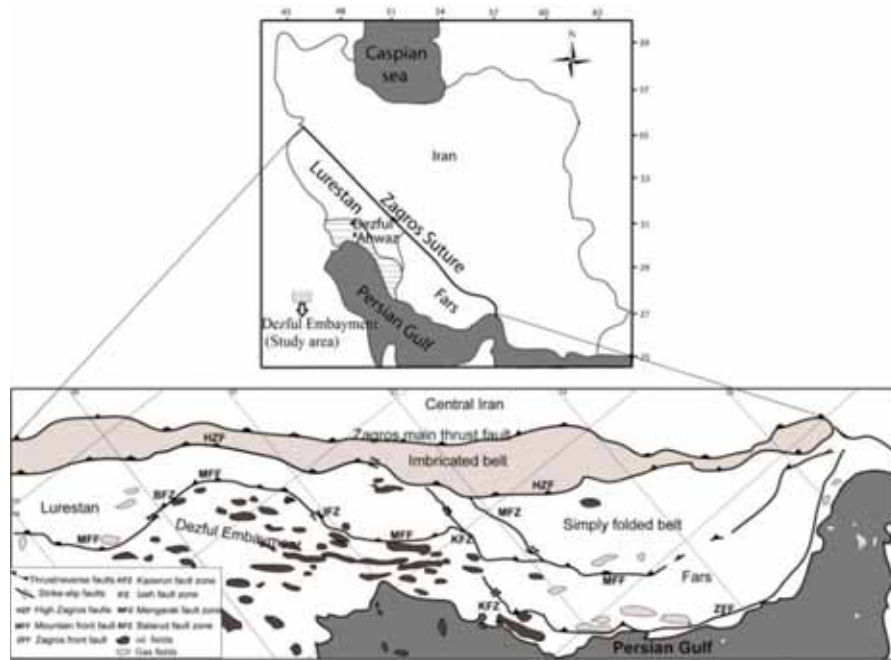


**Figure 1.2:** Structural setting of the Zagros Fold including locations of oil and gas fields (Sepehr and Cosgrove, 2004).

### 1.5.2. Petroleum geology

The Cretaceous to Early Miocene shallow petroleum system of the Dezful Embayment is one of the world richest oil fields because it contains about 8% of global oil reserves (Bordenave and Hegre, 2010). This petroleum system comprises two source rocks including the Kazhdumi and the Pabdeh Formations, two reservoirs including the Asmari and the Sarvak Formation, and two seals including the Gachsaran and the Gurpi Formations.

The Albian Kazhdumi (Kz) Formation consists of bituminous shale with argillaceous limestone. Except in oil fields to the NE of the Dezful Embayment, most of the oil accumulated in the Asmari/Sarvak reservoirs originated from the Kz Formation (Bordenave and Hegre, 2010). The Eocene Pabdeh (Pd) Formation is composed of marls, shales, and carbonates, all rich in pelagic micro-fauna. Recent studies showed that most parts of the Pd Formation, including its limestone beds, were deposited in a ramp environment. The Pd

separates the structural traps of the Cretaceous Bangestan Group from the overlying Asmari Formation (Bordenave and Hegre, 2010).

The Asmari Formation contains 75% of the onshore hydrocarbon reserves. Fractures resulting from the Zagros folding enhanced the quality of this limestone reservoir by facilitating the expulsion of oil from source rocks in anticline areas (Bordenave and Hegre, 2005). The Sarvak Formation, which is the second major reservoir, accounts for 23% of hydrocarbon reserves in the Dezful embayment. The Sarvak Formation is often interconnected to the Asmari Formation in high-relief often thrust anticlines and have the same oil water level because of the fracturing of the Pabdeh-Gurpi marls in the crestal part of the anticlines (Bordenave and Hegre, 2005). The Asmari reservoir is sealed by the Gachsaran evaporites. The Gachsaran Formation exhibits rhythmic bedding consisting of bluish-green marl, limestone, dolomite and anhydrite, with/without bedded salt (Gill and Ala, 1972; Motiei, 1993). The Sarvak reservoir is sealed by the Gurpi Formation, which is dominated by marl and thin interlayers of limestone.

Oil migrated from the source rocks through structures formed during the Zagros folding around 10 Ma ago and continued throughout the Late Miocene and Pliocene. Oil expulsion from the Kz and Pd began between 8 Ma and 3 Ma ago during deposition of the Aghajari Formation (Bordenave and Hegre, 2010). Oil expulsion from the source rocks was also coeval with the formation of the Zagros folds such that hydrocarbons migrated almost vertically to reserves in neighboring anticlines. High pressure in pore spaces of the Kz formed a barrier, however, and prevented oil generated in deeper source rocks from reaching the reservoirs (Bordenave and Hegre, 2010). Oil was expelled from the Pd only in the deeper part of some of synclines, which represent less than 1% of the total oil expelled (Bordenave and Hegre, 2005).

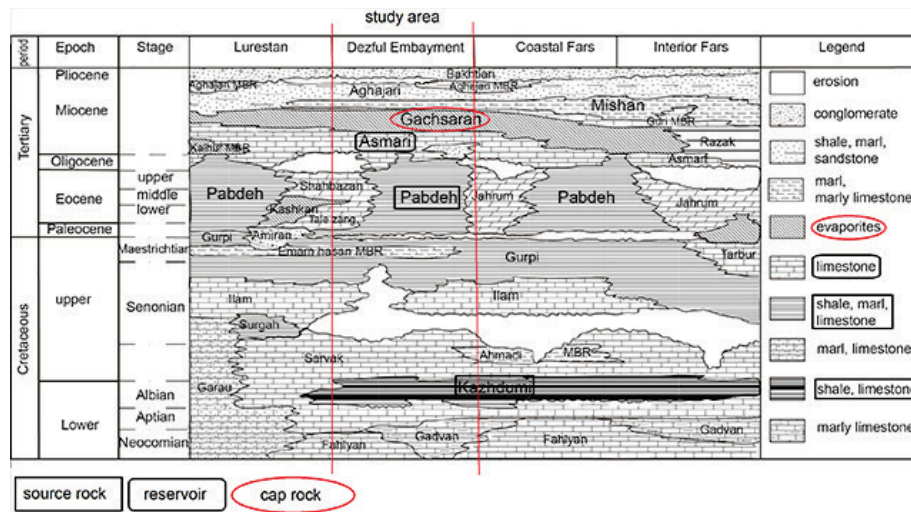


**Figure 1.3:** Stratigraphy of sedimentary rocks in the Zagros belt (James and Wynd, 1965).

## 1.6. Structure of the thesis

This thesis consists of a total seven chapters. Apart from the introduction and synthesis chapters, the five chapters have either been published in peer-reviewed journals (chapters 3, 4, 5, and 6) or are for submission (chapters 2). Figure 1.4 shows the locations of test areas for each chapter.

Chapter 2 reviews previously published remote sensing studies on hydrocarbon seep-induced alteration. The chapter defines the successes, limitations and present state of the art in seep-induced alteration research guides the research directions of following chapters.

Chapter 3 describes quantitatively the spatial pattern and spatial distribution of oil/gas seeps and their associated alterations with geological features. This chapter provides insights about (a) links between geological structures and two subsets of hydrocarbons seeps and (b) the probability of spatial association of different geological features with two sub-sets of seeps. The results from this chapter help to select study areas for field observations.

Chapter 4 analyses the spectral and chemical characteristics of alteration induced by hydrocarbon seep from field data in order to (a) getting a better understanding of oil and gas migration through the stratigraphy in relation to the various types of seeps in the Zagros belt and (b) investigate the potential of detection of hydrocarbon seep-induced alteration for petroleum explorations. The results from this chapter help to select the best suitable test area for image

processing and to extract end-members from field observations to aid in image processing.

Chapter 5 applied a template matching algorithm to ASTER data. The algorithm has been developed by van der Werff et al (2007) to detect mineralogical boundaries in a hydrothermal system. In this research, the RTM algorithm is used to map boundaries between zones of compositional variations within evaporite cap rock in the Zagros petroleum system with ASTER imagery.

Chapter 6 investigates whether high spatial resolution WV2 satellite imagery and multispectral ASTER are able to detect gas-induced alterations in the Mishan marly limestone Formation. This chapter describes the integration of ASTER and WV2 data for mineral classification and investigates if spatial resolution of WV2 and its multispectral bands in VNIR can improve the accuracy of classification of target minerals.

Chapter 7 provides a summary of obtained results of previous chapters 2 to 6 and discusses the outcomes and their implications for petroleum exploration campaigns.

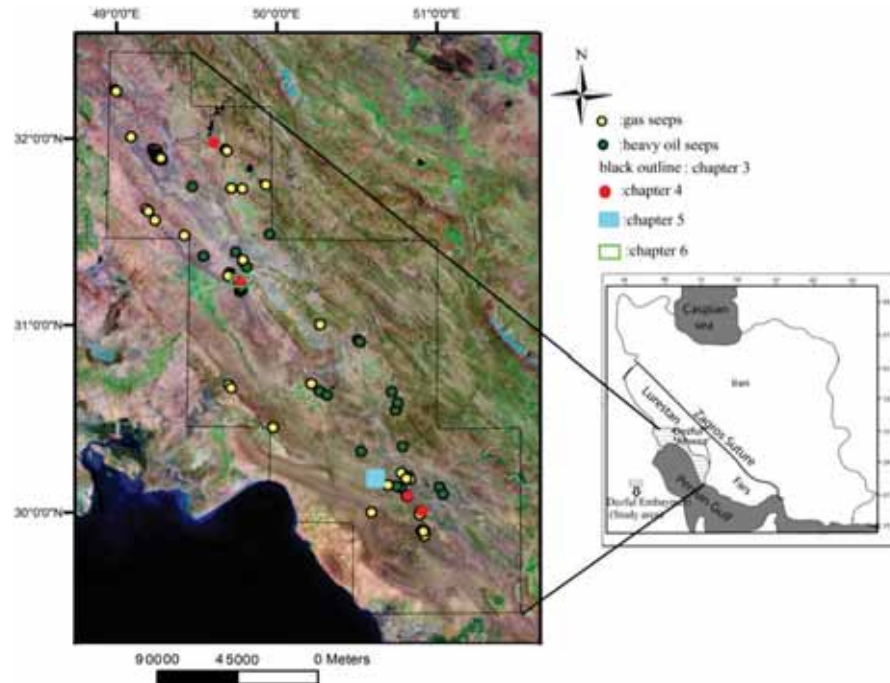


**Figure 1.4:** Distribution of hydrocarbon seeps in the Zagros belt and locations of study areas in the various chapters. Landsat image is in the background.

## **2. Remote sensing of onshore natural hydrocarbon seep-induced alteration<sup>1</sup>**

---

<sup>1</sup> This chapter is based on the following paper: Salati, S., van Ruitenbeek, F. J. A., van der Meer, F. D., 2014. Remote sensing of hydrocarbon seep-induced alteration in onshore basins: a review: Terra Nova (In preparation)

## **2.1. Introduction**

A hydrocarbon seep occurs where due to different pressure in the earth's subsurface, liquid or gaseous hydrocarbons escape to the surface through fractures in the rock and planes of weakness between geological layers. Natural hydrocarbon seeps have long been used in petroleum exploration methods. They are the ends of migration pathways which may provide indications of the presence of subsurface reservoirs and give the first clues to petroleum producing areas. Many of oil and gas fields around the world have been discovered as a result of drilling in seeping areas. The presence of seeps at the surface is not indicative of the size of a petroleum basin and they may even be located over a non-productive basin. However, it is an indirect evidence of the presence of mature source rocks within a geological system at depth.

On land, hydrocarbon seep-induced alteration has been widely studied by traditional techniques such as geochemical and geophysical analyses. Some of these studies have been published by peer-reviewed journals (e.g., <http://www.iso-analytical.co.uk/geochemistry.html>; Klusman and Saeed, 1996; Louis and etal, 2009; Osorio MT et al., 2011; Schumacher, 2011; Staenz et al., 2002) and others might be kept as classified reports with petroleum companies. These methods, however, are expensive, time consuming and only applicable to some observations collected in the field mainly around drilled areas in an active petroleum field. Thus, they cannot be used for mapping alterations and their variations related to different types of seeps and various host lithologies over a large area. Oil and gas prospecting requires the combination of different types of data and remote sensing offers the confidence-building benefit of iterative sampling. The interpretation of remotely sensed imagery cannot reveal depth, size, quality, and presence of hydrocarbon in reservoirs, but it is cost effective and could increase the probability success in exploration. Researchers have found remote sensing more successful in detecting indirect evidences of hydrocarbon seeps in rocks, soils, and vegetation than direct detecting of oil and gas. Oil displays distinctive spectral features at 1.7  $\mu\text{m}$ , 2.3  $\mu\text{m}$ , and 2.6  $\mu\text{m}$ , as well as some overtones from shorter wavelengths (Cloutis, 1989; Ellis et al., 2001; Horig et al., 2001; McCoy et al., 2001). Nevertheless, there is spectral confusion with other bituminous surfaces and brightness confusion with dark surfaces such as shade and moisture. Microseep gases such as  $\text{CH}_4$  (methane) and  $\text{CO}_2$  (carbon dioxide) have absorption features in VNIR-SWIR, but these gases are present in atmosphere ( $\text{CO}_2$ ) or have very narrow absorption features ( $\text{CH}_4$ ) (Jones III and Burtell, 1996) and are, therefore, difficult to be detected.

Using remote sensing in hydrocarbon seep study may have two approaches; a regional view for supporting stratigraphic and structural interpretations in related basins and direct detection of spectral features of hydrocarbon seep related alteration at the surface and confirm this fact that reservoirs are not

entirely sealed and hydrocarbons could escape, reach the surface, and cause alterations in soils, rocks, and vegetation. Iron bearing minerals, carbonates, hydrate and hydroxide minerals such as gypsum and clays are among the most common alteration related minerals induced by onshore hydrocarbon seeps in sediments (Schumacher, 1996). These minerals display distinctive signatures in VNIR-SWIR wavelength ranges related to their overtones and combination tones (Hunt, 1977) and can be recognized and mapped by remote sensing tools. On land, hydrocarbon microseep-induced alteration has been successfully mapped by remote sensing tools and evaluated by ground truth data in some petroleum reservoirs in the USA, Brazil, and China (Fu et al., 2007; Khan and Jacobson, 2008; Lammoglia and Filho, 2013; Lammoglia et al., 2008; Moore, 1999; Petrovic et al., 2008; Petrovic et al., 2012; Shi et al., 2012; van der Meer et al., 2002; Wang and Ding, 2000).

In regional surveys, where the objective is to prove the existence of an active source system, it may suffice to only locate and characterize hydrocarbon anomalies anywhere within the target geological system. However, combining spectral characteristics of seep-induced alteration with geological, geochemical, and geophysical data would allow us to get more reliable information and benefits from remote sensing data, which can be used to relate surface-detected alteration to subsurface migration.

A problem with the use of onshore microseep-induced alteration is that alteration related minerals are spectrally not unique to seeps and separating those alterations from the background is sometimes problematic. In addition, the scale of alterations is often small and formation of alteration minerals in seeping area may take more than two decades. Onshore, most studies of indirect detection of hydrocarbon seeps have mostly been focused on vegetation stress (e.g., Abrams, 1996; Bammel and Birnie, 1994; Etiope and Klusman, 2010; Horvitz, 1972; Lakkaraju et al., 2010; Maček et al., 2005; Noomen et al., 2006; Noomen et al., 2012; Smith et al., 2004; van der Werff et al., 2008; Yang et al., 1999, 2000) and less attention has been paid to mineral changes in sediments. The present chapter reviews the spectral characteristics of mineralogical alteration induced by hydrocarbon seeps in sediments. Successes, limitations and present state of the art in seep-induced alteration research are described and will guide the research directions in following chapters.

## **2.2. Classification of hydrocarbon seeps at the surface**

Based on processes affecting hydrocarbon seeps, Clarke and Cleverly (1991) classified seeps to; (a) unaltered seeps, (b) seeps affected by surface dispersal processes, and (c) seeps altered by subsurface processes (interaction of petroleum and water with migrations pathways rocks). Abrams (1996) classified seeps at the surface into; active seeps and passive seeps. Active seeps are places where hydrocarbons are actively seeping in large concentrations within and

above marine sediments. Active seeps contain low molecular weight ( $C_1$  to  $C_5$ ) and high molecular weight hydrocarbons that are visible. Active seeps typically occur in petroleum basins that are now actively generating hydrocarbon and generally referred to as macroseeps (visible seeps). Such areas are indicative of excellent migration pathways. Passive seeps zones are not actively seeping which can contain low molecular weight hydrocarbon concentrations above background (microseeps or invisible seeps), but also in some areas they can contain high molecular weight hydrocarbons (macroseeps). Passive seeps represent relict seeps of migrated hydrocarbons in basins with passive hydrocarbon generation and/or the presence of excellent seals or poor migration pathways (Abrams, 1996).

Hydrocarbon microseeps (invisible) migrate vertically or near vertically from subsurface reservoirs to the surface through the water-filled network of fractures, joints and bedding planes. They can be recognized by high amounts of light hydrocarbon in soils over a petroleum reservoir (Saunders et al., 1999). The presence of hydrocarbon macroseeps (visible) at the surface is direct evidence of hydrocarbon migration in a separate phase of oil or gas. As hydrocarbon moves to the surface, they re-equilibrate to oil and gas. They can be in contact but are often segregated due to differences of migration pathways such as spillage of oil, capillary leakage of oil and gas, trapping configuration, and cap rock behavior (Matthews, 1996). The study of hydrocarbon macroseeps brings important clues as to the nature of microseeps.

### **2.3. Migration pathways of hydrocarbon seeps**

In 1952, Link concluded five geological structures as hydrocarbon migration pathways: (1) seeps emerging from homoclinal beds; (2) seeps coming from mature source rock outcrops; (3) petroleum leaking from breached traps; (4) seeps along unconformities; and (5) seeps associate with intrusions such as mud volcanoes and salt domes. However, some aspects of petroleum geology such as definition of structures and understanding of fluid movements have changed since Link's (1952) explanations of hydrocarbon migration and associated structures. Three migration pathways have been proposed by MacGregor (1993) for hydrocarbon seeps including; (a) structurally controlled secondary migration; (b) lateral spillage from hydrocarbon accumulations during basin tilting; and (c) vertical leakage from accumulations breached by faulting and diapirism. Matthews (1996) studied hydrocarbon seeps migration mechanisms and pointed out that free phase interacting with a heterogeneous rock framework is the dominant migration mechanism.

With keeping that in mind, it is notable that hydrocarbon seeps migration are controlled by many mechanisms and each may or may not have significant local effects. General classifications cannot encapsulate the complex and highly variable spatial relationships of hydrocarbon seeps with tectonics, lithology, and

subsurface accumulations in different provinces. All those classified structures are some of the *possible* migration pathways for hydrocarbon seeps to reach the surface. To determine the most *probable* migration pathways of hydrocarbon seeps in any petroleum basin, a detailed study of spatial pattern and spatial association of hydrocarbon seeps with geological features is instructive. Such studies could provide insights into the geological processes that control hydrocarbon seep occurrence. Offshore, there are extensive studies about spatial patterns of hydrocarbon seeps (De Boever et al., 2009; Huang et al., 2009; Jin et al., 2011; Washburn et al., 2005) and various conceptual models of hydrocarbon migration in such areas have been proposed (Ding et al., 2008; Leifer and Boles, 2005, 2006). In contrast, spatial distributions of hydrocarbon seeps are poorly studied in different onshore provinces.

#### **2.4. Alterations induced by hydrocarbon seeps**

At the surface, escaped hydrocarbons oxidize and form reducing environment that favor the formation of mineralogical and botanical anomalies. In addition, slightly acidic conditions are created due to the production of CO<sub>2</sub>, H<sub>2</sub>S, and organic acids (resulted from microbial oxidation of hydrocarbons). Chemical changes in the environment of surface rocks cause mineralogical alterations such as red bed bleaching, clay formation and uranium enrichment, formation of secondary carbonates, sulfides, and magnetic minerals. Detailed studies of alterations induced by hydrocarbons either by microseeps or by macroseeps have documented by Shumacher (1996), Saunders et al (1999) , and van der Meer et al (2002).

At the surface, most hydrocarbon seep-induced alterations appear as bleached areas (in grey or white color) (Figure 2.1). Hydrocarbons and H<sub>2</sub>S are the dominant reducing agents responsible for bleaching effects. Acidic or reducing fluids dissolve ferric oxides (hematite) that give the red bed such characteristic appearance. H<sub>2</sub>S is created by sulfate reducing species and could be related to three types of geological-geochemical processes; (a) thermal disintegration of sulfur-bearing organic matter in kerogen, (b) bacterial reduction of sulfate minerals (BSR) in gypsum bearing carbonates at temperature <60-80°, and (c) high temperature thermochemical reduction between sulfate minerals in gypsum-bearing carbonate rocks and hydrocarbons (TSR) at temperature 100-140°. Dissolved sulfates and reactive organic are the most important reactants involved in BSR and TSR (Machel, 2001).

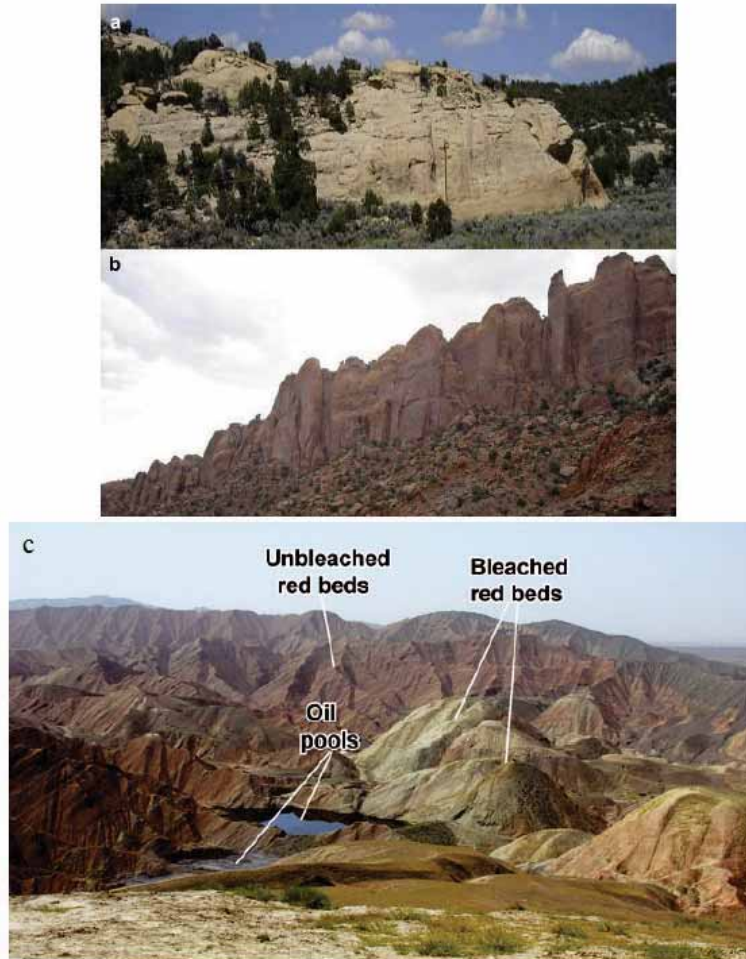


**Figure 2.1:** (a) Alteration induced by hydrocarbon microseeps in Wintage sandstones (Petrovic et al., 2012). (b) Unaltered Wintage sandstone, Lisbon Valley, Utha, USA (Petrovic et al., 2012). (c) Bleached and unbleached red beds of Dushanzi anticline and the presence of oil macroseeps in the Tian Shan Mountains, China (Fu et al., 2007).

In groundwater, carbon dioxide forms carbonic acid ( $H_2CO_3$ ), which can react with clay minerals and cause secondary calcium carbonate deposition and silicification. In acidic conditions resulting from hydrocarbons microbial oxidation, diagenetic weathering of feldspar to clays, leaching of potassium and other radioactive elements from clays, and conversion of smectite clays to kaolinite are common alteration related products (Figure 2.2). In addition, ferrous carbonates known as “Delta C” shows highs above the edges of petroleum accumulations.

The reactions between hydrogen sulfide and iron oxides can produce magnetic anomalies including magnetite, maghemite, pyrrhotite, and greigite over oil and gas fields. However, the exploration significance of such anomalies remain controversial because increases in soil magnetic susceptibility can be related to rainfall and climate and not hydrocarbon seeps (Liu et al., 1994; Maher and Thompson, 1992). Uranium minerals can be precipitated as products of microbial activities. The reducing environment created by hydrocarbons favors the formation of uranium and other heavy metals. Electrochemical and geobotanical anomalies are among the other alterations induced by hydrocarbon seeps, which the later one has been investigated more.

Nevertheless, specific responses to hydrocarbon seeps vary in different petroleum systems and geology, tectonics, soil types, and climate are important factors, which can affect those responses.

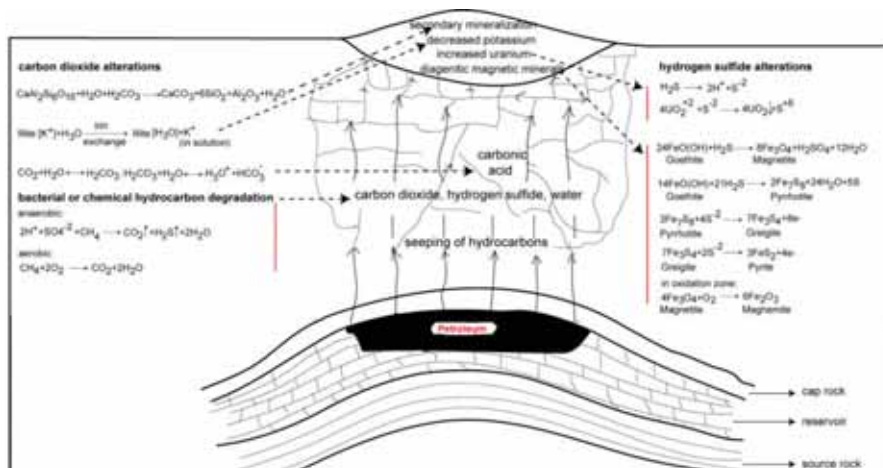


**Figure 2.2:** Generalized model of hydrocarbon geochemical alteration of sediments adopted from (Saunders et al., 1999).

## 2.5. Remote sensing studies of onshore hydrocarbon seep-induced alteration

Many of minerals involved in the reactions between hydrocarbon seeps and surrounding rocks at the surface can be identified and evaluated in a spatial context with reflectance spectroscopy and imaging spectroscopy. In the VNIR (0.40-2.00  $\mu\text{m}$ ) and SWIR (2.00-2.50  $\mu\text{m}$ ) bands, iron bearing minerals, carbonates, hydrate and hydroxide minerals such as gypsum and clays display molecular absorption features related to their overtones and combination tones (Hunt, 1977). Those minerals are some of the most common alteration related minerals induced by hydrocarbon seeps (Schumacher, 1996).

Spectroscopic visible-near infrared and shortwave infrared (VNIR-SWIR) analyses on hydrocarbon seep-induced alteration contain spectral information on diagnostic minerals. Most of researches related to reflectance spectroscopy applications in geosciences involve spectra-lithologic mapping, and exploration for economic minerals within volcanic and metamorphic rocks (Cudahy et al., 2009; Hunt, 1975; Mars and Rowan, 2010; Rowan and Mars, 2003; Rowan et al., 2005; Sabine, 1999; Salati et al., 2011; Serkan Öztan and Lütfi Süzen, 2011; van der Meer et al., 2012; Vicente and de Souza Filho, 2011), alteration related to hydrothermal systems (e.g., Hubbard et al., 2003; Tangestani and Moore, 2001; van der Werff et al., 2007; van Ruitenbeek et al., 2006; van Ruitenbeek et al., 2008), and detecting vegetation stress caused by hydrocarbon effects (Bammel and Birnie, 1994; Etiope and Klusman, 2010; Horvitz, 1972; Lakkaraju et al., 2010; Maček et al., 2005; Noomen et al., 2006; van der Meer et al., 2002; van der Werff et al., 2008; Yang et al., 1999, 2000).

Despite the importance of reflectance and imaging spectroscopy for detecting seep-induced alteration in a sedimentary basin, those alterations are not well documented. Most publications about remote sensing study of hydrocarbon seeps have commonly been focused on few reservoirs in USA, Brazil, and China (Table 1) (Bowen et al., 2007; Filho et al., 1999; Filho, 2002; Fu et al., 2007; Khan and Jacobson, 2008; Lammoglia and Filho, 2013; Lammoglia et al., 2008; Moore, 1999; Petrovic et al., 2008; Petrovic et al., 2012; Shi et al., 2012; van der Meer et al., 2002; Wang and Ding, 2000; Zhang et al., 2011).

The satellite and airborne data such as Landsat/ETM, ASTER, Hyperion, and HyMap have been commonly applied to enhance those alterations. Band rationing, principal component analysis (PCA), and Minimum Noise Fraction (MNF) have been applied to spectrally enhance seep-induced alteration while spectral mapping methods such as Spectral Feature Fitting (SFF), Spectral Angle Mapper (SAM), Mixing Tuned Matched Filtering (MTMF) have showed successes in mapping hydrocarbon seep-induced alteration in onshore provinces. In some areas, however, spectrally separating alterations from the background is difficult by applying common mapping techniques. van der Werff et al (2006) developed a knowledge-based two stages Hough Transform (HTTS) algorithm to detect alterations induced by natural gas seeps in northeast Hungary. The HTTS is an object based technique, which can find spectral signals that occur in seeps-specific spatial pattern: circles (alteration halos) following a line (fault).

Neural Networks, Fuzzy Clustering (Abrams, 1996; Lammoglia et al., 2008), and Bayesian probability statistics (van der Meer et al., 2002) were used to integrate geochemical data with remote sensing data and to model the probability of the occurrence of seep-induced alteration. Alteration related minerals identified by reflectance and imaging spectroscopy were validated by

isotopic data, XRD, thin section, and bulk rock chemistry analyses (Bowen et al., 2007; Khan and Jacobson, 2008; Moore, 1999; Petrovic et al., 2008; Shi et al., 2012). Table 1 displays remote sensing data and image processing techniques, which have been so far applied to map hydrocarbon seep-induced alterations.

**Table 2.1** Displays remote sensing data and image processing techniques applied to map hydrocarbon seep-induced alterations in sediments.na=not available.

Petroleum basin	Alteration related minerals	Remote sensing data	Band ratio	PCA	Mapping techniques	Reference spectra	Reference
1 Ventura basin, California, USA	calcite enrichment alteration profile to limestone	hyperspectral Pav-1	na	na	SAM, Cross Correlation Spectral Matching (CCSM)	laboratory spectra, image derived spectra	van der Meer et al (2002)
2 Mitra, Hungary	loess soil contains decayed organic matter and iron oxides	conversion of laboratory data to image, aerial photo	na	na	Hough transform object based technique	laboratory spectra	van der Weff et al (2006)
3 Jiangxi basin, China	bleaching red beds low values of ferrous iron clay mineral alteration	Landsat 7 ETM+	31/31 (3+31)-(32+3) 37/34	PCA on bands 1344, 1357, 2157/1457	na	na	Zhang et al (2007, 2011)
4 Dushan satellite, Tian Shan, China	bleaching of red bed carbonate mineral formation	ASTER	32/31, 34/30	na	na	na	Fu et al (2007)
5 Navajo sandstone, Utah, USA	bleaching red beds alteration of K-feldspar to kaolinite	HyMap	na	na	Matched Filter (MF), MNF, SAM	laboratory spectra, image derived spectra	Brown et al (2007)
6 Peach Draw Wyoming, USA	alteration of feldspar to clays	Hyperion	na	na	MNF, SAM	laboratory spectra image derived spectra USGS spectral library	Khan and Jacobson (2008)
7 Lilbourn valley, Utah, USA	bleaching red beds, increase in clay amount carbonate concentration of sandstone, silicate mineralization, presence of sulfides	ASTER, SAR	na	PCA on VNIR-SWIR	Maximum Likelihood, fusion	image derived spectra	Petrovic et al (2008)
8 Kaps Farmland basin, Tian Shan, China	red bed bleaching, formation of secondary carbonates	ASTER	32/31, 34/30	na	na	na	Shi et al (2012)
9 Lilbourn valley, Utah, USA	anomalous kaolinite and carbonate concentrations, anomalous kaolinite and other clay mineralizations	HyMap	na	na	SAM, SFF	image derived spectra, spectral library	Petrovic et al (2012)
10 Tucano, Brazil	abundance of clay minerals, depletion of limestone, bleaching of red beds radioactivity intensity, diagenetic carbonate and carbonatic cement	Landsat 5 ETM+ ASTER	TM2/TM1, TM4/TM3	na	MNF, SAM, MTF, Neural Networks, Fuzzy Clustering	laboratory spectra,	Filho et al (1999), (2002), Lammoglia et al (2008, 2013)

## 2.6. Discussion and conclusions

The value of hydrocarbon seeps either as visible (macroseeps) or invisible (microseeps) is always there, but using them as one of input information in petroleum exploration survey is only possible with geological interpretations. In a regional survey, where the objective is simply to prove the existence of an active source system, it may suffice to locate and characterize just hydrocarbon anomalies anywhere within the target geological system. Nevertheless, geochemical and/or spectral surveys should not be thought as black magic tools of spotting locations of seep-induced alterations but rather as methods of collecting reliable data which can be used wisely and be interpreted well enough along other geological data for petroleum explorations campaigns. Remote

sensing study of onshore hydrocarbon seeps has geologically been restricted to few petroleum systems contain hydrocarbon microseeps mostly occurred in sandstones (Figure 2.3).

Study of hydrocarbon seeps within other petroleum basins with different lithologies deserves more attentions. Results of such studies would provide valuable information about the efficiency of different types of cap rocks; thus, they can have implications for petroleum reservoirs in global scales.

The key to understanding the surface anomalies lies in understanding how hydrocarbon leaks to the surface and what is the most probable subsurface migration pathways. Onshore, spatial distribution of hydrocarbon seeps and their spatial association with geological features have been poorly studied. A detailed study of spatial pattern and spatial association of hydrocarbon seeps in a petroleum basin is instructive to determine the most *probable* migration pathways of hydrocarbon seeps from the *possible* one. It is doubtful that subsurface migrations will ever be fully understood because it is a very complex phenomena controlled by many factors and all interpretations are only based on basic principles of science and our observations. However, study of spatial distribution of hydrocarbon seeps provides insights into what geological processes control the occurrence of hydrocarbon seeps at the surface.

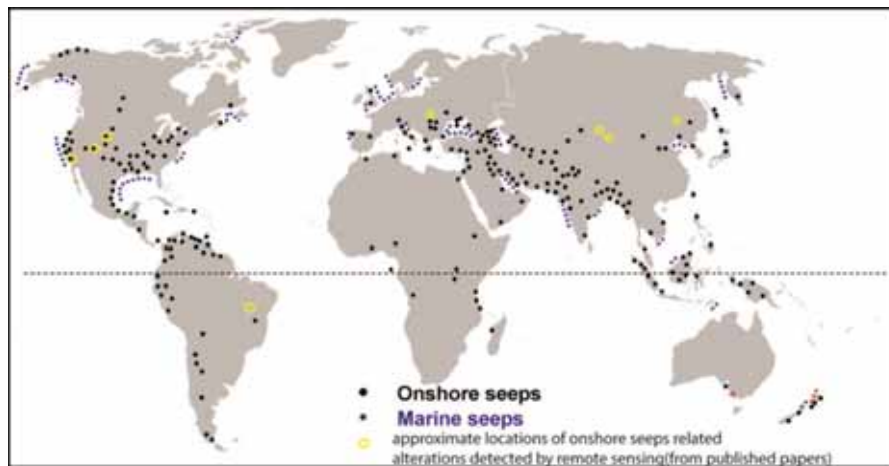


**Figure 2.3:** Global distribution of petroleum seeps (Etiopie, 2009) and approximate locations of onshore seep related alterations studied by remote sensing (Fillho, 2002; Fu et al., 2007; Lammoglia and Filho, 2013; Lammoglia et al., 2008; Moore, 1999; Petrovic et al., 2008; Petrovic et al., 2012; Shi et al., 2012; van der Meer et al., 2002; van der Werff et al., 2007; Zhang et al., 2011).

In most remote sensing studies which have so far been carried out on seeps related alteration, reflectance spectroscopy of altered rock samples taken from field observations did not show significant differences with non-altered areas.

However, the spectral characteristics of those alterations such as the position of absorption features, depth of absorption features, and the asymmetry of spectra show differences between altered and non-altered sediments. Such spectral characteristics of alterations have not been well studied. Spectral characteristics may provide instructive information about the amount and types of minerals, which can be validated with geochemical data. Therefore, spectroscopy studies should not only be focused on finding diagnostic features of minerals but rather interpreting spectral characteristics of diagnostic features.

Although geochemical data such as XRD, XRF, and thin sections can be used to validate minerals identified by spectroscopy, only isotopic data would provide reliable information to understand the origin of seeps and relate the surface alterations to underlying reservoirs. Except researches have been carried out by Khan and Jacobson (2008) and Pterovic et al (2012), no attempts was made to relate surface alterations detected by remote sensing studies to subsurface reservoirs using isotopic data.

The information about the spatial extension of alterations related to hydrocarbon seeps has been missed from literatures of remote sensing studies. Such information would allow us to select suitable remote sensing data to study alteration related minerals in areas affected by hydrocarbon seeps. Multispectral ASTER and hyperspectral data have been successfully used to map onshore seep-induced alteration. ASTER data may be more of interest for geoscientists because these data are able to compensate for limitations of site specific applications of airborne hyperspectral data and the limited mineral mapping capacity of Landsat TM data.

Although hydrocarbon seep-induced alteration can be mapped with ASTER data, in some areas, the scale of alteration zones is smaller than the spatial resolution of ASTER. High spatial resolution satellite data such as IKONOS, QuickBird, and the relatively new WorldView-2 (WV-2) may provide the opportunities to map mineral variations occur at small scales. The new WV2 data have 8 spectral bands in the VNIR with 2 m resolution and one panchromatic band with 0.5 m resolution. This new dataset has not yet been applied for mineral mapping. With 8 bands in VNIR wavelength ranges, the WV-2 can provide us important information about transition elements, especially about iron and elemental sulfur. The use of WV-2 imagery poses a new challenge in minerals mapping because some minerals such as carbonates and some clays do not exhibit diagnostic spectral responses in VNIR wavelength ranges but the bleaching effect of hydrocarbon seeps can be mapped with this data. Although spectral resolution is the main support in image classification, spatial resolution is the main factor in recognition accuracy of the ground objects. Ground control points are needed to validate spatial distribution of minerals identified with image classification techniques. In areas with few

ground data, it is difficult to validate spatial distribution of minerals identified from image with field measurements because these measurements may cover few pixels of the imagery. One promising approach in image classification is integrating high spectral resolution data with high spatial resolution data to solve this challenging task. Integration of ASTER and WV-2 data for mineral classification would allow us to understand if spatial resolution of WV-2 and its multispectral bands in VNIR have any impacts on classification of target minerals.

Chapters 3 to 7 present and discuss the spatial pattern of seeps and reflectance and multispectral image analyses of seep-induced alterations in one of the richest petroleum basin around the world, Zagros.

### **3. Conceptual modelling of onshore hydrocarbon seep occurrence in the Dezful Embayment, SW Iran<sup>2</sup>**

---

<sup>2</sup> This chapter is based on the following paper: Salati, S., van Ruitenbeek, F. J. A., Carranza, E. J. M., van der Meer, F. D., and Tangestani, M. H., 2013, Conceptual modeling of onshore hydrocarbon seep occurrence in the Dezful Embayment, SW Iran: *Marine and Petroleum Geology*, v. 43, p. 102-120.

## **Abstract**

Petroleum and gas seeps on the ground surface are direct indicators of accumulations of hydrocarbons in the subsurface and could reflect the migration of hydrocarbons in a sedimentary basin. Quantitative analyses of the spatial pattern of hydrocarbon seeps and their spatial associations with geological features could aid in deducing geological controls on their occurrence. In this study, the Fry analysis was applied to study the spatial pattern of mapped hydrocarbon seeps, whereas spatial association analyses were implemented to quantify the spatial association of mapped seeps and their alteration products with geological features. The spatial pattern analysis of hydrocarbon seeps showed that oil seeps followed prominent NW-SE and NE-SW trends while gas seeps followed NW-SE and N-S trends suggesting that NNE-SSW and NW-SE fractures are possible migration pathways for hydrocarbons to reach the surface. The results of the spatial association analysis illustrated strong positive spatial associations of oil and gas seeps with the Gachsaran and the Mishan formations, implying upward migration of hydrocarbons through permeable micro-fractures and micro-pores in their strata. A conceptual model has proposed for the occurrence of onshore hydrocarbon seeps in the Dezful Embayment.

### **3.1. Introduction**

Petroleum and gas seeps on the ground surface are direct indicators of accumulations of hydrocarbons in the subsurface and could reflect the migration of hydrocarbons in a sedimentary basin. Due to high pressures at depths, hydrocarbons in the subsurface can escape to the surface through fractures in rocks and planes of weakness between geological layers.

There are extensive studies about spatial patterns of hydrocarbon seeps in offshore areas (De Boever et al., 2009; Huang et al., 2009; Jin et al., 2011; Washburn et al., 2005) and various conceptual models of hydrocarbon migration in such areas have been proposed (Ding et al., 2008; Leifer and Boles, 2005, 2006). In contrast, few studies have been published about the geological context of hydrocarbon seeps in onshore areas (Clarke and Cleverly, 1991; Link, 1952; MacGregor, 1993). Hydrocarbon seeps are spatially associated with structures such as faults, fractures, folds, unconformities, and salt domes. They can be found within the reservoirs and cap rock formations exposed at the surface. Spatial associations of hydrocarbon seeps with geological features could aid in investigation of cap rock capacity at regional scales (O'Brien et al., 2005; Pinet et al., 2008). In addition, recognition of spatial associations between hydrocarbon seeps with geological features could provide additional valuable information for exploration and environmental programs (Ellis et al., 2001; Etiope et al., 2006).

Methods for quantitative analyses of the spatial pattern of mineral deposits and their spatial associations with geological features have been extensively applied for mineral prospectivity mapping (Carranza, 2009a, b; Carranza and Sadeghi, 2010). Such methods have not yet been applied, however, to study hydrocarbon seep occurrences. Like in mineral prospectivity analysis, quantitative analyses of the spatial pattern of hydrocarbon seeps and their spatial associations with geological features such as faults, fractures, and lithologies could aid in deducing geological controls on their occurrence. Analysis of the spatial pattern of mapped hydrocarbon seeps could provide insights into which geological features control their localization at the surface. In addition, analysis of spatial association of mapped seeps with geological features is instructive in weighing the importance of each geological feature as controls on the occurrence of hydrocarbon seeps. Consequently, such analyses would allow development of a conceptual model of how hydrocarbon seeps are localized at the surface and why they occur only at specific sites.

In this chapter, we describe quantitatively the spatial pattern of mapped hydrocarbon seeps in the Dezful Embayment, SW Iran. The prime objectives of this study are to obtain insights about (a) links between geological structures such as faults, fold axes and fractures and hydrocarbon seeps and (b) the

probability of spatial association of different geological features such as lithological units and their associated structures with oil and gas seeps. We chose the Dezful Embayment for this study because sufficient knowledge exists about the distribution of petroleum at the surface and in the subsurface.

### **3.2. Hydrocarbon seeps in the Zagros belt**

The presence of hydrocarbon seeps led to the discovery of the subsurface petroleum in the SW Iran in early 1900s. There are different types of hydrocarbon seeps in the Zagros fold-thrust belt, such as crude oil, heavy oil or asphalt, gas, gas/oil. Gach-e-tursh and sulphur springs are products of the subsurface alteration processes of gas seeps (Clarke and Cleverly, 1991), which are common in the Dezful Embayment. The term Gach-e-tursh, which was used by Thomas (1952), represents an association of oxidizing petroleum seep, gypsum, jarosite, sulphuric acid, and sulphur.

There are few published studies about hydrocarbon seeps in the Zagros oil fields in Iran (Link, 1952; Safari et al., 2011). Based on geological controls, Link (1952) classified seeps into 5 groups. The Zagros hydrocarbon seeps were classified as seeps coming from oil accumulations, which have been eroded or reservoirs ruptured by faulting and folding. By using Remote Sensing techniques, Safari et al (2011) studied the role of the Kzerun fault on localizing oil and sulfur springs in the Nargesi oil field, SW Iran.

### **3.3. Methods**

We used 14 1:100,000 scale geological maps of the Dezful Embayment, which have been compiled by the Iranian oil company, to provide lithologic, structural, and hydrocarbon seep maps. Existing knowledge about petroleum systems in the Zagros oil fields (Bordenave, 2002; Bordenave and Hegre, 2010), and extensive studies about the structural framework of the Zagros fold-thrust belt (Berberian, 1995; Bordenave and Hegre, 2005; Carruba et al., 2006; Hessami et al., 2001; McQuillan, 1991; Sepehr and Cosgrove, 2002; Sherkati and Letouzey, 2004) provide us insights into defining geological controls on petroleum systems in the Zagros. Insights into geological controls on hydrocarbon seeps migration and localization can be derived by examining the spatial distribution of hydrocarbon seeps via spatial pattern and spatial association analyses. Because several locations of heavy oil/asphalt seeps and two products of gas seep alteration, namely Gach-e-tursh and sulphur springs, exist in geological maps of the study area, these sub-sets of seeps were used in the spatial analyses.

### **3.3.1. Analysis of spatial pattern of hydrocarbon seeps**

Hydrocarbon seeps exhibit trends that are similar to trends of faults and anticline axes (Figure 3.1) and lithologic units (Figure 3.2) in the study area. This illustrates that hydrocarbon seeps in the Zagros oil fields are, in general, structurally controlled (Beydoun et al., 1992; Bordenave and Hegre, 2010; Douglas Elmore and Farrand, 1981; Link, 1952; Rudkiewicz et al., 2007). However, there is a question about which specific sets of geological structures controls the occurrence of each sub-set of hydrocarbon seeps at regional and local scales. An answer to this question can be explored through analysis of the spatial pattern of each sub-set of hydrocarbon seeps. For this purpose, we applied Fry analysis (Fry, 1979) to maps of locations of hydrocarbon seeps in the study area.

Fry analysis is a geometrical method of examining spatial autocorrelation of a set of points, by plotting translations of points whereby each point is used as an origin for translation. Fry analysis describes the spatial pattern of a set of points based on orientations and distances between pairs of translated points. A rose diagram can be created for orientations and frequencies of orientations between all pairs of translated points and pairs of translated points within specific distances. These orientations reveal trends in the points of interest at regional and local scales (Carranza, 2009; Carranza and Sadeghi, 2010). Analysis of point's trends at local scales can be used to deduce processes that localize hydrocarbon occurrences (as points) at certain areas. To analyze trends between any two neighboring seeps, a minimum distance was used within which there is a maximum probability for only one neighbor point next to any one of the points.

We used the DotProc (<http://www.kuskov.com>) package for Fry analysis. We exported the map coordinates of hydrocarbon seep locations into a delimited file, which is supported by the DotProc software. Fry point coordinates were then exported back into the GIS to visualize and analyze the spatial pattern of seeps. We applied this method to all hydrocarbon seeps and to each sub-set of seeps, as well.

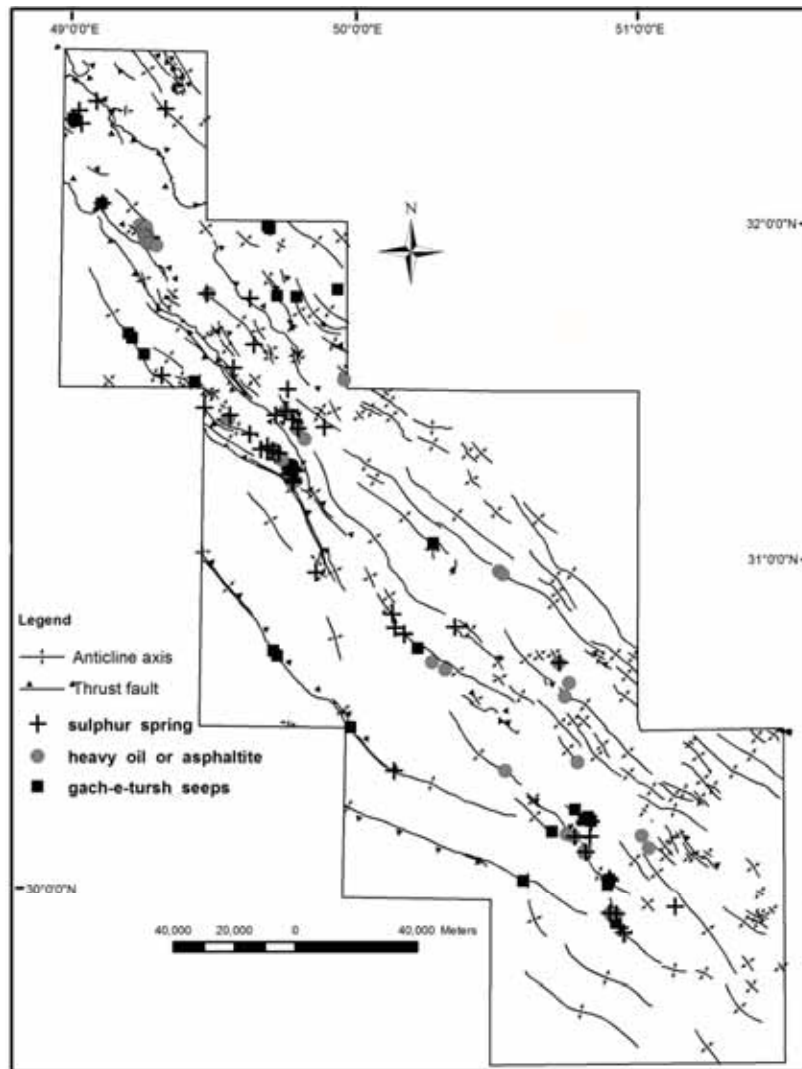


**Figure 3.1:** Distribution of faults, anticline axes, and hydrocarbon seeps in the study area.

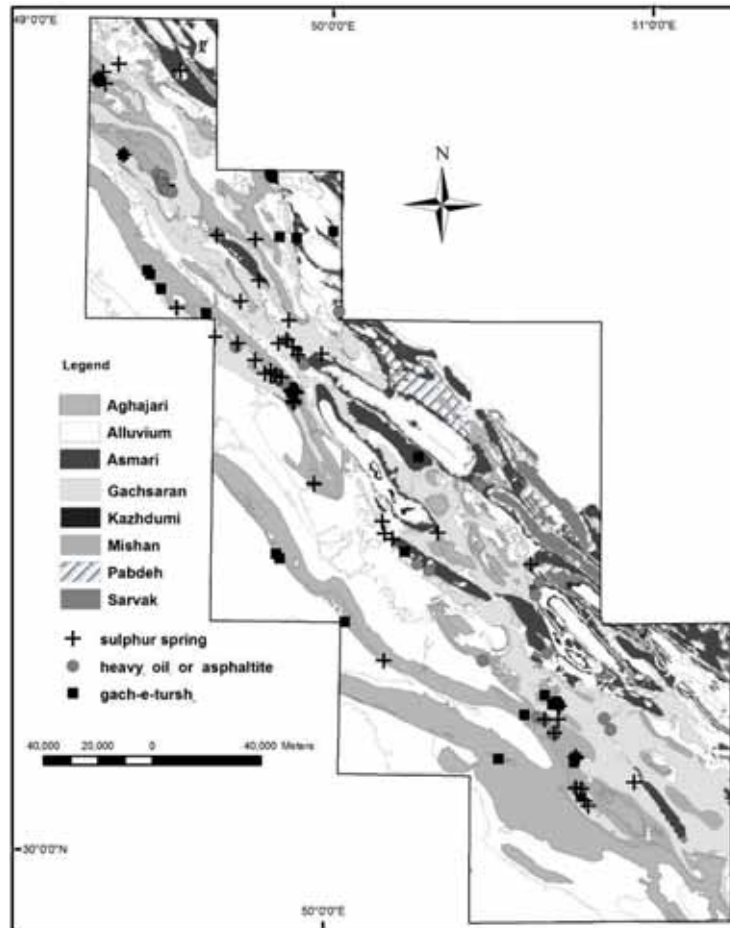


**Figure 3.2:** Distribution of hydrocarbon seeps, source rocks (Kazhdumi and Pabdeh Formations), reservoirs (Asmari and Sarvak Formations), cap rock (Gachsaran Formation), and the Mishan Formation.

### 3.3.2 Analysis of spatial association between hydrocarbon seeps and geological features

Analysis of the spatial association of occurrences of hydrocarbon seeps with geological features could provide insights into which features plausibly controlled those occurrences at specific locations. We applied the distance distribution analysis (Berman, 1977) for quantifying spatial association between hydrocarbon seeps and structural features such as mapped faults and anticline axes. The quantified spatial association refers to the distance or range of distances where hydrocarbon seeps are preferentially located from structural features such as faults and anticline axes. Also, we applied weights-of-evidence

(WofE) analysis (Bonham-Carter, 1994) to quantify spatial associations of hydrocarbon seeps with lithologic units.

### **3.3.1.1. Distance distribution analysis**

The distance distribution analysis quantifies spatial associations between a set of point objects and another set of objects with a particular geometry. It compares a cumulative relative frequency distribution of distances from a set of linear geo-objects to a set of points of interest (denotes as  $D(M)$ ) and a cumulative relative frequency distribution of distances from the same set of linear objects to a set of random point geo-objects (denotes as  $D(N)$ ).

In this study,  $D(M)$  and  $D(N)$  represent, respectively, a cumulative relative frequency distribution of distances from faults and anticline axes to hydrocarbon seeps and a cumulative relative distribution of distances from the same lineaments to a set of random points.

The graph of  $D(M)$  is compared with the graph of  $D(N)$  by computing Kolmogorov-Smirnov statistic to test the null hypothesis that locations of points of interest and linear geo-objects are spatially independent:

$$D = D(M) - D(N) \quad (1)$$

A positive  $D$  implies that there is a positive spatial association between the points of interest (hydrocarbon seeps) and the set of linear geo-objects, whereas a negative  $D$  implies negative spatial association between them. If  $D = 0$ , it implies that the locations of points of interest and the linear geo-objects are spatially independent. An upper confidence band for the graph of  $D(N)$  curve can be calculated to determine statistically and graphically if  $D(M)$  is greater than  $D(N)$  (Berman, 1977):

$$UD(N) = D(N) + \sqrt{9.21 \left( \frac{N + M}{4NM} \right)} \quad (2)$$

where  $M$  is the number of points of interest and  $N$  is the number of random point geo-objects. The value of 9.21 is a critical  $\chi^2$  value for 2 degrees of freedom and significance level  $\alpha=0.01$  (Berman, 1977).

The  $\beta$  statistic, which has a  $\chi^2$  distribution, can be applied to find the distance from a set of linear geo-objects at which a positive  $D$  value is the highest (Berman, 1977):

$$\beta = 4D^2NM / (N+M) \quad (3)$$

We applied this method to quantifying spatial association of hydrocarbon seeps with faults and anticline axes. The values of  $D$  (Eq. 1) show the spatial association of hydrocarbon seeps with structural features and values of  $\beta$  (Eq. 3) determine the distance of optimal positive spatial association between the same lineaments and seeps. A positive spatial association ( $D > 0$ ) between a set of hydrocarbon seep locations and a set of geological features suggests that the latter represents a set of probable geological controls on the occurrence of the former. The value of  $\beta$  represents an optimal distance from the geological features, which within this distance there is significantly higher proportion of the occurrence of hydrocarbon seeps than would be expected due to chance.

### 3.3.1.2. Weights of evidence (WofE) analysis

The WofE analysis uses a log-linear derivation of Bayesian probability to quantify spatial association between a dependent variable (e.g., hydrocarbon seep occurrence) and an independent variable (e.g., presence of geological features) by statistical means (see (Bonham-Carter, 1994) for more details). In WofE analysis, a positive weight ( $W^+$ ) and a negative weight ( $W^-$ ) represent, respectively, positive and negative spatial associations of points of interest  $D$  with spatial feature  $B$ . The  $W^+$  is calculated as:

$$W^+ = \log_e \frac{P\{B|D\}}{P\{B|\bar{D}\}} \quad (4)$$

and  $W^-$  is calculated as:

$$W^- = \log_e \frac{P\{\bar{B}|D\}}{P\{\bar{B}|\bar{D}\}} \quad (5)$$

where  $B$  is a binary map of a spatial feature and  $D$  is a binary map of points of interest. The  $P\{B|D\}/P\{B|\bar{D}\}$  is known as “sufficiency ratio” (LS) and  $P\{\bar{B}|D\}/P\{\bar{B}|\bar{D}\}$  is known as “necessity ratio” (LN). These ratios are also known as “likelihood ratios” (Bonham-Carter, 1994).  $D$  and  $B$ , respectively, indicate the presence of the points of interest and the spatial feature, whereas,  $\bar{D}$  and  $\bar{B}$ , respectively, represent the absence of the points of interest and the spatial feature.

The contrast ( $C$ ), which is a measure of the spatial association between the points of interest and the spatial features, is calculated as:

$$C = (W^+) - (W^-) \quad (6)$$

We applied the WofE method to provide a measure of spatial association of hydrocarbon seeps ( $D$ ) with lithologic units ( $B$ ). A studentized contrast ( $Sig C$ ) provides a measure of the certainty with which the contrast is known (Bonham-Carter, 1994). It is defined as the ratio of the contrast divided by its standard deviation. The studentized contrast ( $Sig C$ ) is calculated as (Bonham-Carter, 1994):

$$SigC = \frac{C}{\sqrt{s^2(W^+) + s^2(W^-)}} \quad (7)$$

A  $Sig C$  greater than 2 suggests a statistically significant spatial association. The maximum  $Sig C$  is used as index of significant spatial association between hydrocarbon seeps and lithological units.

### **3.4. Results**

#### **3.4.1. Spatial patterns of hydrocarbon seeps**

Mapped hydrocarbon seeps in the Dezful Embayment show prominent  $315^\circ \pm 15^\circ$  trend (Figure 3.3), which is roughly the same as the general trend of folds and faults in the Zagros fold-thrust belt. Fry plots of hydrocarbon seeps at local scales (<43 km) show subsidiary NNE-SSW trend (Figure 3.3c). At the local scale, the Fry plots of heavy oil or asphalt seeps show a prominent NW-SE trend and a subsidiary NNE-SSW trend (Figure 3.4). The Fry plots of Gachsaran and sulphur springs show prominent NW-SE and subsidiary N-S trends (Figures 3.5a, and 3.5b). These trends seem correspond with trends of major lineaments that are either perpendicular or parallel to (a) the general trend of the Zagros folds related to the shortening trend of the Zagros (NE-SW) and (b) the trends of basement faults (N-S and NW-SE). These indicate the ongoing influence of NW-SE and NNE-SSW trending faults and/or fractures on the occurrence of hydrocarbon seeps in the Dezful Embayment.

It is known that there is a close correlation between the oil production pattern and structures trending NNE-SSW (McQuillan, 1991) or N-S (Edgell, 1996). Thrust faults exposed to the surface are parallel to the NW-SE trending folds and are mostly located at the southwestern limb of anticlines. In addition, there are two types of fractures in the Dezful Embayment (Lacombe et al., 2011; Mobasher and Babaie, 2007; Stephenson et al., 2007; Wennberg et al., 2007): fold related fractures and fault related fractures. The  $45^\circ \pm 5^\circ$  (NE-SW) trend of all

hydrocarbon seeps is perpendicular to the axial trace of anticlines. This trend, which is possibly related to fold- and/or fault-related fractures, is strongly evident in the Fry plots of Gach-e-tursh at the local scale (Figure 3.5a). At the local scale, the Fry plots of the Gach-e-tursh and sulphur springs show a prominent  $160^{\circ}$ - $170^{\circ}$  (roughly N-S).

This trend is plausibly due to fractures formed at small oblique angles to the main N-S ( $10 \pm 5^{\circ}$ ) trending faults (e.g., Kazerun) (Mobasher and Babaie, 2007). The subsidiary E-W trend ( $80^{\circ}$ - $90^{\circ}$ ) of mapped hydrocarbon seeps is plausibly related to fractures oblique to NW-SE trending folds, NW-SE trending faults, and N-S trending basement faults.

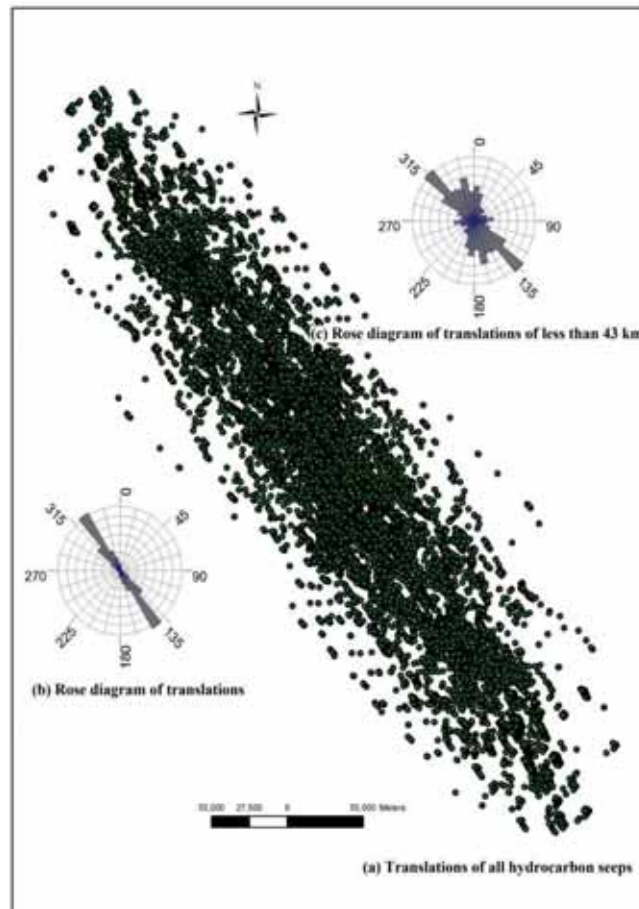


**Figure 3.3:** Fry plots and trends of pairs of Fry points of locations mapped hydrocarbon seeps.

By inference from the analyses of the spatial patterns of mapped hydrocarbon seeps in the study area, it is likely that NNW-SSE trending faults/fractures are plausible structural controls on the occurrences of oil and gas seeps. Heavy oil or asphalt seeps showed the prominent NW-SE trend, which is the same as the general trend of folds. Gas seep alteration products (Gach-e-tursh and sulphur springs) showed the prominent NNW-SSE trends, which are similar to the general trends of folds and basement faults. The results of the spatial pattern analyses can be interpreted further by analysis of spatial associations between mapped seeps and structural and lithological units.

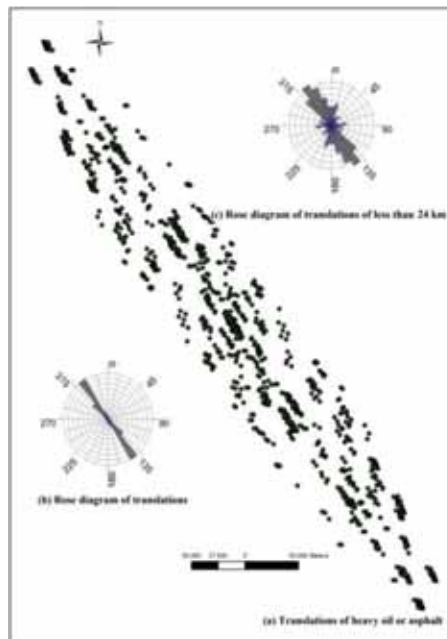


**Figure 3.4:** Fry plots and trends of pairs of Fry points of locations mapped heavy oil or asphalt seeps.

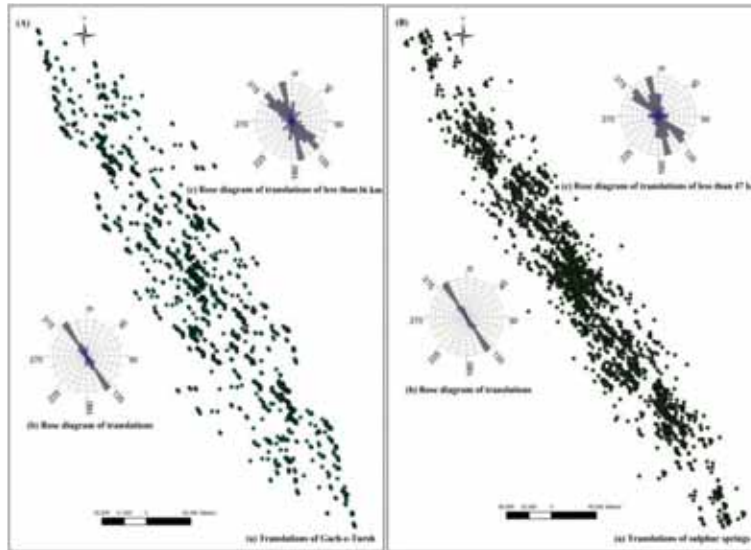


**Figure 3.5:** (A) Fry plots and trends of pairs of Fry points of locations mapped Gach-e-Tursh. (B) Fry plots and trends of pairs of Fry points of locations mapped sulphur springs.

### 3.4.2. Spatial associations of hydrocarbon seeps with structural units

Heavy oil or asphalt seeps have positive spatial association with anticlines (Figure 3.6a). Within 4 km of anticline axes, 78% of heavy oil or asphalt seeps are present. Based on the curve of  $D$ , there is at most 22% higher occurrence of heavy oil or asphalt seeps than would be expected due to chance (Figure 3.6a). As indicated in Figure 3.6b, there is positive spatial association between heavy oil or asphalt seeps and thrust faults. It appears in Figure 3.6b that about 60% of the heavy oil or asphalt seep occurrences are within 6 km of the mapped thrust faults suggesting that fault related fractures or/and non-fault related fractures can provide pathways for heavy oil seeps to reach the surface.

Sulphur springs have positive spatial association with anticline axes (Figure 3.6c) and thrust faults (Figure 3.6d). However, these spatial associations are not statistically significant (at  $\alpha=0.01$ ). The two peaks in the  $D$  curve (Figure 3.6c) imply that there are two groups of sulphur springs in the area. The first group is comprised of about 30% of the sulphur springs located about an average of 1 km away from anticline axes. The second group is comprised of about 70% of springs located about an average of 4 km away from anticline axes. It appears in Figure 3.6d that about 78% of the sulphur springs occurrences are within 10 km of the mapped thrust faults.

Gach-e-tursh shows weak but significant (at  $\alpha= 0.05$ ) positive spatial association with anticline axes. As indicated in Figure 3.6e, 38% of the Gach-e-tursh is located within 1 km of the mapped anticline axes. Within 1 km of anticline axes, there is at most 20% higher frequency of Gach-e-tursh than would be expected due to chance. The Gach-e-tursh shows statistically significant (at  $\alpha=0.01$ ) positive spatial association with thrust faults (Figure 3.6f).

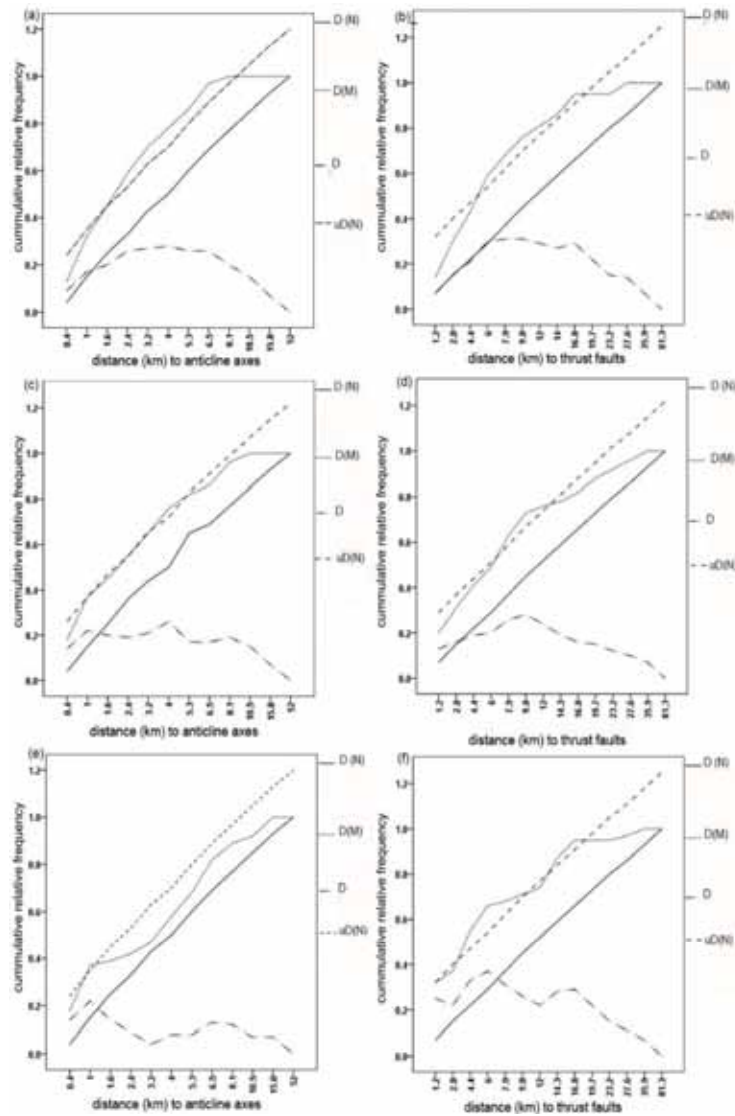


**Figure 3.6:** Graphs of cumulative relative frequency of distances at seep locations (D (M)) and non-seep locations (D (N)) around structural units in the Dezful Embayment. D and u D (N) represent spatial association of seeps with structures and confidence band for  $\alpha=0.01$  respectively. (a) and (b) show analysis of spatial association of heavy oil or asphalt seeps with anticline axis and with thrust faults; (c) and (d) represent analysis of spatial association of sulphur springs with anticline axis and with thrust faults; (e) and (f) show analysis of spatial association of Gach-e-Tursh with anticline axis and with thrust faults.

### 3.4.3. Spatial association of hydrocarbon seeps with lithological units

Table 3.1 presents the weights and contrast values calculated for each lithologic unit with respect to the heavy oil or asphalt seeps, Gach-e-tursh, and sulphur springs. The hydrocarbon seeps exhibit positive spatial associations with the Asmari (reservoir), Gachsaran (cap rock), and Mishan Formations.

The Gachsaran Formation shows significant positive spatial association with heavy oil or asphalt seeps. Heavy oil or asphalt seeps have positive spatial associations with the Asmari and Mishan Formations. Heavy oil or asphalt seeps lack spatial associations with the other lithological units with negative values of *SigC*.

Gach-e-tursh and sulphur springs show a significant positive spatial association with the Mishan Formation and positive spatial association with the Gachsaran Formation. The other lithological units do not show spatial associations with sulphur springs and Gach-e-tursh.

The quantified spatial associations of lithological units with mapped hydrocarbon seeps and their alteration products are coherent with facts that the densities of oil and gas seeps are not decreased upwards in the stratigraphy.

**Table 3.1** Variation of weights and contrasts for lithologic units with respect to (a) heavy oil or asphalt seeps; (b) Gach-e-tursh; and (c) sulphur springs.

Variation of weights and contrasts for lithological units with respect to heavy oil or asphalt seeps				
Lithologic units	$W^+$	$W^-$	$C$	$SigC$
Alluvium	0.006	0.14	-0.13	-0.27
Bakhtiari	0	0.076	-0.076	-0.15
Lahbari	0	0.09	-0.09	-0.18
Aghajari	-1.14	0.11	-1.15	-2.3
Mishan	0.8	-0.06	0.86	1.72
Gachsaran	1.3	-0.05	1.63	<b>3.26</b>
Asmari	1.09	-0.02	1.11	2.22
Gadvan	0	0.001	-0.001	-0.002
Gurpi	0	0.009	-0.009	-0.019
Hurmuz	0	0.0002	-0.0002	-0.0004
Kazhdumi	0	0.003	-0.003	-0.006
Pabdeh	0	0.2	-0.2	-0.4
Sarvak	0	0.02	-0.02	-0.04
Daryan	0	0.0002	-0.0002	-0.0004
Fahlyan	0	0.003	-0.003	-0.006
Shahbazan	0	0.0002	-0.0002	-0.0004

Tutak	0	0.0002	-0.0002	-0.0004
Variation of weights and contrasts for lithologic units with respect to <i>Gach-e-tursh</i>				
Lithologic units	$W^+$	$W^-$	$C$	$SigC$
Alluvium	-1.06	0.25	-1.31	-1.35
Bakhtiari	0	0.076	-0.076	-0.078
Lahbari	0	0.09	-0.09	-0.092
Aghajari	0	3.11	-3.11	-3.2
Mishan	2	-0.39	2.39	<b>2.4</b>
Gachsaran	1.08	-0.45	1.53	1.57
Asmari	-0.28	-0.3	0.3	-0.3
Gadvan	0	0.001	-0.001	-0.001
Gurpi	0	0.009	-0.009	-0.01
Hurmuz	0	-0.0002	-0.0002	-0.0002
Kazhdumi	0	0.003	-0.003	-0.003
Pabdeh	0.59	-0.025	0.615	0.6
Sarvak	0	0.02	-0.02	-0.02
Daryan	0	0.0018	-0.0018	-0.005
Fahlyan	0	0.005	-0.005	-0.005
Shahbazan	0	0.0002	-0.0002	-0.0002
Tutak	0	0.0002	-0.0002	-0.0002
Variation of weights and contrasts for lithologic units with respect to sulphur springs				
Lithologic units	$W^+$	$W^-$	$C$	$SigC$
Alluvium	-0.2	0.07	-2.07	-3.45
Bakhtiari	0	0.076	-0.076	-0.13
Lahbari	0	0.09	-0.09	-0.15
Aghajari	0	0.16	-0.16	-0.3
Mishan	1.53	-0.2	1.75	<b>2.9</b>
Gachsaran	1.13	-0.5	1.63	2.7
Asmari	-1.2	0.05	-1.25	-2.08
Gadvan	0	0.001	-0.001	-0.001
Gurpi	0	0.009	-0.009	-0.01
Hurmuz	0	0.0002	-0.0002	-0.0003
Kazhdumi	0	0.003	-0.003	-0.005
Pabdeh	-0.33	0.008	-0.34	0.6
Sarvak	0.02	0.02	-0.02	-0.03
Daryan	0	0.0018	-0.0018	-0.003
Fahlyan	0	0.003	-0.003	-0.005
Shahbazan	0	0.0002	-0.0002	-0.0003
Tutak	0	0.0002	-0.0002	-0.0003

#### **3.4.4 Spatial association of sub-sets of hydrocarbon seeps with structures only in lithological units having positive spatial association**

The results of the spatial association analysis show that heavy oil or asphalt seeps have significant positive spatial associations with anticline axes in the Asmari reservoir, Gachsaran, and Mishan Formations (Figures 3.7a, c, and e). These positive spatial associations are optimal within 2.6 km of the anticline axes in the Asmari Formation (Figure 3.7b), within 5.8 km of anticline axes in the Gachsaran Formation (Figure 3.7d), and within 3.8 km of anticline axes in the Mishan Formation (Figure 3.7f). Within 2.6 km, there is 100% occurrence of known heavy oil or asphalt seeps of the anticline axes in the Asmari Formation (Figure 3.7a). Within 5.8 km of anticline axes of the Gachsaran Formation, there is at least 50% higher frequency of heavy oil or asphalt seeps than would be expected due to chance (Figure 3.7c). According to the curve *D* in Figure 3.7e, within 3.8 km of the anticline axes in the Mishan Formation, there is at least 85% higher frequency of heavy oil or asphalt seeps than would be expected due to chance. From the curve *D*, it appears that heavy oil or asphalt seeps have stronger positive spatial association with anticline axes in the Asmari Formation.

These results are coherent with the fact that oil seeps occurring close to the Oligocene Asmari Formation represent the final exhaustion of former oil accumulations (Douglas Elmore and Farrand, 1981).

Figure 3.8 shows the analyses of spatial associations of heavy oil or asphalt seeps with thrust faults in the three lithologic formations having positive spatial associations with these seeps. There is no positive spatial association between heavy oil or asphalt seeps within 15 km of thrust faults in the Asmari Formation (Figure 3.8a), but this sub-set of seeps have positive spatial associations with thrust faults in the Gachsaran and Mishan Formations (Figures 3.8c and e). The two peaks in the *D* and  $\beta$  curves (Figures 3.8c and 3.8d) imply that there are two groups of heavy oil or asphalt seeps with respect to thrust faults in the Gachsaran Formation. The first group is comprised of about 70% of the heavy oil or asphalt seeps located about an average of 3.8 km away from thrust faults. The second group is comprised of about 30% of heavy oil or asphalt seeps located about an average of 10.4 km away from thrust faults. The positive spatial association of heavy oil or asphalt seeps is optimal within 5.4 km of thrust faults in the Mishan Formation (Figure 3.8f).

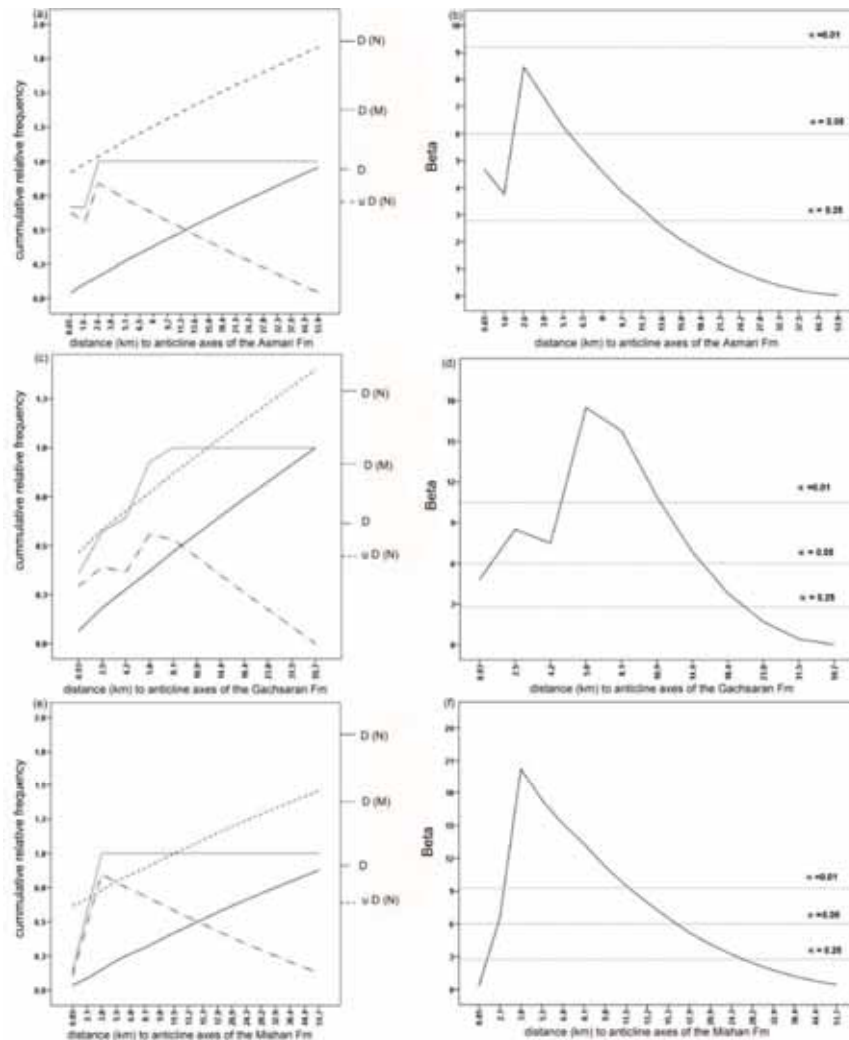


**Figure 3.7:** Graphs of cumulative relative frequency of distances at heavy oil or asphalt seep locations (D (M)) and non-heavy oil or asphalt locations (D (N)) around structural units of the three Formations and corresponding graphs of  $\beta$ -statistics of differences (D) between the cumulative relative frequency curves, the Dezful Embayment. D and u D (N) represent spatial association of seeps with structures and confidence band for  $\alpha=0.01$  respectively. (a) and (b) show the analysis of the Spatial association between heavy oil or asphalt and anticline axis of the Asmari Formation; (c) and (d) represent the spatial association between heavy oil or asphalt and anticline axis of the Gachsaran Formation; (e) and (f) show the analysis of the spatial association of heavy oil or asphalt seeps with the Mishan Formation.

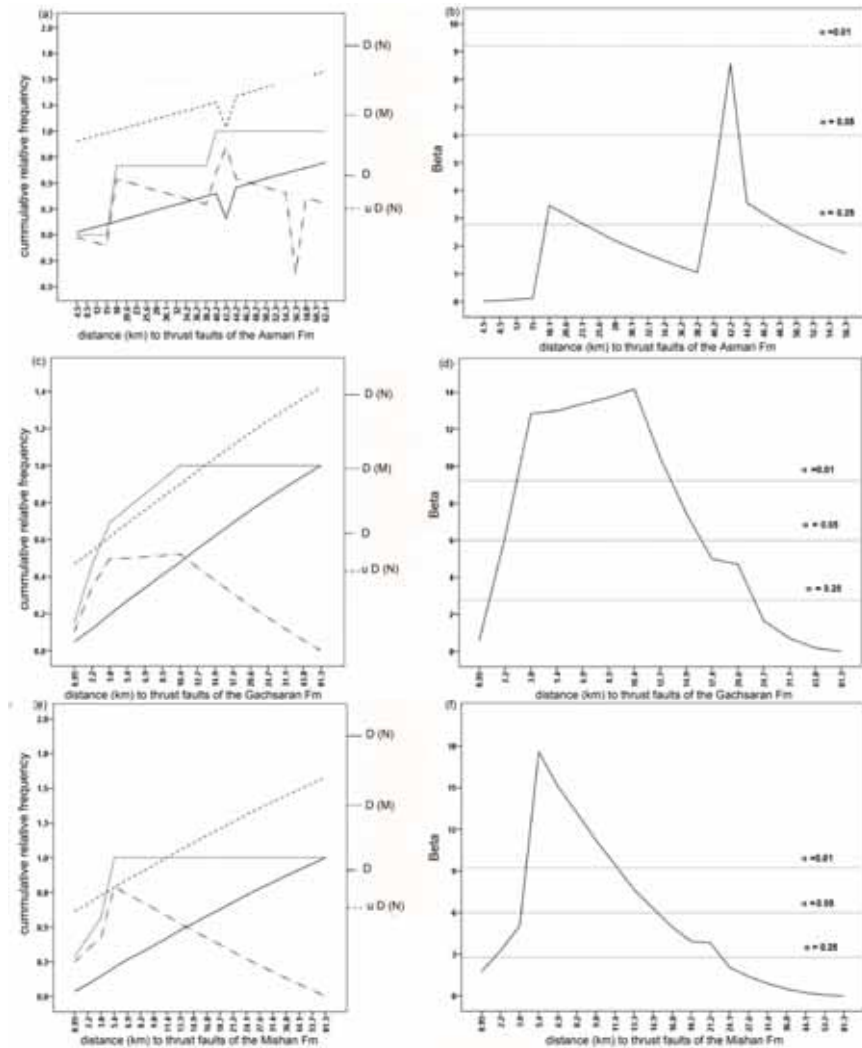


**Figure 3.8:** Graphs of cumulative relative frequency of distances at heavy oil or asphalt seep locations (D (M)) and non-heavy oil or asphalt locations (D (N)) around thrust faults of three Formations and corresponding graphs of  $\beta$  -statistics of differences (D) between the cumulative relative frequency curves, the Dezful Embayment. D and u D (N) represent spatial association of seeps with structures and confidence band for  $\alpha=0.01$  respectively. (a) and (b) show the analysis of spatial association between heavy oil or asphalt seeps and thrust faults of the Asmari Formation; (c) and (d) represent the spatial association between heavy oil or asphalt seeps and thrust faults of the Gachsaran Formation; and (e) and (f) show the spatial association between heavy oil or asphalt seeps and thrust faults of the Mishan Formation.

Figure 3.9 shows the analyses of spatial association of Gach-e-tursh with structures in the Mishan and Gachsaran Formations. There are statistically significant (at  $\alpha=0.01$ ) positive spatial associations between Gach-e-tursh and structures in the Gachsaran Formation (Figures 3.9a and 3.9c). The two peaks in the  $D$  and  $\beta$  curves (Figure 3.9b) imply that there are two groups of Gach-e-tursh with respect to anticline axes in the Gachsaran Formation. The first group is comprised of about 78% of the Gach-e-tursh located about an average of 5.8 km away from anticline axes. The second group is comprised of about 22% of Gach-e-tursh located about an average of 10.9 km away from anticline axes. There are also two peaks in the  $D$  and  $\beta$  curves of the spatial association of the Gach-e-tursh with thrust faults in the Gachsaran Formation. The first group is comprised of about 85% of the Gach-e-tursh located about an average of 5.4 km away from thrust faults. The second group is comprised of about 15% of Gach-e-tursh located about an average of 10.4 km away from thrust faults.

The Gach-e-tursh has statistically significant (at  $\alpha=0.01$ ) positive spatial associations with structures in the Mishan Formation (Figures 3.9e and g). The positive spatial association is optimal at 6.8 km of the anticline axes (Figure 3.9f). The two peaks in the  $D$  and  $\beta$  curves (Figures 3.9g and h) imply that there are two groups of Gach-e-tursh with respect to thrust faults of the Mishan Formation. The first group is comprised of about 63% of the Gach-e-tursh located about an average of 5.4 km away from thrust faults. The second group is comprised of about 37% of Gach-e-tursh located about an average of 15 km away from thrust faults.

Sulphur springs have positive spatial association with anticline axes and thrust faults in the Gachsaran Formation (Figures 3.10a and c). Within 2 km of anticline axes and thrust faults in the Gachsaran Formation, there are at least 70% and 50% of known sulphur springs, respectively. The two peaks in the  $D$  and  $\beta$  curves (Figures 3.10c and d) imply that there are two groups of sulphur springs in the area. The first group is comprised of about 50% of the sulphur springs located about an average of 2.2 km away from thrust faults of the Gachsaran. The second group is comprised of about 50% of springs located about an average of 10.4 km away from thrust faults in the Gachsaran Formation. In the Gachsaran Formation, the positive spatial association of sulphur springs with anticline axes is stronger than with thrust faults.

Sulphur springs show significant spatial associations (at  $\alpha= 0.01$ ) with anticline axes and thrust faults in the Mishan Formation (Figures 3.10e and g). These associations are optimal within 5.5 km of anticline axes and 5.4 km of thrust faults (Figures 3.10f and h).

By means of spatial association analysis, it is possible to rank the individual sets of geological features in terms of their relative importance as controls on the

occurrences of each sub-set of hydrocarbon seeps. In the distance distribution method, a basis for this ranking is the ratio of the value of  $D(M)$  to the value of the  $D(N)$  at the optimal distance of optimal positive spatial association of a set of geological feature (Carranza, 2009a). As summarized in Table 3.2, oil and gas seeps are mostly associated with the Mishan Formation and with structures in that formation. This finding suggests that hydrocarbons migrated upwards in the stratigraphy in the Dezful Embayment.

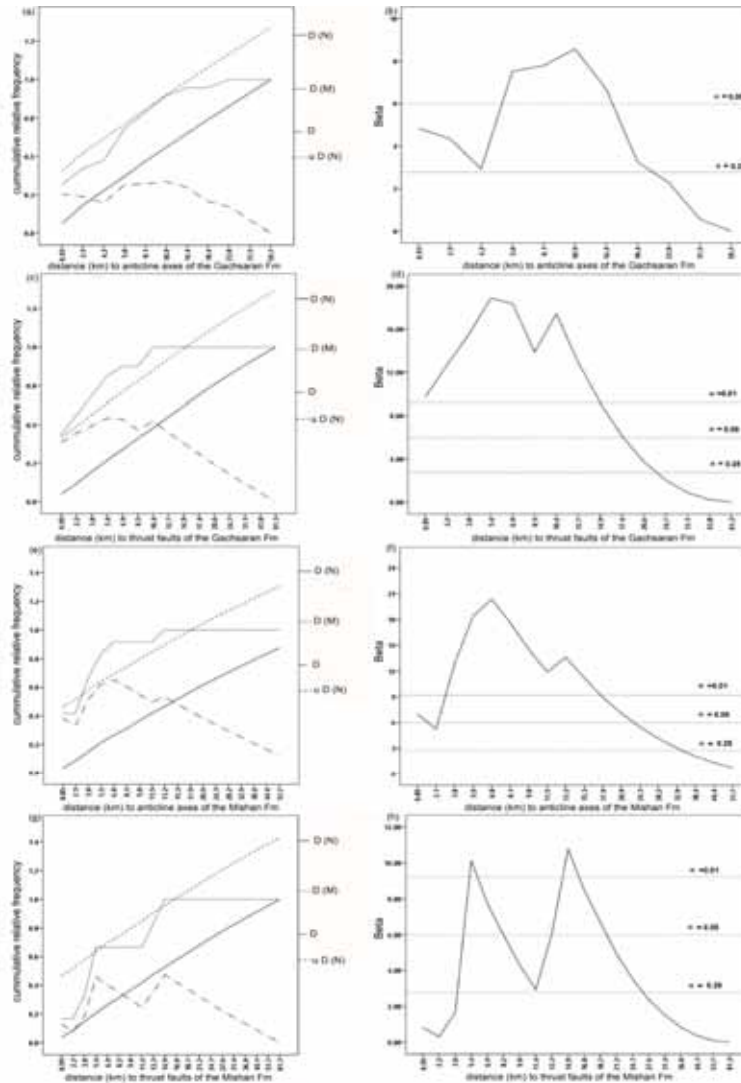


**Figure 3.9:** Graphs of cumulative relative frequency of distances at Gach-e-tursh locations (D (M)) and non-seep locations (D (N)) around structural units of the Gachsaran and Mishan Formations and corresponding graphs of  $\beta$ -statistics of differences (D) between the cumulative relative frequency curves, the Dezful Embayment.  $D$  and  $u D$  (N) represent spatial association of seeps with structures and confidence band for  $\alpha=0.01$  respectively. (a) and (b) show the analysis of spatial association between Gach-e-tursh and anticline axis of the Gachsaran Formation; (c) and (d) represent the spatial association between Gach-e-tursh and thrust faults of the Gachsaran Formation; (e) and (f) show the analysis of spatial association between Gach-e-tursh and anticline axis of the Mishan Formation; and (g) and (h) show the analysis of spatial association between Gach-e-tursh and thrust faults of the Mishan Formation.

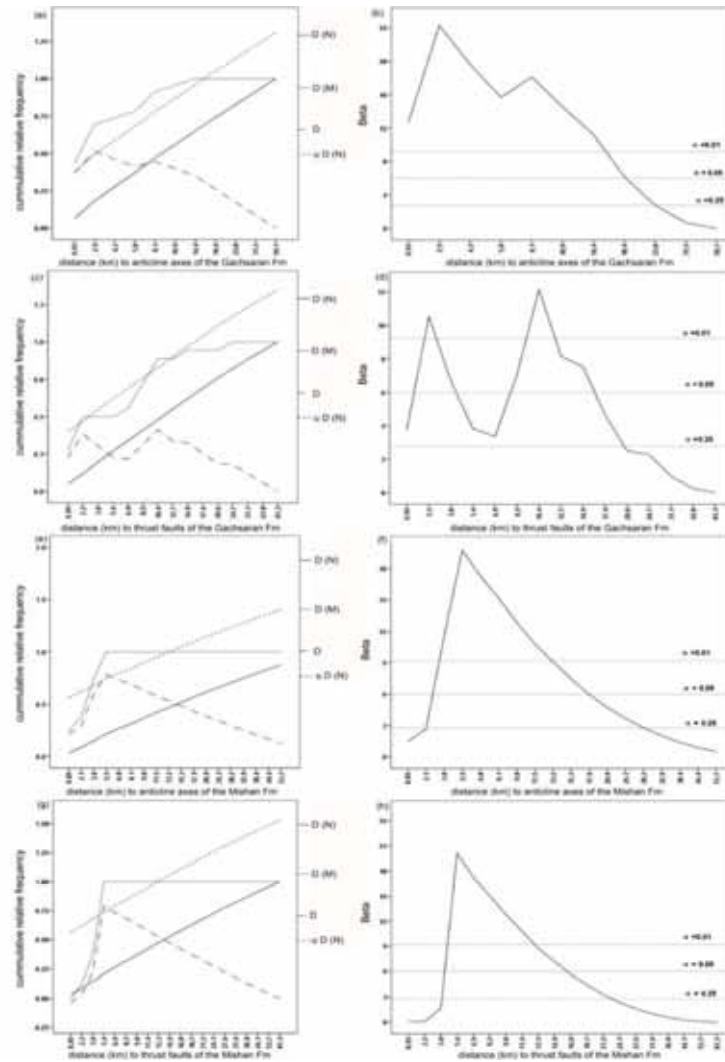


**Figure 3.10:** Graphs of cumulative relative frequency of distances at sulphur springs locations (D (M)) and non-seep locations (D (N)) around structural units of the Gachsaran and Mishan Formations and corresponding graphs of  $\beta$ -statistics of differences (D) between the cumulative relative frequency curves, the Dezful Embayment. D and u D (N) represent spatial association of seeps with structures and confidence band for  $\alpha=0.01$  respectively. (a) and (b) show the analysis of spatial association between sulphur springs and anticline axis of the Gachsaran Formation; (c) and (d) represent the spatial association between sulphur springs and thrust faults of the Gachsaran Formation; (e) and (f) show the analysis of spatial association between sulphur springs and anticline axis of the Mishan Formation; and (g) and (h) show the analysis of spatial association between sulphur springs and thrust faults of the Mishan Formation.

**Table 3.2** Summary of statistically significant results of analyses of spatial associations between each sub-set of hydrocarbon seeps and individual sets of structural features of the Formations having positive spatial associations with seep.

Summary of statistically significant results of analyses of spatial associations between heavy oil or asphalt seeps and individual sets of structural features of three Formations having positive spatial associations with seeps				
Structural features	Distance (d) of optimal positive spatial association	Values of D (M) at d (see Figs. 6 and 7)	Values of D (N) at d (see Figs. 6 and 7)	Values of D(M):D(N) at d
Anticline axes of the Asmari Fm	2.6	100	0.16	6.2
Anticline axes of the Gachsaran Fm	5.8	0.93	0.37	2.5
Anticline axes of the Mishan Fm	3.8	1	0.14	<b>7.1</b>
Thrust faults of the Gachsaran Fm	10.4	1	0.48	2
Thrust faults of the Mishan Fm	5.4	1	0.2	5
Summary of statistically significant results of analyses of spatial associations between <i>Gach-e-tursh</i> and individual sets of structural features of tow Formations having positive spatial associations with seeps				
Structural features	Distance (d) of optimal positive spatial association	Values of D (M) at d (see Fig. 8)	Values of D (N) at d (see Fig. 8)	Values of D(M):D(N) at d
Anticline axes of the Gachsaran Fm	10.9	0.89	0.55	1.6
Anticline axes of the Mishan Fm	6.8	0.91	0.26	<b>3.5</b>
Thrust faults of the Gachsaran Fm	5.4	0.81	0.26	3.1
Thrust faults of the Mishan Fm	14.9	1	0.52	1.9
Summary of statistically significant results of analyses of spatial associations between sulphur springs and individual sets of structural features of tow Formations having positive spatial associations with seeps				
Structural features	Distance (d) of optimal positive spatial association	Values of D (M) at d (see Fig. 9)	Values of D (N) at d (see Fig. 9)	Values of D(M):D(N) at d
Anticline axes of the Gachsaran Fm	2.5	0.69	0.18	3.8
Anticline axes of the Mishan Fm	5.5	1	0.2	<b>5</b>
Thrust faults of the Gachsaran Fm	10.4	0.88	0.47	1.9
Thrust faults of the Mishan Fm	5.4	1	0.2	5

### **3.5. Conceptual modeling of occurrence of hydrocarbon seeps in the Dezful Embayment**

The strong positive spatial associations of oil seeps and products of gas seeps alteration such as sulphur springs and Gach-e-tursh with the Mishan Formation and with anticline axes and thrust faults in that formation (Table 3.2) imply that densities of hydrocarbon seeps are not decreased upwards in the stratigraphy. The results of spatial association analyses (Figures 3.7 and 3.8) imply that there are probably two groups of heavy oil or asphalt seeps. The first group is spatially associated with the Asmari anticlines exposed to the surface. The occurrence of this first group of seeps could be due to the final exhaustion of former oil accumulations in the Asmari reservoir. The second group is spatially associated with the Gachsaran cap rock and the overlying Mishan Formation, where heavy oil or asphalt seeps showed stronger positive spatial associations with structures in the Mishan Formation than in the Gachsaran cap rock (Table 3.2). Where the Gachsaran Formation is exposed to the surface and where it is overlain by the Mishan Formation, heavy oil or asphalt seeps show spatial associations with associated structures (Figure 3.11a). Although the Gachsaran Formation has flowed by salt tectonics (Berberian, 1995) resulting in disharmonic relationship between folds in the surface and evaporites in the subsurface, oil likely escaped through prominent NW-SE and NE-SW trending faults and fractures formed during the Miocene syntectonic deposition of the Gachsaran Formation and/or through subsidiary N-S and NE-SW trending fractures formed by the reactivation of basement faults. In the former case, when oil migrated to pre-existing structures in the Asmari reservoir sealed by the Gachsaran cap rock in the late Miocene-Pliocene, hydrocarbons may have been localized in fractures related to salts and/or in NW-SE faults in SW flanks of anticlines. Later, localized hydrocarbons re-migrated upwards due to active tectonics in the area. The second case could have happened when N-S and NE-SW trending fractures formed by the shortening and the reactivation of basement faults breached the seal or superimposed the former structures.

When the Gachsaran Formation was buried (Figure 3.11b), it likely acted as a detachment zone such that overlying formations may have been folded into anticlines. The axes of those anticlines were likely displaced to the SW with respect to fold crests within underlying strata (cf. Sherhati et al., 2005; Allen and Talebian, 2011). In this case, oil could have migrated through thrust faults in the southwestern flank of the Gachsaran cap rock and joined the NNE-SSW trending fault-related fractures. The oil could have lost its lighter components and occurred as heavy oil or asphalt seeps in the Mishan Formation at the surface. Hydrocarbon seeps could have occurred at the contact zone of the Mishan Formation with the Gachsaran cap rock. They likely found active faults related to salts of the cap rock and a network of open fractures as migration pathways to reach the surface. Because the SW flanks of the Gachsaran

anticlines are thrust, heavy oil or asphalt seeps likely occurred at the southwestern parts of structures. In addition, the low permeability of marl of the Mishan Formation would have not allowed hydrocarbons to migrate to the surface through this Formation in the subsurface. The foregoing interpretations of results of the spatial analyses of heavy oil or asphalt seeps with structures and lithologic units suggest, therefore, that subsurface fractures and faults of the Gachsaran cap rock, particularly at the southwestern flank, provided favorable pathways for the vertical migration of these seeps to reach the surface.

The positive spatial associations of Gach-e-tursh and sulphur springs with the Gachsaran and Mishan structures (Figures 3.9 and 3.10) imply that gas seeps have migrated upwards in stratigraphy and have produced these alterations in the respective formations. Gas-free oil seeps are rare or do not exist because oil buoyancy itself was not enough to reach the surface. However, gas may have segregated from oil in the subsurface and probably escaped through permeable fractures even when seal was effective and not breached by faults. Thus, gas may have probably migrated through NW-SE, and NNE-SSW trending fractures within the Gachsaran cap rock. Products of gas seep alteration such as Gach-e-tursh and sulphur springs have occurred within the Gachsaran Formation (Figure 3.11a) or at the contact zone of the Gachsaran Formation with the Mishan Formation (Figure 3.11b). The configuration of Gach-e-tursh at the surface as vein fillings or matrix cement could be an important factor for better understanding of gas seeps pathways mineralization. Gas may have entered basinal water and have changed its chemical properties. This water likely rose up and was enriched in sulphate by dissolution of anhydrite in the Gachsaran Formation. This action may have produced features such as galleries at the contact between limestone and gypsum following maximum dip in rhythmic units of the Gachsaran cap rocks in the subsurface and/or at the sharp contact zone of the Gachsaran Formation with the Mishan Formation. Such features could have been potential conduits for fluid flow in the subsurface.

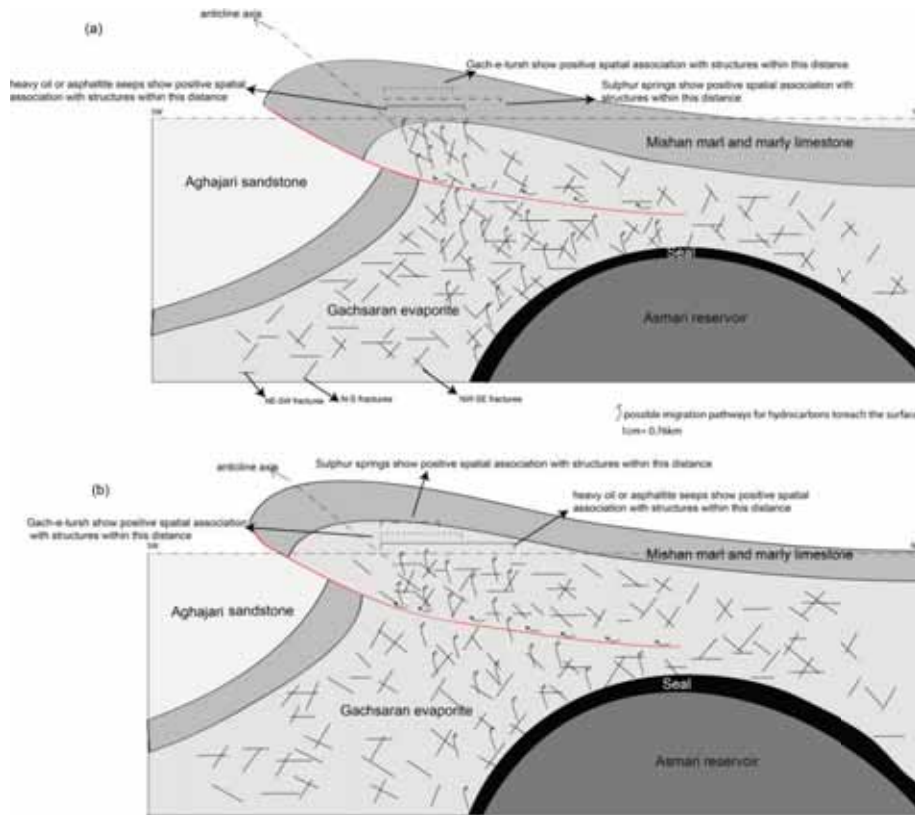


**Figure 3.11:** Conceptual model for the occurrence of onshore hydrocarbon seeps and their alteration products in the Dezful Embayment, (a) when the Gachsaran Formation has exposed at the surface and (b) when it is overlaid by the Mishan Formation.

### 3.6. Discussion

The results of Fry analyses of hydrocarbon seep locations are useful for visual interpretations of which structures likely controlled the occurrence of hydrocarbon seeps in the Dezful Embayment. The syntheses of those results with the results of analyses of spatial association of seeps with geological features are useful for development of a conceptual model for the occurrence of onshore hydrocarbon seeps in the Dezful Embayment. In this conceptual model, we suggest that hydrocarbon seeps and their alteration products likely occur in the Mishan Formation. In areas where the Gachsaran cap rock does not outcrop, it is likely that hydrocarbon seeps and their alteration products occur on the surface of the overlying Mishan Formation.

The deformation of the petroleum basin in the Dezful Embayment has resulted in faults and fractures, which were likely potential pathways for hydrocarbons

to migrate upwards to the surface. The structural disharmony between the underlying carbonate reservoir and overlying folds, which resulted from salt tectonics, likely played a role in the lateral displacement of hydrocarbon seeps from their source rocks. However, oil cannot flow except under well conditions, governed by factors such as viscosity and capillarity. In some areas, oil was likely trapped at the water table where it had biodegraded or had flowed downward to emerge groundwater, although the associated gas could have escaped into the surface rocks.

Many oil fields in SW of Iran have a gas cap (Alshahran and Nairn, 1997); thus, a better understanding of the occurrences of gas seeps and their alteration products may benefit from petroleum-finding survey. However, an advantage of spatial analyses in the present study is the provision of empirical evidence for establishing a conceptual model of geological controls on hydrocarbon seep occurrence. Therefore, the methods of spatial analyses demonstrated here could provide geo-information that can be used as scientific basis for selecting potential areas for investigation of hydrocarbon entrapment.

Nevertheless, results of the application of the spatial analytical methods used in the present study can be undermined by the (lack of) quality and completeness of the datasets used and by the scale compatibility between the datasets. The datasets used here were derived from geological maps compiled by the Iranian oil company. Thus, the datasets used are compatible in scale although they may not be complete. Accordingly, there is a possibility that hydrocarbon seeps are associated with minor structures that were not mappable at the scale of map shown in Figures. 3.1 and 3.2. It follows that the quantified spatial associations between hydrocarbons seeps and structures presented in this study are tentative. This means that the analyses and the conceptual model presented must be updated as new data become available.

### **3.7. Concluding remarks**

With the aid of spatial pattern and spatial association analyses, a conceptual model for the occurrence of oil and gas seeps in the Dezful Embayment was developed. Oil seeps likely have migrated along NW-SE and NE-SW trending faults and fractures in SW flanks of anticlines, whereas gas seeps likely have escaped to the surface through prominent NW-SE and N-S trending faults and fractures. The positive spatial associations of seeps with the Mishan Formation imply that the density of seeps is not decreased upwards in the stratigraphy suggesting upward migration of hydrocarbons through permeable micro-fractures and micro-pores in their strata. Salt tectonics has played an important role in the lateral migration of hydrocarbon seeps from their sources.



#### **4. Spectral and geochemical characterization of onshore hydrocarbon seep-induced alteration in the Dezful Embayment, SW Iran<sup>3</sup>**

---

<sup>3</sup> This chapter is based on the following paper: Sanaz. Salati, Frank J.A. van Ruitenbeek, J. Boudewijn de Smeth, Freek D. van der Meer. Spectral and geochemical characterization of onshore hydrocarbon seep-induced alterations in the Dezful Embayment, SW Iran. In: American Association of Petroleum Geologists (AAPG Bulletin), (Accepted).

## **Abstract**

The presence of hydrocarbon seeps at the surface is an indirect evidence of the presence of mature source rocks within a geological system at depth. Chemical changes in the environment of surface rocks caused by hydrocarbon seeps form mineralogical alterations. To determine the nature of alterations and the influence of lithologies and types of seeps, rock samples were collected from altered and unaltered Gachsaran (evaporite) and the Mishan (marly limestone) formations in the Dezful embayment, SW Iran, and subsequently analyzed. Reflectance spectroscopy, bulk rock/wet chemical analyses, and sulfur, carbon and oxygen isotopic analyses were successfully used to delineate surficial alterations and relate alterations to hydrocarbons seeping from underlying reservoirs. In addition, the boosted regression trees (BRT) method was used to successfully predict the presence of alterations from spectral indices. Comparisons of geochemical data and spectral data of altered evaporites and altered marly limestones showed that the minerals within alteration facies have distinctive spectral, chemical, and isotopic signatures. Gas-induced alterations were characterized by the formation of gypsum and native sulfur and depletion in  $^{34}\text{S}$ . The released  $\text{H}_2\text{S}$  (obtained from bacterial sulfate reduction) reacted with gypsum in the evaporite sediments and calcite in the marly limestone formations which led to precipitation of secondary gypsum and native sulfur. Oil induced alterations were characterized by formation of secondary calcite and depletion in  $^{13}\text{C}$ . The oxidation of seeping oil and reactions between this oil and host rocks caused precipitation of secondary calcite within the both formations. The combination of field work data and laboratory analyses (spectral and geochemical) showed that there is a connection between surficial alterations and underlying petroleum reservoirs, which can be used in explorations campaigns.

#### 4.1. Introduction

Hydrocarbon seeps and their surface expressions are commonly found throughout the world in sedimentary basins containing oil and gas reserves. The presence of seeps at the surface is not indicative of the size of a petroleum basin and they may even be located over a non-productive basin. However, it is an indirect evidence of the presence of mature source rocks within a geological system at depth. Hydrocarbon macroseeps manifest themselves as the visible presence of oil and gas seeping to the surface; while hydrocarbon microseeps have no visible and direct evidences for their occurrences, seeping probably vertically or near-vertically from the reservoir to the surface (Abrams, 2005). The presence of hydrocarbon macroseeps at the surface is direct evidence of hydrocarbon migration in a separate phase. As hydrocarbon moves to the surface, they re-equilibrate to oil and gas. They can be in contact but are often segregated due to differences of migration pathways such as spillage of oil, capillary leakage of oil and gas, trapping configuration and cap rock behavior (Matthews, 1996). At the surface, escaped hydrocarbons oxidize and form reducing environment that favor the formation of mineralogical and botanical anomalies. In addition, slightly acidic conditions are created due to the production of CO<sub>2</sub>, H<sub>2</sub>S, and organic acids (resulted from microbial oxidation of hydrocarbons). Chemical changes in the environment of surface rocks cause mineralogical alterations such as red beds bleaching, clay formation and uranium enrichment, formation of secondary carbonates, sulfides, and magnetic minerals (Schumacher, 1996). The patterns of alteration minerals have important implications for detection of hydrocarbon pathways as they show permeable zones within the cap rock where the hydrocarbons leak to the surface.

Integration of spectroscopic and geochemical data were successfully used to identify microseeps alteration-related minerals and chemical changes and mapping of their spatial distribution within sandstones of Bahia state in Brazil, Lisbon valley in Utah, and Wyoming (Fillho, 2002; Khan and Jacobson, 2008; Petrovic et al., 2008). In this study, this is attempted in areas of evaporitic and marly limestone formations, which are affected by hydrocarbon macroseeps. Evaporite formations are some of the most effective seals in half of the world's largest oil fields (Warren, 2006). Characterization of hydrocarbon seeps-induced alterations within evaporite seals would allow us to map spatial distributions of those alterations, which could be analogous to the spatial pattern of alterations in the subsurface. Such studies provide a framework for identifying permeable zones and evaluating the efficiency of cap rocks related to petroleum systems.

The Zagros belt is a good natural laboratory to study oil and gas seeps and their manifestations in various types of geological formations. Hydrocarbon seeps

and their associations typically occur in the Gachsaran evaporite (cap rock) and its overlying Mishan marly limestone formation (Salisbury et al., 1993). The spatial distribution of alterations related minerals within the Gachsaran cap rock and the Mishan Formation and the relationships between these types of alterations are important for interpreting hydrocarbon migration pathways. The main objectives of this study are (a) getting a better understanding of oil and gas migration through the stratigraphy in relation to the various types of seeps in the Zagros belt by applying geochemical and reflectance spectroscopy techniques and (b) investigate the potential of detection of hydrocarbon seep-induced alterations for petroleum explorations.

## **4.2. Materials and methods**

### **4.2.1. Field sampling**

Field work took place in the April 2012 in the Dezful Embayment, where active oil and gas seeps are located in both evaporite and marly limestone formations so as to investigate the influence of lithology on seeps-induced alterations type (Figure 4.1). Rock samples were collected along horizontal and vertical transects crossing active seeps in order to obtain samples both within as well as outside of the altered areas (Figure 4.2). In addition, unaltered rock samples were collected for each lithological unit in the same geographic zone but at some distances away from the seeping areas. The location of seeps was based on information primarily from existing geological maps and on information about active seeps locations provided by the Iranian Oil Company.



**Figure 4.1:** Typical gas (a and b) and oil (c and d) seeps in the Gachsaran and Mishan Formations in the Dezful Embayment, SW, Iran.

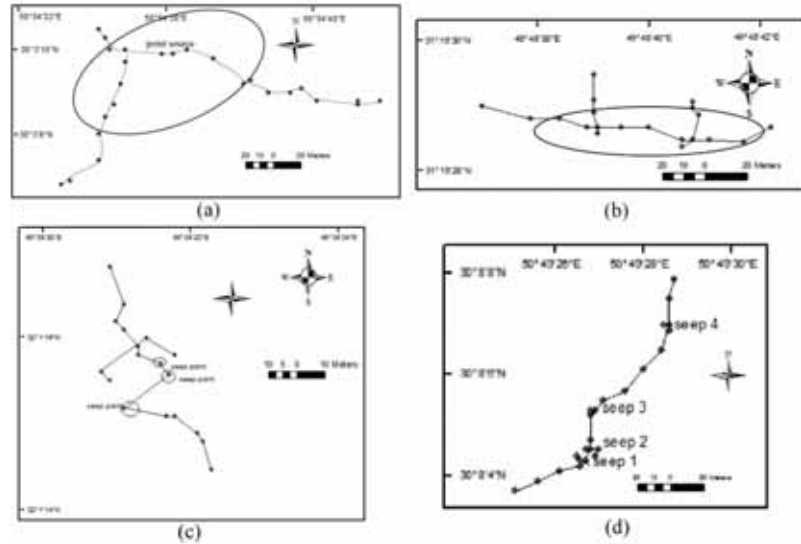


**Figure 4.2:** Sampling profiles over gas seeping area (**a** and **b**) and over oil seeping area (**c** and **d**). Samples were taken from the Gachsaran Formation (**a** and **c**) and the Mishan Formation (**b** and **d**). Circles show boundaries of alteration zones.

#### 4.2.2. Spectral analysis

Reflectance spectra in the range of 0.4 to 2.4  $\mu\text{m}$  of rock samples were measured in the laboratory with an ASD FieldSpec using a contact probe. Raw spectra were corrected using the ViewSpecPro (splice correction) and then converted to ASCII format file to create spectral library using ENVI software. The mineralogy of spectra was interpreted by comparing spectral features at different wavelengths with library spectra and by using prior knowledge about the lithology of the study area. Diagnostic spectral wavelengths ranges showing the differences were selected for further analyses. For each seeping area, the dominant absorption depth of spectral features was measured to characterize different rock types. The depth of absorption features between altered and unaltered samples vary because of different abundances of the detected minerals. The depth of an absorption feature in a reflectance spectrum was calculated by subtraction of the reflectance value at peak shoulders by the reflectance value at reflectance minimum at the center of the absorption feature of continuum removal of the spectrum (Clark and Roush, 1984; van der Meer, 2004):

$$D(\lambda) = 1 - R_c(\lambda) \quad (1)$$

Where  $R_c$  is the continuum removed spectrum and  $(\lambda_c)$  is the wavelength position with the maximum depth.

### **4.2.3. Statistical analysis of spectra**

In this study, the boosted regression trees (BRT) method was used to predict the presence of alterations from absorptions depth of diagnostic spectral features. This method has been successfully applied for prediction in economics (Schonlau, 2005), computer sciences (Tyree et al., 2011) and ecology (Elith et al., 2008). The BRT is a machine learning algorithm that uses the technique of boosting to combine large numbers of simple tree models to improve predictive performance (Elith et al., 2006; Elith et al., 2008). Machine learning methods use an algorithm to learn the relationship between the response and its predictor instead of starting with a data model (Breiman, 2001). The BRT fits nonlinear relationships by combining two algorithms of regression trees (from regression and classification tree groups of models) and boosting (builds and combines several models).

In a real geological situation, measurements may show high concentrations of certain chemical elements or deep absorption features related to high mineral abundances. These measurements are key factors in interpretation of geological processes such as seeps-induced alterations. They are not outliers but exceeded amounts, and they may affect the accuracy of produced predictive models. The BRT is not sensitive to outliers or anomalously high values and the method assumes that the data generating processes are complex and unknown and it tries to find the dominant pattern.

The BRT model used here is a form of logistic regression that models the probability that alteration occurs,  $y=1$ , at a location with covariates  $X$ ,  $P(y=1 | X)$ . This probability is modeled via a logit:  $\text{logit } P(y=1 | X) = f(X)$ . The models were fitted in R version 2.15.3 (R development Core Team 2006), using generalized boosted regression models (gbm) package version 2.0-8 (Ridgeway, 2006). The learning rate and number of trees are two important parameters controlling prediction errors. The learning rate shrinks the contribution of each tree as it is added to the model. A low learning rate and 1000 trees were used to deal with over fitting of BRT for small number of samples (Elith et al., 2008).

One of the most important outputs of the BRT algorithm is the relative influence of predictors, which is measured based on the number of times a variable is selected for splitting, weighted by the squared improvement to the model as a result of each split and averaged over all trees (Friedman and Meulman, 2003). The model accuracy performance was evaluated by a threshold-independent metric; AUC (Area Under ROC Curve) (Fielding and Bell, 1997). A ROC curve is constructed from false positive rates (X axis) and true positive rates (Y axis). An area of 1 shows the best model (perfect discrimination) and an area  $< 0.5$  indicates discrimination worth than chance. For each area, the dataset (absorption depth of diagnostic spectral features) were randomly partitioned into calibration and validation datasets (i.e. 70% for

calibration and 30% for validation). The repeated sub-sampling validation was applied for evaluation the performances of models. This method randomly splits a dataset into training and validation data. The model is calibrated with training and the predictive accuracy is assessed by validation data. Results of splits are then averaged (Kohavi, 1995).

#### 4.2.4. Geochemical analyses

A portable XRF analyzer (Niton XL3t GOLDD) in a laboratory set-up with Helium gas purging was used to analyze whole rock for major and trace elements of altered and unaltered samples. Statistical comparison (t-test) analysis was performed to compare the average concentration of major and minor elements from altered and unaltered samples.

Where both gypsum and calcite were present (evaporites affected by oil seeps and marly limestones affected by gas seep), water and acid extraction procedures were applied to determine gypsum and calcite contents of samples. These analyses are based on the dissolution of gypsum in water and dissolution of all calcium present in carbonate form ( $\text{Ca}^{2+}$ ) in hydrochloric acid. Because of the low solubility of gypsum in distilled water (2.6 gr/L at 25°C), the ratio of 0.1gr: 60ml was chosen for the rock powder: water ratio. Suspensions were mixed on shaker overnight and the  $\text{Ca}^{2+}$  content of solutions was measured by ICP-OES (Varian Liberty II instrument). It is assumed that all of the  $\text{Ca}^{2+}$  content of the extraction solutions originates from dissolved gypsum. To measure acid extractable  $\text{Ca}^{2+}$ , 1 gram of rock powder was mixed with 30 ml distilled water after which 5 ml concentrated HCl was added. Suspensions were mixed on a shaker overnight, and then 1 ml of the solutions was diluted twenty times followed by ICP-OES analysis. Calcite contents of samples were estimated by the Eq2:

$$\text{Calcite (\%)} = 2.5 \times (\text{acid extractable } \text{Ca}^{2+} - \text{water extractable } \text{Ca}^{2+} \text{ (gypsum)}) \quad (2)$$

Neither the spectral measurements, nor the Mg amounts determined by XRF indicated the presence of dolomite.

Altered and unaltered rock samples from both formations were analyzed for stable carbon ( $^{13}\text{C}$ ), oxygen ( $^{18}\text{O}$ ), and sulfur ( $^{34}\text{S}$ ) in order to determine the origin of surficial alterations. Two oil samples, thirty rock powder samples from gas seeping areas and thirty samples from oil seeping areas were analyzed for their isotopic composition in the Iso-Analytical laboratory, Cheshire, UK.

### **4.3. Results**

#### **4.3.1. Characterization of gas seep-induced alteration**

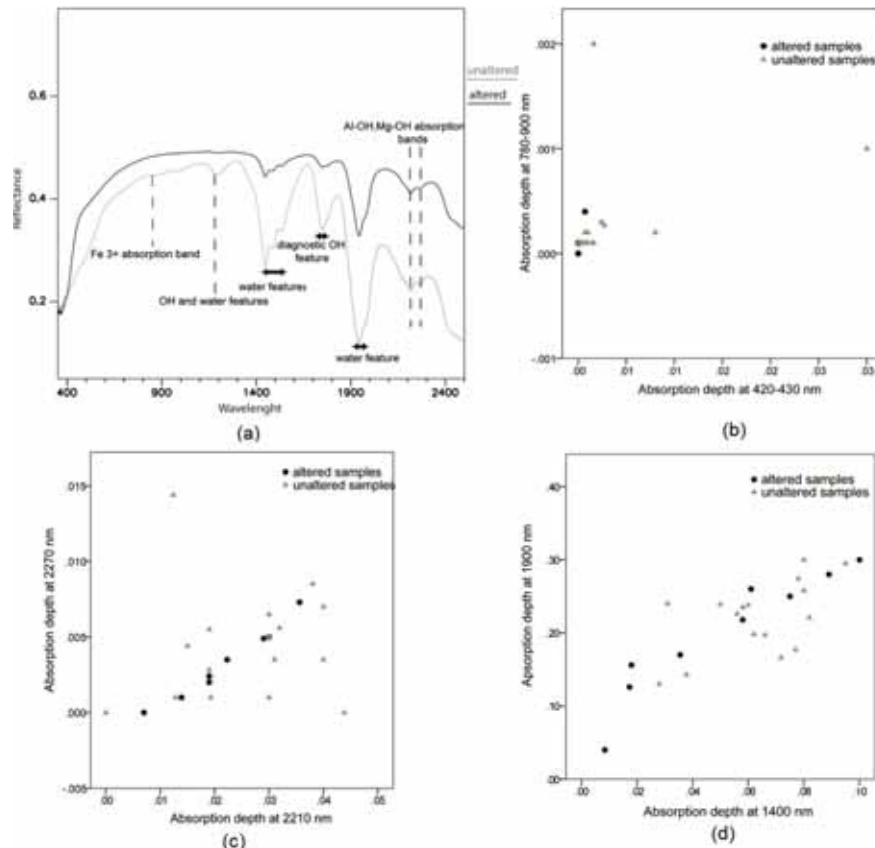
##### **4.3.1.1. Evaporite formation**

Figure 4.3a shows spectral signatures of gas-induced alterations and unaltered rocks within the Gachsaran evaporite in the Dezful Embayment. The unaltered samples exhibit shallow absorption features in near 0.43 and a broad absorption features near 0.8-0.9  $\mu\text{m}$  (Figure 4.3a), which can be related to the presence of iron bearing sulfate minerals such as jarosite (Cloutis et al., 2006). The unaltered evaporites shows distinctive spectral features of gypsum near 1  $\mu\text{m}$ , 1.4  $\mu\text{m}$ , 1.75  $\mu\text{m}$ , 1.9  $\mu\text{m}$ , a doublet at 2.21-2.27  $\mu\text{m}$ , and a drop at 2.4  $\mu\text{m}$  wavelengths (Figure 4.3a). Gas-induced alterations and unaltered evaporites have somewhat similar reflectance spectra, however, altered rocks lack any absorption features within the visible wavelength range (Figure 4.3b). Although both altered and unaltered samples show diagnostic features of gypsum in SWIR wavelengths, altered samples show shallower absorptions depth indicative of gypsum (Figures 4.3c and d) inferring that altered samples contain lower abundances of gypsum than unaltered samples. Figure 4.3d shows that secondary gypsum has lower water content than unaltered gypsum.

The boosted regression trees analysis (BRT) demonstrated that reflectance spectra successfully predicted the presence of hydrocarbon-induced alterations in the evaporite formation (Figure 4.4). The predicted powers of the fitted models are very good; the AUC has a mean value of 0.91. This means that evaporite rocks that were altered by gas seeps, have different spectral characteristics from the unaltered evaporites and that reflectance spectra can be used to successfully distinguish between the two groups of rocks. The spectral wavelengths ranges which are indicative of the presence of Fe bearing minerals and water have the largest contributions in the prediction modeling for the presence of gas-induced alterations (Figure 4.4). The gas-induced alterations (secondary gypsum) have less amounts of water and lack Fe bearing minerals.

The results of chemical analysis show that the chemical composition of altered evaporites is different from unaltered evaporites, which is consistent with the results of spectral analysis. The statistical comparison (t-test) between two average elemental concentrations from gas-induced alterations and unaltered Gachsaran evaporite samples showed that except for CaO and MgO, major oxides have significantly different concentration when comparing the altered and unaltered samples (Figure 4.5). It appears that the concentrations of these major oxides are lower inside the alteration zone of the Gachsaran evaporites (Figure 4.5). Sulfur (S) shows statistically significant differences between the two groups of rocks. The altered samples contain higher concentrations of S

than the unaltered samples. However, some of the unaltered Gachsaran evaporite samples contain sulfur concentrations higher than 19%. As pure marine gypsum has 19% of S, this indicates the presence of other sulfate minerals than gypsum e.g. jarosite.



**Figure 4.3:** Characteristic reflectance spectra and spectral parameters of altered and unaltered the Gachsaran evaporites; **(a)** spectra of gas-induced alterations and unaltered Gachsaran evaporites, **(b)** scatter plots of the depth of absorption features between 420-430  $\mu\text{m}$  related to Fe, **(c)** scatter plots of the depth of absorption features in the SWIR range related to gypsum, and **(d)** scatter plots of the depth of absorption features at 1.4 and 1.9  $\mu\text{m}$  related to water content.

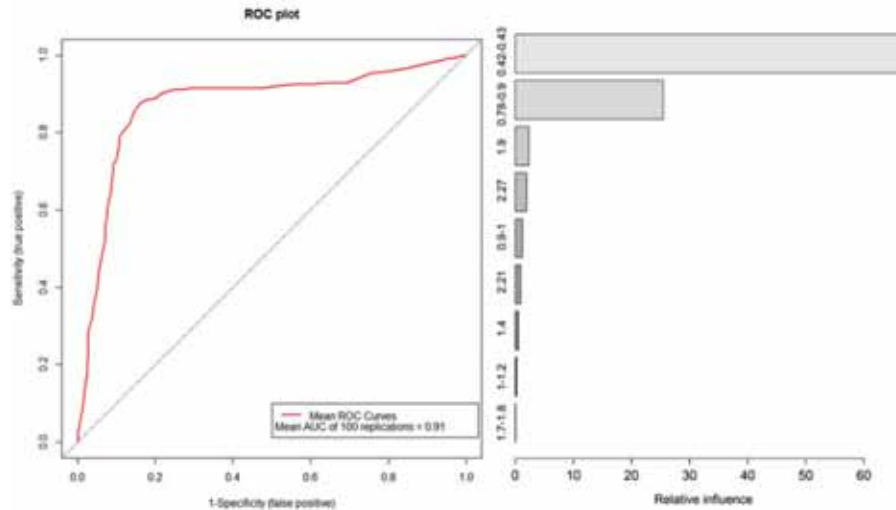


**Figure 4.4:** ROC curve of the predictive power of the BRT model on the presence/absence of gas-induced alterations and relative influences of absorption features on prediction models in the Gachsaran evaporites.

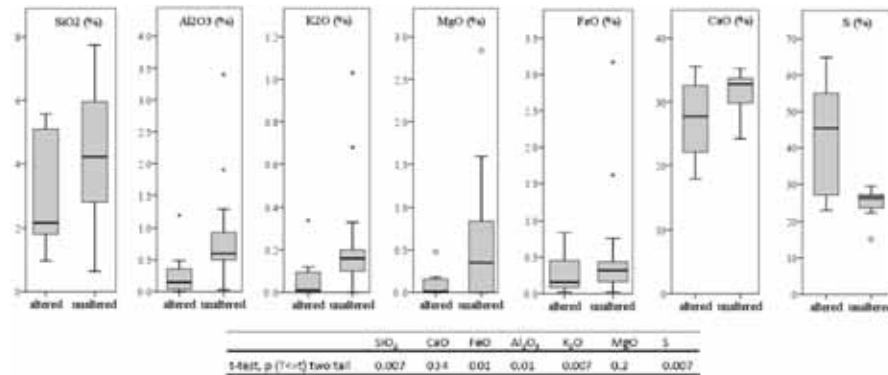


**Figure 4.5:** Box plots of major oxides and sulfur (S) concentrations in the Gachsaran evaporite samples including gas-induced alteration samples, southern of Dezful Embayment, and statistical comparison (t-test) between elemental concentrations from altered and unaltered Gachsaran evaporites.

### 4.3.1.2. Marly limestone formation

Figure 4.6a presents spectral signatures of gas-induced alterations and unaltered rocks in the Mishan marly limestone formation. Unaltered samples have an absorption feature in 0.4-0.45  $\mu\text{m}$  and a broad absorption feature between 0.8-0.9  $\mu\text{m}$  indicating the presence of iron bearing minerals in the Mishan formation such as goethite and clays and around 2.35, which is related

to the presence of calcite (Figure 4.6a). In addition, unaltered rocks contain absorption features at 2.2, 2.34-2.44  $\mu\text{m}$  indicating the presence of Al-OH containing clays such as illite. Most of altered samples lack any absorption features in the 0.8-0.95  $\mu\text{m}$  range. All altered rocks are characterized by absorption features at around 1, 1.4, 1.75, 1.9, 2.215, and 2.27 $\mu\text{m}$ . Gas-induced alterations show deep absorptions depth indicative the presence of gypsum (Figures 4.6c, and d), while unaltered marly limestones have deep absorption depth at 2.3  $\mu\text{m}$  caused by calcite (Figure 4.6b). Features at 1.4 and 1.9  $\mu\text{m}$  indicate the presence of high amounts of water (in gypsum) (Figure 4.6d).

The BRT analysis demonstrated that absorptions depth of diagnostic spectra successfully predict the presence of hydrocarbon-induced alterations in the Mishan marly limestones (Figure 4.7). The predictive powers of fitted models are very good; the AUC has mean value 0.92. This means that marly-limestone rocks that were altered by gas seeps have different spectral characteristics from the unaltered rocks and that reflectance spectra can be used to successfully distinguish between the two groups of rocks. The spectral wavelength ranges indicative for gypsum and calcite form the largest contributions in the predictive modeling of the presence of gas-induced alterations in the Mishan marly limestones (Figure 4.7) where calcite is converted to gypsum in the alteration zone of the marly limestone formation.

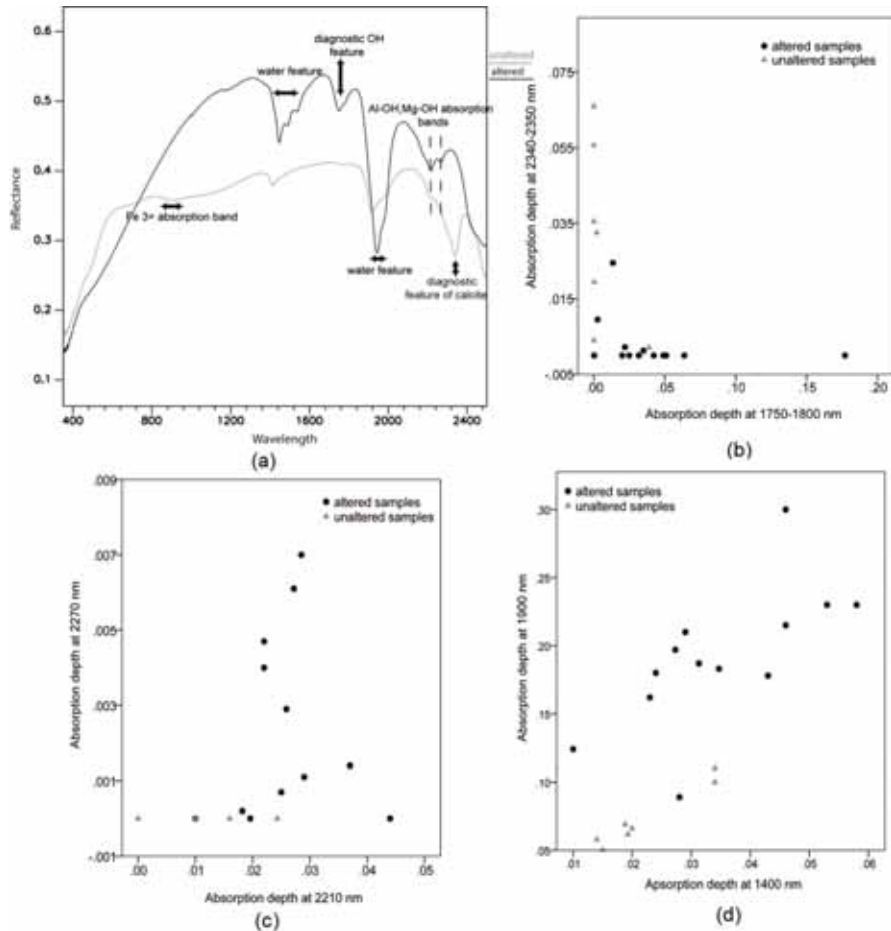


**Figure 4.6:** Characteristic reflectance spectra from the Mishan marly limestone; (a) presents spectral signatures of gas-induced alterations and characteristic Mishan marly limestone spectra, and (b) scatter plots represent absorption depth in SWIR range to distinguish calcite, (c) represent absorption depth in the SWIR range to distinguish gypsum in altered samples, and (d) shows the absorption depth of water features for unaltered and altered marly limestone samples.



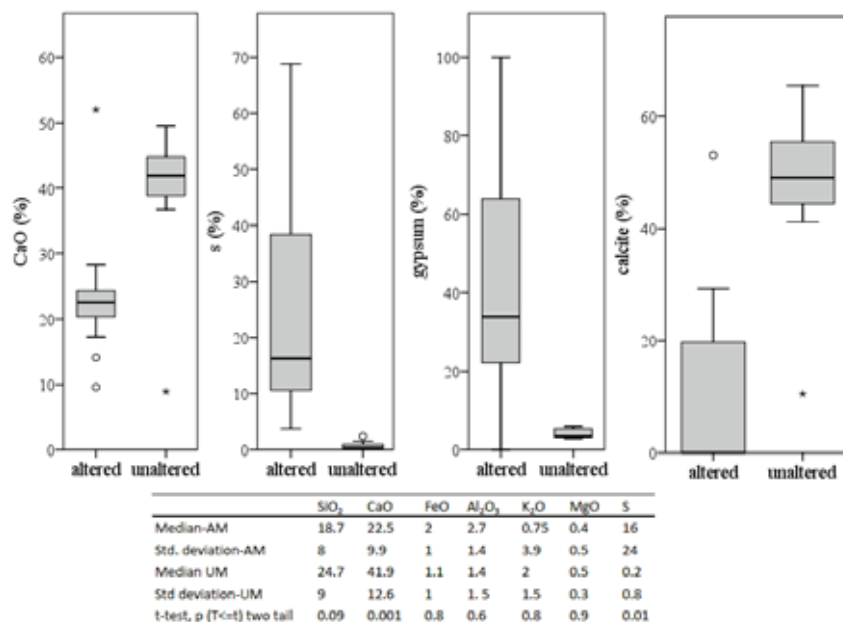


**Figure 4.8:** Box plots of XRF measured CaO, S, and wet chemical measured gypsum and calcite, and statistical comparison (t-test) between elemental concentrations from altered (marly limestone affected by gas seep) and unaltered Mishan marly limestone.

### 4.3.2. Characterization of oil seep-induced alteration

#### 4.3.2.1. Evaporite formation

Figure 4.9a shows spectral signatures of oil-induced alterations and unaltered rocks within the Gachsaran formation, NE of the Dezful Embayment. Unaltered rocks exhibit absorption features between the 0.5-1 $\mu$ m, which is indicative of iron bearing minerals. All unaltered rocks show diagnostic absorption features of gypsum and some of them contain features near 2.35  $\mu$ m, which indicated the presence of calcite. The variation within the group of unaltered rocks is caused by varying mineralogical composition within the Gachsaran Formation where occasionally limestone rich layers occur within predominantly gypsum-rich sequences in the area. Unaltered rocks have additional absorption bands at 2.10  $\mu$ m, 2.20  $\mu$ m, 2.30  $\mu$ m and 2.45  $\mu$ m caused by the effects of OH<sup>-</sup> in combination with aluminum and magnesium (Al-OH and Mg-OH) suggesting the presence of clay minerals such as illite and palygorskite. In contrast, altered rocks lack absorption features in the VNIR range and they lack indicative absorption features of gypsum. Instead, they have absorption features in 2.35  $\mu$ m and 2.15  $\mu$ m indicative of the presence of calcite and clays (Figure 4.9d). Oil-induced alterations within the Gachsaran formation contain less amounts of

water because of the conversion of gypsum to calcite (Figure 4.9b). Also those alterations show deeper absorptions depth at 2.4-2.5  $\mu\text{m}$  than unaltered samples, which might be related to clays (Figure 4.9d).

The BRT analysis demonstrated that spectral features successfully predicted the presence of oil-induced alterations in the Gachsaran evaporites (Figure 4.10). The predicted power of fitted models for the Gachsaran evaporites is fair; the AUC has mean values of 0.74. This shows that evaporite rocks that were altered by oil seeps have different spectral characteristics from the unaltered rocks and that reflectance spectra can be used to distinguish between the two groups of rocks. The spectral wavelengths ranges indicative of the presence of gypsum, calcite, clays, and water have the most contributions in the predictive modelling of the presence of oil-induced alterations in the Gachsaran evaporites (Figure 4.10).

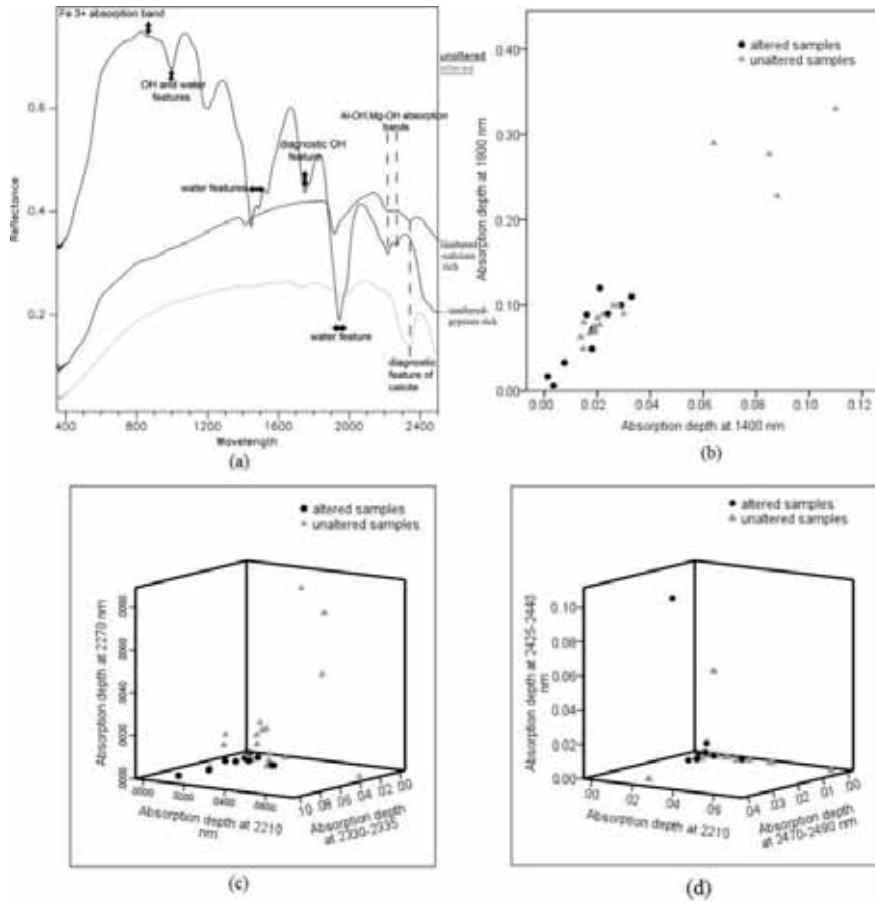


**Figure 4.9:** Characteristic reflectance spectra from the Gachsaran evaporites; (a) presents oil-induced alterations spectra and characteristic Gachsaran evaporites spectra, (b) shows the absorption depth of water features for unaltered and altered evaporites samples, (c) represents absorption depth in the SWIR range to distinguish gypsum in unaltered samples and calcite in altered samples, and (d) represents absorption depth in the SWIR range to distinguish clays.

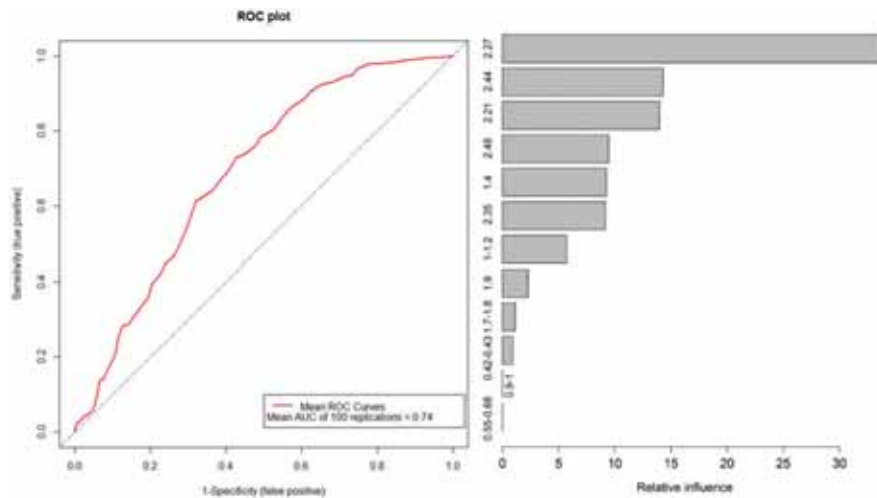


**Figure 4.10:** ROC curve of the predictive power of the BRT model on the presence/absence of oil-induced alterations and relative influences of absorption features on prediction models in the Gachsaran.

The results of chemical analysis show that the chemical composition of altered rocks is somewhat different from unaltered rocks, which is consistent with the results of spectral analyses. Major oxides show small differences between altered and unaltered samples (Figure 4.11). The results of wet chemical analysis for quantifying the contents of gypsum and calcite show that most of the altered and unaltered samples contain relatively high amounts of calcite. This indicates that the Gachsaran Formation is relatively rich in limestone in the area. However, altered samples collected on oil seeping points contain higher concentrations of calcite.

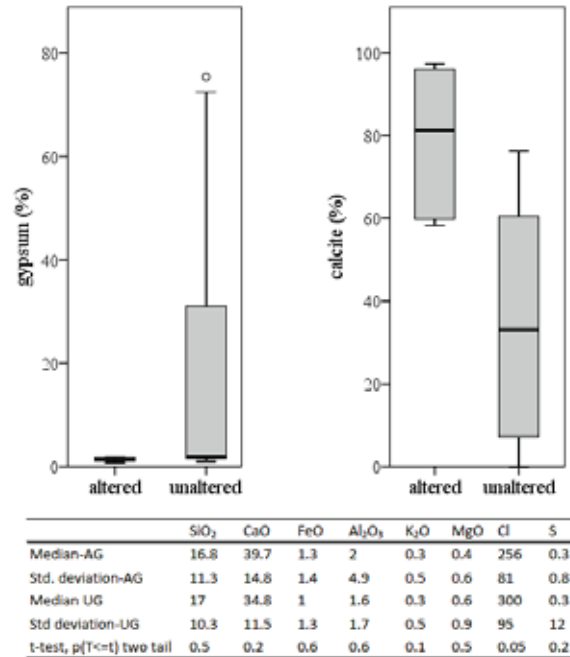


**Figure 4.11:** Box plots of gypsum and calcite concentrations measured by wet chemical analysis and statistical comparison between major oxides and elemental concentrations from altered (evaporites affected by oil seeps) and unaltered Gachsaran evaporites; UG=unaltered Gachsaran; AG=altered Gachsaran.

#### 4.3.2.2. Marly limestone formation

Figure 4.12 presents spectral signatures of unaltered rocks and oil-induced alterations within the Mishan marly limestone. Unaltered and altered samples spectra have somewhat similar reflectance spectra and all samples have diagnostic absorption features of calcite at 2.35  $\mu\text{m}$ . This means that there is spectrally little difference between the mineral composition of unaltered Mishan marly limestone and oil-induced alterations.

Oil-induced alterations cannot be predicted from spectral measurements in the Mishan marly limestones. As it was expected from spectral analysis, oil seeps do not produce a spectrally distinguishable alteration in the Mishan marly limestones. Secondary calcite is the alteration product of oil seeps, which has somewhat similar spectral characteristic with marine limestones.

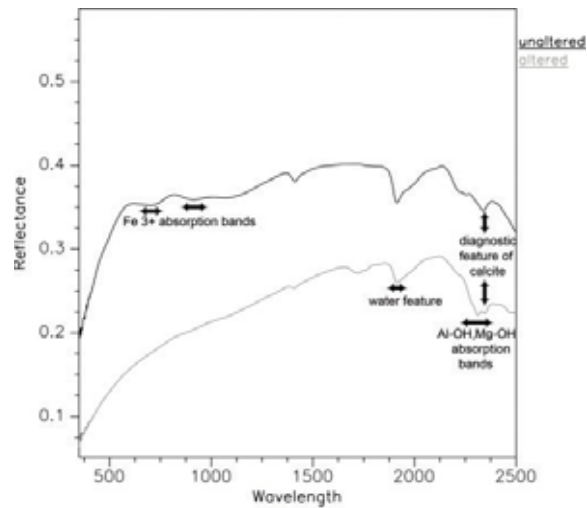


**Figure 4.12:** Characteristic reflectance spectra from oil-induced alterations in the Mishan Formation and characteristic marly limestone spectrum.

The statistical comparison (t-test) between two averages elemental concentrations from oil-induced alterations and unaltered marly limestone samples indicates that only CaO and K<sub>2</sub>O show statistically significant differences between altered and unaltered samples (Figure 4.13). The unaltered marly limestone samples have higher amounts of CaO than altered samples. All other elements do not have significantly different concentrations among altered and unaltered samples.

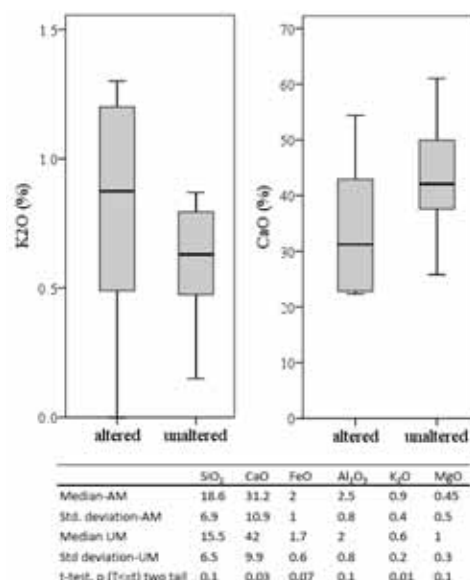


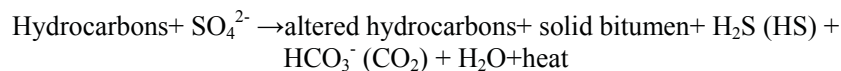
**Figure 4.13:** Box plots of CaO and K<sub>2</sub>O and statistical comparison between major oxides from unaltered marly limestone and oil seep-induced alterations of Mishan marly limestone; AM=altered Mishan; UM=unaltered Mishan.

### 4.3.3 Identifying the origin of hydrocarbon seeps by isotopic analysis

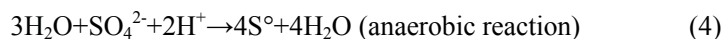
Altered evaporites show depletion in <sup>34</sup>S with respect to unaltered samples (Figure 4.14a). The δ<sup>34</sup>S values range between 14.32‰ and 21.34‰. In the Gachsaran formation, the altered samples with high amounts of sulfur are more depleted in <sup>34</sup>S. Altered samples of the Mishan marly limestone formation have the δ<sup>34</sup>S values ranging between 15.6‰ and 20‰ (Figure 4.14b). These also have somewhat similar signature for δ<sup>34</sup>S when compared with altered evaporites implying that H<sub>2</sub>S has a similar origin and that the secondary gypsum (gas alteration product) is produced through the same processes in both formations.

The presence of H<sub>2</sub>S in a petroleum basin could be related to three types of geological-geochemical processes; (a) thermal disintegration of sulfur-bearing organic matter in kerogen, (b) bacterial reduction of sulfate minerals (BSR) in gypsum bearing carbonates at temperature <60-80°, and (c) high temperature thermochemical reduction between sulfate minerals in gypsum-bearing carbonate rocks and hydrocarbons (TSR) at temperature 100-140° (Cai et al., 2003; Machel, 2001). Dissolved sulfates and reactive organic are the most important reactants involved in BSR and TSR (Machel, 2001). In the Dezful Embayment, oil fields are located between 500-4100 m depth where

temperature varies between 40-120°C (Bordenave and Hegre, 2010) implying bacterial reduction of sulfate minerals in evaporites. Bacterial sulfate reduction is faster for the lighter  $^{32}\text{S}$ - $^{16}\text{O}$  than for the  $^{34}\text{S}$ - $^{16}\text{O}$  because the energy is needed for breaking  $^{32}\text{S}$ - $^{16}\text{O}$  bond is lower than  $^{34}\text{S}$ - $^{16}\text{O}$  bond (Y. Mizutani and Rafter, 1969). Therefore, the microbial reduction of sulfates leads to an enrichment of the lighter  $^{32}\text{S}$  in the formed of hydrogen sulfide and thus a rise of isotopic values of the residual sulfide. Gas induced alterations within both formations have lower  $\delta^{34}\text{S}$  values, thus, they contain relatively more of the lighter  $^{32}\text{S}$ . The schematic net mass reaction for BSR can be represented as (Machel, 2001):



Elemental sulfur can be formed as an intermediate product of  $\text{H}_2\text{S}$  by several oxidation and reduction reactions:



The high fugacity of oxygen at the surface causes more oxidation of S to  $\text{SO}_4^{2-}$  to form sulfuric acid, which was distinct within the Gachsaran evaporite formation. Dissolved  $\text{SO}_4^{2-}$  is the reactive sulfate for bacterial derived sulfur from seawater, evaporative brines (pore water), and/or from dissolution of solid calcium sulfate (gypsum and anhydrite) (Machel, 2001).

More dissolved  $\text{SO}_4^{2-}$  is available within the Gachsaran Formation than the Mishan marly limestone Formation to react with  $\text{H}_2\text{S}$ , therefore, gas induced alteration contains higher amounts of sulfur in the Gachsaran evaporites. There is a little sulfur isotope fractionation due to oxidative processes and there is rapid sulfur isotope exchange between native sulfur and hydrogen sulfide. The sulfur isotope composition of secondary gypsum and native sulfur reflects the sulfur isotope composition of sulfide produced by the hydrocarbon-induced sulfate reduction. Using the gypsum in the unaltered Gachsaran Formation as a proxy for isotopic composition of the source of sulfate and secondary gypsum coated with native sulfur as proxy for produced hydrogen sulfide, we infer that the sulfur isotope fractionation during sulfate reduction ranged from 2‰ to 7‰ in  $\delta$  values (Figure 4.14).

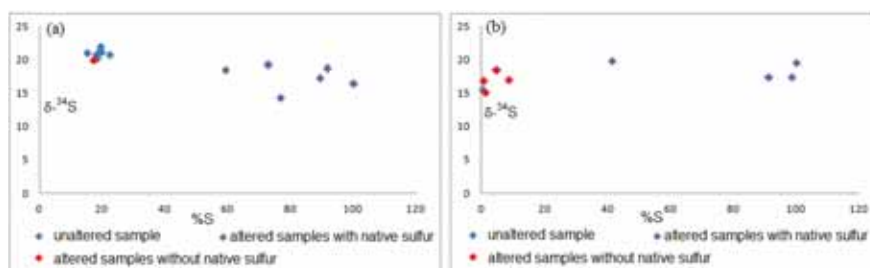


**Figure 4.14:** (a) Sulfur isotopic composition of altered and unaltered evaporites (affected by gas seep). (b) Sulfur isotopic composition of altered and unaltered marly limestones (affected by gas seep).

The results of the carbon and oxygen isotope analyses show that altered evaporites and altered marly limestone affected by oil seeps are both depleted in  $^{13}\text{C}$  and  $^{18}\text{O}$  (Figure 4.15). Measured  $\delta^{18}\text{O}$  values for all analyzed samples ranged from 0‰ to -7‰. The  $\delta^{18}\text{O}$  values are decreased in altered samples. The values of  $\delta^{13}\text{C}$  for altered rocks are different in two formations indicate that these formations were affected by two different fluids. It shows that the origins of the two oil seeps are different within the Gachsaran evaporites (NE of the Dezful Embayment) and the Mishan marly limestones (south of the Dezful Embayment). This can be supported by the isotopic composition of two oil seeps. The values of  $\delta^{13}\text{C}$  and  $\delta^{34}\text{S}$  for the oil in the Gachsaran evaporites are 24.6 ‰ and 4.14‰, respectively, and the oil taken from the Mishan marly limestone has values of -26‰ and 0.32‰ for  $\delta^{13}\text{C}$  and  $\delta^{34}\text{S}$ , respectively. The former values (for the Gachsaran oil seep) are similar to the stable isotopic compositions of the Pabdeh source rock and the later values (for the Mishan oil seep) is similar to the stable isotopic compositions of the Kazdumi source rock reported by Bordenave and Herge (2010). Thus, two types of oil seeps imprint different signatures in the isotopic composition of their induced alterations. The values of  $\delta^{13}\text{C}$  illustrated that calcite formed from petroleum oxidation in the Gachsaran formation is more depleted in  $^{13}\text{C}$  than in the Mishan formation, inferring more incorporation of oxidized hydrocarbons in secondary calcite formation.

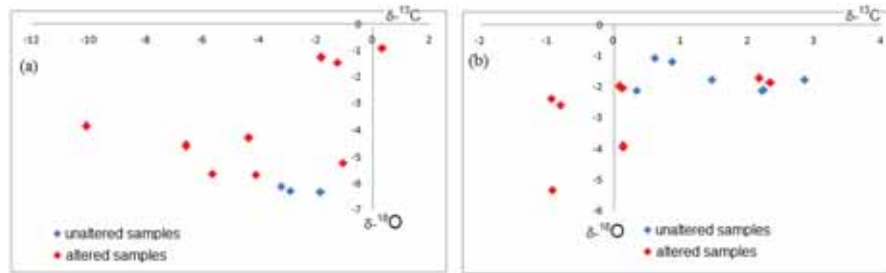


**Figure 4.15:** (a) Carbon and oxygen isotopic composition of altered and unaltered evaporites (affected by oil seep). (b) Carbon and oxygen isotopic composition of altered and unaltered marly limestones (affected by oil seep).

#### 4.4. Discussion

The minerals within alteration facies have distinctive spectral signatures, chemical compositions, and isotope ratios in the Gachsaran (cap rock) and the overlying Mishan Formation in the Zagros oil fields (Figure 4.16). The results showed that, the types of hydrocarbon seeps influence the forms of alteration that are produced within the formations.

The spectral and chemical analyses of the unaltered Gachsaran cap rock showed the heterogeneity of this cap rock located north of the Dezful Embayment (the oil seeping area). The heterogeneity of the Gachsaran evaporite seal can control the type of escaped hydrocarbons and, therefore, their migration pathways. The Gachsaran formation is relatively rich in limestone in that area, which formation was more prone to fracturing during the tectonic activities of the Zagros and this may have affected the permeability of this formation as cap rock. If hydrocarbons escaped through the cap rock reach the water table they can leak to the surface as a separate phase; as an oil phase. The spectral and chemical analyses of the Gachsaran formation located in the southern of the Dezful embayment shows that the marine evaporites and all unaltered samples are composed of gypsum and that there is no evidence of the presence of the limestone member. If escaped hydrocarbons (usually methane) react with the cap rock in that area and do not interact with ground water,  $\text{H}_2\text{S}$  as a gas byproduct of the reaction would be able to migrate to the surface (Eq. 3). The absence of iron sulfides in gas-induced alterations suggest the low concentrations of iron sulfates and absence of clays in the evaporites of that area, as clays usually provide iron into the depositional environment.

Within the Mishan marly limestone the gas-induced alterations have more easily identifiable spectral and geochemical signatures. The reaction between  $\text{H}_2\text{S}$  and calcite lead to precipitation of gypsum and native sulfur within the marly limestone formation. On the other hand, the oil seeps-induced alterations of the Mishan formation can only be recognized by geochemical signatures.

Gas seeps and their associated alterations could be vertically connected to source rocks. When the vertical migration of oil is interrupted by impermeable rocks, horizontal migration along evaporite layers is the dominant mechanism suggesting the lateral displacement of oil seeps at the surface from source rocks at the subsurface. However, gas can segregate from oil in the subsurface and move upwards vertically even when there is an efficient seal. Gas seeps affect larger and more easily identifiable areas within the both formations; while oil seeps are more localized and their associated alterations can be more detected by geochemical signatures rather than spectral signatures particularly in the Mishan formation.

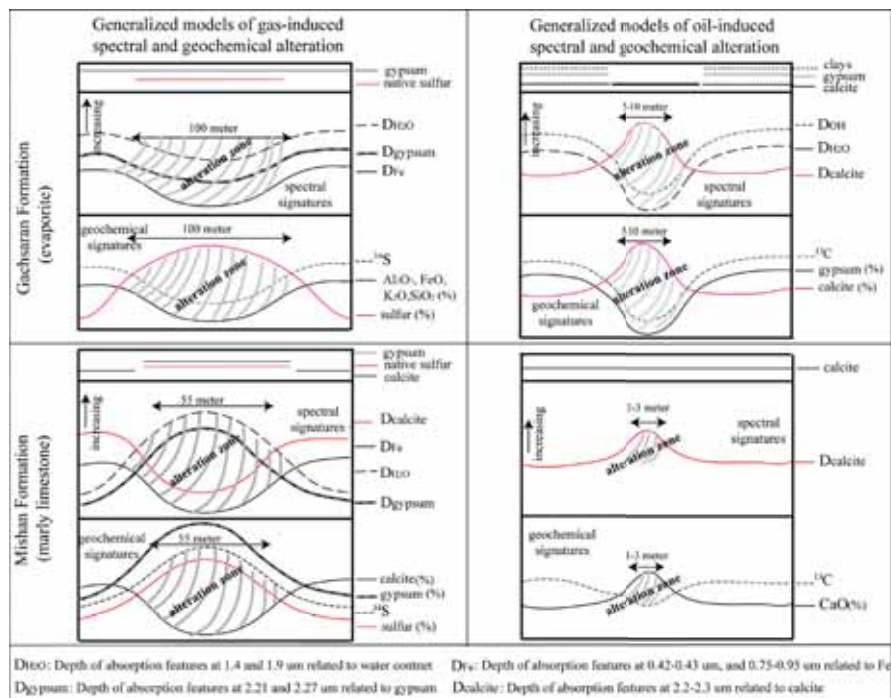


**Figure 4.16:** Generalized models of oil and gas seeps-induced spectral and geochemical alterations within the Gachsaran evaporites and the Mishan marly limestone formations.

#### 4.5. Conclusion

This study demonstrated that the combination of spectral, geochemical, and isotopic analyses provides a better understanding of surface expressions of hydrocarbons in the Zagros belt, which can be used in identifying subsurface migration pathways. Spectral analysis can be used to detect alteration changes and products, whereas chemical element and isotope analyses demonstrate causes of alterations. Gas-induced alterations cover larger areas than oil-induced alterations and the types of hydrocarbon seeps influence the kinds of produced

alterations. Gas-induced alterations are characterized by high amounts of gypsum and native sulfur, while oil-induced alterations are characterized by secondary calcite formation. The combination of field work data and laboratory analyses (spectral and geochemical) showed that there is a connection between surficial alterations and underlying petroleum reservoirs, which can be used in explorations campaigns. Our study supports the hypothesis that alterations studies would allow us to understand the oil/gas migrations mechanism in relation to the various types of seeps in the Zagros oil fields. This information carries a potential for hydrocarbon explorations.



## **5. Detecting mineralogical boundary of evaporite cap rock using rotation variant template matching<sup>4</sup>**

---

<sup>4</sup> This chapter is based on the following paper: Salati, S., van Ruitenbeek, F. J. A., van der Meer, F. D., Tangestani, M. H., and van der Werff, H., 2011. Lithological mapping and fuzzy set theory: Automated extraction of lithological boundary from ASTER imagery by template matching and spatial accuracy assessment: *International Journal of Applied Earth Observation and Geoinformation*, v. 13, no. 5, p. 753-765.

## **Abstract**

Lithological boundaries provide information useful for activities such as mineral and hydrocarbon exploration, water resource surveys, and natural hazard evaluation. Automated detection of lithological boundaries reduces bias inherent in expert interpretation of boundaries and thus improves the reliability of lithological mapping. The Rotation Variant Template Matching (RTM) algorithm was applied to ASTER imagery to detect pre-defined lithological boundaries. Templates incorporating the mineral combinations gypsum-calcite and calcite-illite were designed to detect boundaries between evaporites, marly limestone, and sandstone. The RTM algorithm successfully detected lithological boundaries by rotating the templates over the ASTER imagery. The accuracy of the detected boundaries was spatially assessed using fuzzy set theory. Boundaries from a published geological map and boundaries interpreted from a stereo pair of aerial photos by five experts were used as references for assessing the accuracy. A confidence region unifying spatial errors was defined for the geological map and stereo-pair interpretation to provide boundary zones from these references. The correspondence between detected boundaries and the boundary zones of the aerial photo was better than between detected boundaries and boundary zones of the geological map.

## 5.1. Introduction

Research on geological remote sensing has long focused on the use of spectral signatures for the detection of alteration zones (Crosta et al., 1998; Ferrier, 1996; Hubbard et al., 2003; Kruse et al., 1993; Sabine, 1999) and lithological mapping (Gomez et al., 2005; Hewson et al., 2005; Rowan and Mars, 2003; Rowan et al., 2005) without exploiting spatial information. Lithological boundaries represent the contact where changes in rock composition occurs (Neuendorf et al., 2005) and as such provide information useful for activities such as mineral and hydrocarbon exploration/exploitation, water resource surveys, and natural hazard evaluation. In the case of pixel-based methods, lithological boundaries are portrayed after classifying imagery into meaningful classes of rock. As a result, the identification of boundaries is often subjective, with distinct variations occurring between expert analyses.

In addition, classification techniques in lithological mapping have been less successful because lithological units are rarely homogeneous and intra-class spectral variations may produce noisy images. Incorporation of spatial information from neighboring pixels improves spectral classification (Lu and Weng, 2007). Spatial (i.e. contextual) information is a valuable source for inferring geological transitions (van der Meer, 2003). Integration of spatial information with spectral data is required in applications involving detection processing and highly accurate mapping (Plaza et al., 2009).

To date, little has been done to integrate spatial context with spectral data in order to improve classification results in geological mapping. By making use of variations in radiance between adjacent pixels, Penn et al. (1993) applied trained neural networks to locate boundaries and linear features. Lithological contacts between units could not, however, be detected because of insufficient contrast between pixels. Gong (1996) used knowledge-based techniques to integrate spatial data from multiple sources with spectral data for geological mapping, but the method generated much noise within boundary zones. Lucieer et al. (2004) applied multivariate texture-based segmentation methods to ASTER data to identify geological units. Segmentation results were better in areas with homogeneous textures, although the method produced some uncorrected small objects and increased uncertainty about the exact position of boundary zones between lithological units. All the attempts at integrating spatial and spectral data could not successfully localize lithological boundaries.

Automated detection of lithological boundaries reduces bias inherent in decision-making by expert interpreters, as well as improving reliability in lithological mapping. If a boundary detection technique were able to exploit expert knowledge about the spectral characteristics and spatial (contextual) information of a boundary zone, then it would provide for consistent lithological boundary mapping. Furthermore, assessment of the spatial quality

of detected lithological boundaries against existing reference sources would provide valuable information about the spatial correspondence between the detected boundaries and those sources, which is important for applications such as geological mapping.

The Rotation variant template matching (RTM) algorithm is a contextual method designed for supervised detection of boundaries (van der Werff et al., 2007). A boundary zone is not a homogeneous polygon and contains a group of pixels that according to expert knowledge belong together. The algorithm, which obtains spatial information by rotating a pre-defined template on an image, detects boundaries by matching the template against an image; the template design is based on the spectral and spatial characteristics of boundary zones between two distinct lithological units. Van der Werff et al. (2007) and Van Ruitenbeek et al. (2008) have detected boundaries between alteration zones in hydrothermal systems by applying the RTM algorithm to HyMap imagery.

The RTM algorithm has, however, not yet been used to detect boundaries from lower spectral and spatial resolution imageries, such those from ASTER (Advanced Spaceborne Thermal Emission and Reflection Radiometer). ASTER data have provided geologists with complementary data for lithological mapping (Rowan and Mars, 2003) and these data have been successfully used for mineral mapping and exploration surveying (Hubbard et al., 2003; Khan and Mahmood, 2008; Mars and Rowan, 2010; Rowan and Mars, 2003; Rowan et al., 2005; Tangestani et al., 2008).

Moreover, potentially, ASTER data are able to compensate for the limitations of site-specific applications of airborne hyperspectral data and the limited mineral mapping capacity of Landsat TM data. Detection of lithological boundaries from ASTER imagery by applying the RTM algorithm would, moreover, be a promising tool for geologic mapping, as ASTER data are available at low cost for most areas in the world.

Assessment of spatial accuracy of detected boundaries against boundaries described in existing reference sources would provide an indication of spatial correspondences between detected boundaries and those sources. Fuzzy set theory has been used to assess accuracy in a wide variety of applications (Foody, 2002; Guo and Tanaka, 2001; Hagen, 2003; Metternicht, 2003; Woodcock and Gopal, 2000). Zadeh (1965) introduced fuzzy set theory for describing imprecision in human reasoning. The theory has also been applied in research on land sustainability and in pattern recognition for making thematic maps (Altman, 1994; Foody, 1999; Woodcock and Gopal, 2000). We expect that fuzzy set theory will also be able to provide appropriate information on the spatial quality of detected lithological boundaries.

This paper represents a concerted effort to automate lithological boundary extraction procedure based on expert knowledge and to provide an indication of spatial accuracy of those boundaries to produce reliable lithological maps for geological applications.

## **5.2. Test area**

The area of interest (Figure 5.1a) is located on the western flank of the Gachsaran oil field, in the Dezful embayment, south of the Zagros front fault, in SW Iran. The Dezful embayment is the most important area for exploration of hydrocarbon reservoirs in Iran. In this region, Miocene evaporites of the Gachsaran Formation form a good seal for the hydrocarbon reservoirs. Subsidence at the foot of the uplifting mountain front fault has resulted in deposition of thick post-Oligocene sediments in the Dezful embayment (Falcon, 1974).

Major geological features in the area are the Fars group formations and the NW-SE trending Garangan anticline (Figure 5.1b). Miocene to Pliocene Fars group has been deposited in a favorable condition of progressive post-Oligocene regression in the Zagros basin. This includes

Gachsaran (GS) (cap rock of hydrocarbon reservoirs in Zagros), Mishan (MN), and Aghajari (AJ) Formations (Bahroudi and Koyi, 2004). The Gachsaran Formation predominantly consists of evaporites, with additional marl and thin limestone (Gill and Ala, 1972); the Gachsaran Formation underlies Mishan marl and marly limestone. Carbonates can be found at the contact zone of the Mishan Formation with the Gachsaran and Aghajari Formations (Motiei, 1993). Miocene to Pliocene Aghajari sandstone overlies the Mishan Formation (Alshahran and Nairn, 1997). The Aghajari Formation, which is the most extensive lithological unit in the study area, consists predominantly of sandstone, which is widely exposed in the center, west, and southwest of the area (Figure 5.1b). The Lahbari (LBM) member of the Aghajari Formation consists of calcareous argillite, siltstone, and cross-bedded limestone-sandstone, conglomerate beds interspersed with layered gypsum lenses (Alavi, 2004).

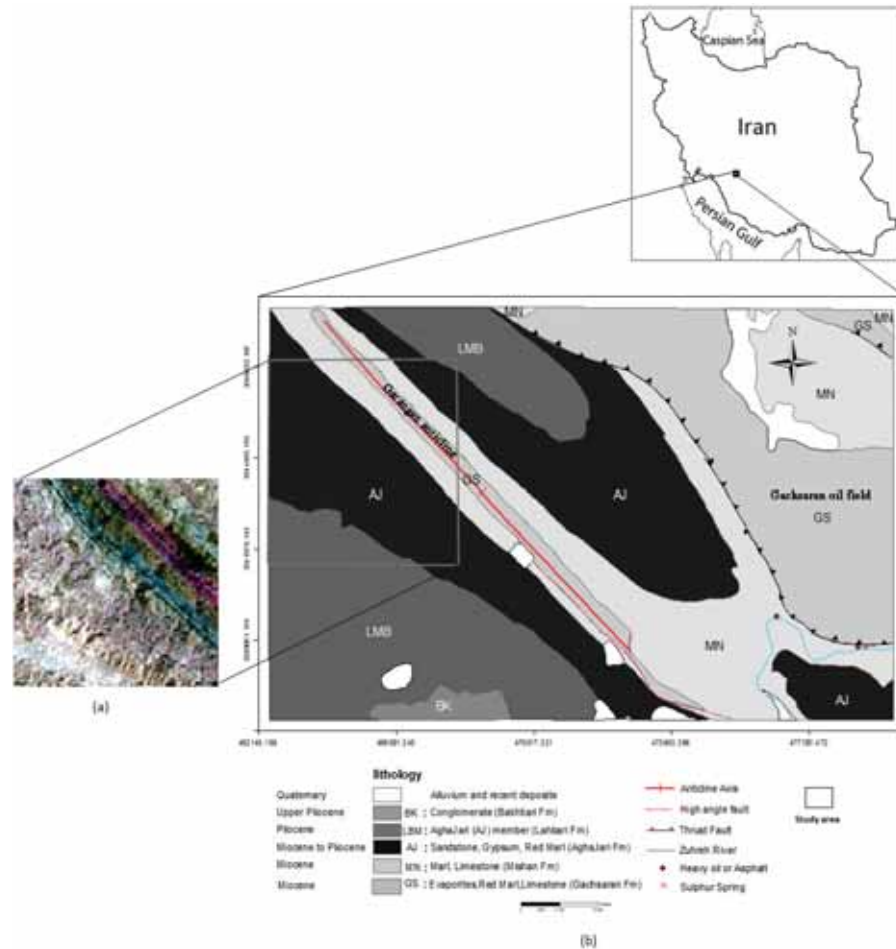


**Figure 5.1:** (a) An ASTER (RGB: 468) false color composite image of the study area. (b) Geological map of study area derived from the geological map (scale 1:100,000) of the Gachsaran (Setudenhnia and OB Perry, 1966).

### 5.3. Methods

#### 5.3.1. RTM algorithm

Template matching is a pattern recognition technique that has been used for machine vision (Tsai and Yang, 2005). Van der Werff et al. (2007) developed a rotation-variant version of the algorithm to detect boundaries between two spectrally and textually contrasting regions. The algorithm fits a template that includes the spectral information and spatial context of two spectrally and spatially contrasting areas to an image (Figure 5.2). The template moves over

the image and rotates at every position at user-defined increments. The algorithm is restricted to odd templates dimensions and has a center pixel, which stores the algorithm information for each position in output imagery (van Ruitenbeek et al., 2008).

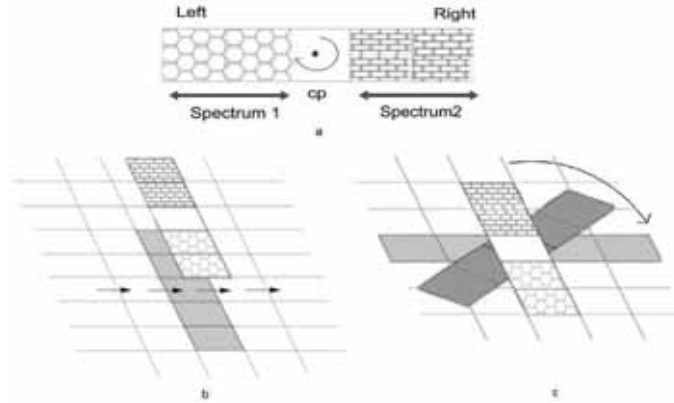


**Figure 5.2:** (a) Template design of 5×1 pixels including center pixel (cp); (b) moving over an image; and (c) rotating at every position adopted from Van der Werff et al. (2007).

The output of the RTM algorithm is a series of new images, the main ones being optimal fit ( $F_{opt}$ ) (Eq. 1), spectral variance ( $\bar{V}_s$ ) (Eq. 3), and rotation variance ( $V_r$ ) (Eq. 4) (van der Werff et al., 2007). The spectral angle mapper (SAM) method (Kruse et al., 1993) was applied to calculate the spectral fit between pixels of the template and corresponding pixels at each position on the image. Accordingly, optimal fit is expressed by a vector angle, in which low values represent the better fit. Mean spectral fit ( $F_s$ ) for all template pixels is calculated as:

$$F_s = \frac{\sum_{p=0}^N F_{(p)}}{N} \quad (1)$$

where,  $N$  is the number of template pixels (e.g.,  $N=4$  in Fig.2) and  $F_{(p)}$  is the spectral fit for a pixel  $p$ . Minimum and maximum values of  $F_s$  are found at each position by rotating the template.

The mean spectral variance ( $\bar{V}_s$ ) includes information on the spectral fit of the template.  $V_s$  can be calculated for every position as:

$$V_s = \frac{\sum_{p=0}^N (F_p - F_{s(a)})^2}{N} \quad (2)$$

The spectral fit obtained from (1) and the spectral variance calculated by (2) can be expressed as  $\bar{V}_s$  (3):

$$\bar{V}_s = \frac{\sum_{a=0}^A V_{s(a)}}{A} \quad (3)$$

where,  $A$  is the number of template orientations. The value of  $\bar{V}_s$  (mean template variance) can be used to recognize pure pixels in which relatively high values represent pure pixels (van der Werff et al., 2007). Rotation variance ( $V_r$ ) contains spatial information indicating the presence or absence of boundaries. The values of  $V_r$  are high in the presence of at least one end-member, which forms a boundary. Rotation variance values will be low when no end-members are present or both are present as a mixture. Rotation variance is calculated as:

$$V_r = \frac{\sum_{a=0}^A (F_{s(a)} - F_r)^2}{A} \quad (4)$$

where,  $F_r$  is mean fit of all orientations and is calculated as:

$$F_r = \frac{\sum_{a=0}^A F_{s(a)}}{A} \quad (5)$$

### **5.3.2. Aster data analysis**

A subset of ASTER level 1B data covering the Fars group formations and the NW-SE trending Garangan anticline was selected for image analyses. ASTER data recorded on June 4, 2007, was corrected for atmospheric effects on surface reflectance using the Log Residuals Method (Green and Craig, 1985). As the SWIR bands are main sources for information on the molecular absorption of carbonates, hydrates, and hydroxide minerals, the SWIR region was used for image analysis. ASTER data processing was done in two steps: (1) analyze spectral characteristics of lithological units to distinguish minerals in each unit; and (2) application of the RTM algorithm to the ASTER subset data.

#### **5.3.2.1. Spectral characteristics of lithological units**

An image-based stratigraphic column displays the distribution of minerals in lithological units identified on images. A false color composite of relative absorption-band depth (RBD) (Crowley et al., 1989) and a ratio image were used to create an image-based stratigraphic column. RBD images are a three-point ratio formulation for highlighting CO<sub>3</sub>, Al-O-H, and Mg-O-H absorption intensities prior to spectral analysis (Rowan and Mars, 2003). Two RBD images were calculated from the ASTER subset by using prior knowledge about the lithology of the study area.

Band 7+band9/band8 and band5+band7/band6 RBD images were applied to enhance Ca-CO<sub>3</sub>, and Al-O-H and Mg-O-H absorption intensities. The band4/band9+band6 ratio image was designed to enhance the spectral contrast of gypsum absorption features.

### 5.3.2.2. Application of RTM algorithm on the ASTER image

Lithological mapping is based on the determination of the relationship between spectral reflectance and the mineral composition of rock units (Rowan and Mars, 2003). If groups of minerals are known to occur in particular lithological units, these could be used as index minerals for estimating locations of boundaries between different units.

Regions of interest (ROIs) were used to extract mean spectra from groups of pixels of several lithological units. The mineralogy of mean spectra was interpreted by comparing spectral features at different wavelengths with re-sampled library spectra and by using prior knowledge about the lithology of the study area. Gypsum is the dominant mineral in the Gachsaran Formation, while carbonates can be found predominantly in the Mishan Formation (Motiei, 1993). Boundary zones between the Aghajari and Mishan Formations contain predominantly illite.

Figure 5.3a shows the locations of ROIs generated to extract the mean spectra of endmembers calcite, gypsum, and illite, respectively. Mean spectra were then used as endmembers for the RTM analysis. Accordingly, two 5×1 templates (Figure 5.2) with mineral combinations of gypsum-calcite and calcite-illite were designed to detect boundaries between evaporites, marly limestone, and sandstone of respectively the Gachsaran, Mishan, and Aghajari Formations.

### 5.3.3. Assessment of the spatial accuracy of detected boundaries

The accuracy of the detected lithological boundaries was assessed spatially against two reference sources; a published geological map, which is produced by Iranian oil operation companies (scale: 1:100,000); and boundaries interpreted from a stereo pair of aerial photographs (1:50,000) by five experts. When mapping lithological units, one cannot assume the units have been identified without positional errors that arise from data acquisition and geo-processing. A confidence region was defined around the boundaries from these reference sources to establish a zone unifying potential spatial errors with the true boundary line being assumed to be within a pre-defined confidence region.

Fuzzy set theory (Zadeh, 1965) was used to assess the spatial accuracy of the detected boundaries. Fuzzy set theory can be used to combine information of different scales, producing results that allow the incorporation of uncertainty. It allows grades of membership for each object or element as a member of a set.

The membership values vary continuously from complete (=1) to incomplete (=0). In this paper, the term spatial accuracy is used to represent the degree of spatial correctness of detected boundaries. It shows the degree to which the detected boundaries agree with references, so that, for example, a membership of 0.2 reflects smaller degree of agreement than a membership of 0.7. Therefore, detected boundary pixels within the confidence region were complete objects with a grade membership 1, while all intervening values define an intermediate degree of agreement between detected boundaries and references. The spatial evaluation of detected boundaries followed four main stages:

- (a) Interpretation of lithological boundaries from aerial photos
- (b) Inference of detected boundary pixels
- (c) Definition of confidence region around reference boundaries extracted from the geological map and interpretations of the aerial photo, and
- (d) Determination of fuzzy membership function.

#### **5.3.3.1. Aerial photograph interpretations**

From their knowledge of sedimentary rock types in the study area and the basic characteristics of the lithological units (e.g. shape, pattern, and tone), five experts interpreted the lithological boundaries of the area from a stereo pair of aerial photographs with ERDAS (Earth Resource Data Analysis System) software. These experts were given the ASTER color composite image of the area as a guide.

Chapman et al. (2003) described the uncertainty of a line is as an aggregation of the uncertainties of the points that comprise the line. In our study, we assumed that the uncertainties of points along a line do not exceed the uncertainties of the line's endpoints. Hence, error ellipses, which represent the uncertainty of points (Mikhail and Gracie, 1981), were calculated for the coordinates of the endpoints. This approach yielded a data set for which a boundary zone could be defined as an area that connects error ellipses of the endpoints.

#### **5.3.3.2. Inferring boundaries pixels from RTM output**

To assess the spatial accuracy of the RTM output; a local spatial autocorrelation statistic was applied to cluster pixels of detected boundaries. Clustering of gray values is a common technique for thresholding in image processing (Huang and Wang, 1995; Kwon, 2004; Otsu, 1979; Wang and Bai, 2003; Wang et al., 2006). Wang and Bai (2003) introduced the notion of the mean grey level value of points lying on a boundary being the optimal threshold. Spatial distribution of gray levels could be an important criteria for threshold selection because different images with similar histograms can be obtained by changing the spatial distributions of gray levels (Kwon, 2004). Spatial autocorrelation is a

reliable statistical indicator for detecting separable regions in remote sensing imageries (Espindola et al., 2006). Spatial autocorrelation statistics analyse the degree of similarity between attribute values of two locales. Positive spatial autocorrelation occurs when adjacent pixels have similar values, while negative values occur with dissimilar neighboring values (Getis and Ord, 1992; Premo, 2004). Getis and Ord (1992) demonstrated the use of a statistical indicator for measuring the local spatial autocorrelation of attribute values located within a user defined distance of each target value. The Getis-Ord index ( $G_i^*$ ) measures the degree of association that results from the concentration of points and all other weighted points included within a defined distance from the original weighted points (Getis and Ord, 1992). Getis (1994) established the use of a local indicator of the spatial autocorrelation to identify the spatial dependency in remotely sensed imagery. This indicator considers the autocorrelation of digital numbers centered on a given pixel and the score of these values relating to the values of the entire image (Premo, 2004; Wulder and Boots, 1997). Positive values of  $G_i^*$  indicate a cluster of high DN values, while negative values indicate a cluster of low values.

Rotation variance imageries were processed with the Getis-Ord local spatial autocorrelation statistic to infer boundary pixels. Pixels with high values of rotation variance depict detected boundaries. Consequently, high values of rotation variance identify areas that can be interpreted as lithological boundary pixels. These pixels were clustered by Getis-ord local spatial autocorrelation statistic.

### 5.3.3.3. Defining confidence region around references boundaries

The transition from analog geological map formats to their digital equivalent and the producing of geological maps from aerial photos has raised a number of potential issues regarding spatial data handling. A confidence region can provide a zone around boundaries unifying potential spatial errors. In map production, errors are introduced by processes such as registration, map compilation, and interpretation. As sources of errors were assumed to be independent, a distance containing composite error may contain, therefore, a true boundary. The inherent map error (Eq. 8) was calculated based on the national map accuracy standards of the U.S. Geological survey (USGS), which stipulate that 90 percent of well-defined features on maps should fall within 0.5mm times the map scale on the earth's surface.

$$\text{Inherent map error} = \text{radius (0.5mm)} \times \text{map scale} \quad (6)$$

Registration errors of references were determined by the root mean square (RMS) error. The values of inherent map error and registration error were summed to add to obtained boundary zones from expert interpretations. The result is a total measure of error called confidence region.

#### **5.3.3.4. Fuzzy membership function**

The fuzziness of a location indicates imprecision of a site specification (Hagen, 2003). A fuzzy membership function ( $\mu_x$ ) was applied to assign membership grades to a series of distances (Eq. 7). We have assumed that pixels located within a defined confidence region of reference boundaries were complete objects with membership grade 1. Consequently, a membership function may be applied for the fuzzy set distances to the detected boundary pixels as:

$$\mu_d(x) = \begin{cases} 0 & , x \geq 200 \\ 1 - \left( \frac{x - \min(d)}{\max(d) - \min(d)} \right) & , 0 \leq x \leq 200 \end{cases} \quad (7)$$

The specification of  $x$  is based on the distance ( $d$ ) between detected boundary pixels and the reference boundary. The minimum distance ( $\min(d)$ ) is equal to zero in a confidence region, while the maximum distance ( $\max(d)$ ) is equal to 200m, covering all detected boundary pixels.

### **5.4. Results**

#### **5.4.1. Image analyses**

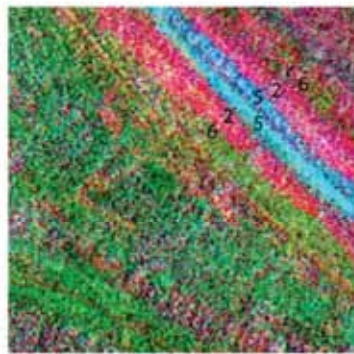
The image-based stratigraphic column (Figure 5.3b) indicating the distribution of minerals was designed based on mineral expression in a false color composite (FCC) of RBD and ratio images (Figure 5.3c). The FCC (Figure 5.3a) shows the distribution of pixels with Ca-CO<sub>3</sub> absorption (in red), Al-O-H and Mg-O-H absorption (in green), and SO<sub>4</sub> absorption (in blue). Patterns of pixels representing Ca-CO<sub>3</sub>, Al-O-H, Mg-O-H, and SO<sub>4</sub> absorption intensities corresponded well with the distribution of marly limestone, sandstone-marl, and evaporites on the geological map (Figure 5.1).

Gypsum, calcite, and illite have been used as index minerals for estimating locations of boundaries between lithological units. Calcite shows an absorption feature at 2.33  $\mu\text{m}$ , while illite exhibits a broad 2.1-2.2  $\mu\text{m}$  absorption feature at ASTER spectral resolution (Figure 5.3c). Gypsum displays absorption features at 2.2 and 2.4- $\mu\text{m}$ . Overall shapes of mean spectra of the ASTER imagery have some differences from the JPL re-sampled library due to several factors that influence image spectra shapes including mineral mixtures, grain size, and residual atmospheric absorption features.

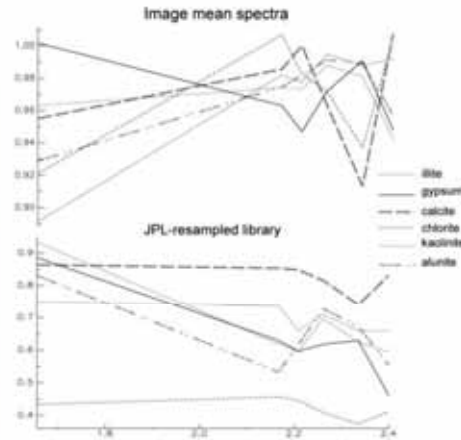
Conventional stratigraphic column				Image-based stratigraphic column False color composite expression	ASTER-derived DEM			
Period	Series	Lithology units	Typical mineral	ASTER (FCC) R: 7+9/8 G: 5+7/6 B: 4+9+6	Elevation (m)			
Tertiary	Pliocene	Fars group	Lahbari (Aghajari member)	Alunite	Miocene	Aghajari	Alunite Calcite Chlorite Kaolinite Gypsum Calcite Illite	399-679
			Mishan	Calcite		515-767		
	Sachasan		Gypsum	445-731				



(b)



(a)



(c)

**Figure 5.3:** (a) False color composite (FCC) created from RBD and band ratio images; regions 1, 2, and 3 show the locations of ROIs (polygonal ROIs with approximately 1400 pixels each) generated to extract end-members; (b) Image-based stratigraphic column, indicates distributions of minerals. (c) SWIR image mean spectra and the JPL re-sampled library.

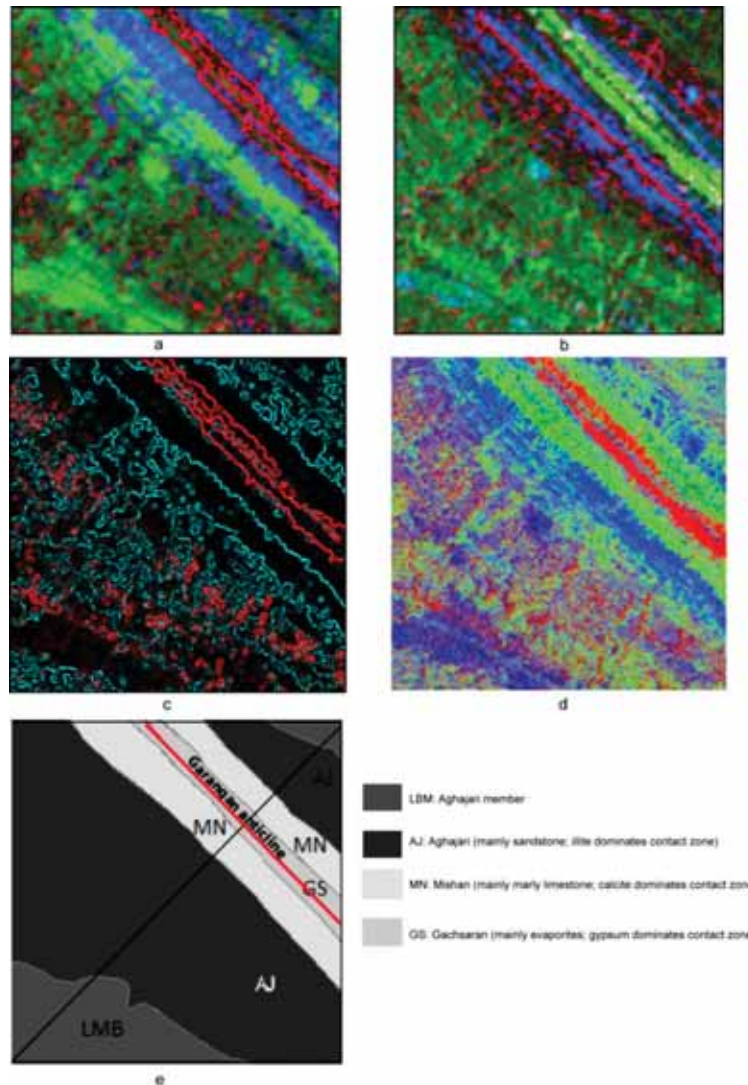
### 5.4.2. RTM algorithm

Figure 4 shows the outputs of the RTM algorithm as a series of images. Color composites of  $V_r$  (red),  $F_{opt}$  (green), and  $V_S$  (blue) were created for the templates gypsum-calcite and calcite-illite respectively (Figures 5.4a, and b). The rotation variance ( $V_r$ ) in red tones shows the NW-SE trending lithological boundaries between evaporites and marly limestone (Figure 5.4a) and between marly limestone and sandstone units (Figure 5.4b). Figure 5.4c demonstrates the color composite of rotation variance of both templates showing gypsum-calcite

boundaries (red) and calcite-illite boundaries (green). It also represents local boundaries around areas containing endmembers within the formations.

Spectral fit was calculated using the SAM method between the template pixels and respective image pixels. As a result, pixels with high  $F_{opt}$  in black tones (Figures 5.4a, and b) represent the better fit (smaller spectral angle), while pixels in green tones indicate a lower fit (wider vector angle). Blue tones display mean spectral variance (VS) that high values depict presence of only one mineral. The blue tone in Fig. 4a indicates the presence of gypsum within the Gachsaran Formation and calcite within the Mishan Formation, while the blue tone in Fig. 4b shows illite within the Aghajari Formation. The RTM algorithm results are in agreement with the inverted color composite of rule images obtained by the SAM method (Figure 5.4d). The distinction between the Aghajari Formation and its associated member (Lahbari) is difficult to see, due to their similar spectral characteristics.

Profiles of optimal fit, template rotation variance, mean spectral variance, and spectral angle mapper (Figure 5.5) were extracted following the NE-SW trending profile line shown in Fig. 4e; they assist the interpretation of the RTM algorithm results. In addition, a cross section was generated from the geological map, and rescaled to the extracted profiles of the RTM outputs to display the relation between the extracted peaks of the profiles and the respective map units. The rotation variance profiles indicate four peaks for the designed templates, representing the locations of the detected boundaries. These peaks are explicitly in agreement with the profiles of SAM displaying lower values for the better fit. Additionally, the profiles of  $F_{opt}$  display lower values (better fit) at locations of lithological boundaries peaks. Points 1 and 2 exhibit detected boundaries between calcite and gypsum within Gachsaran Formation. The rotation variance profile represents several peaks (points 3 to 11) that show boundaries around small areas within the Aghajari formation. Points 3, 4, 5, 7, and 11 show the boundaries between calcite and illite while points 6, 8, 9, and 10 show the boundaries between gypsum and calcite. However, illite is the dominant mineral in the contact zones between the Aghajari with Mishan Formations. As a result, the illite-calcite template successfully located the boundaries between these formations.



**Figure 5.4:** (a) and (b) Color composite images produced from RTM outputs; rotation variance (red), optimal template fit (green), and mean spectral variance (blue). (a) Detected boundary between evaporites and marly limestone units (in red lines) by using gypsum-calcite template. (b) Detected boundary between marly limestone and sandstone units (in red lines) by using the calcite-illite template. (c) Rotation variance of both templates showing the gypsum-calcite boundary (red) and calcite-illite boundary (green). (d) Inverted color composite of gray-level images indicating abundances of the respective minerals, showing the gypsum in red, calcite in green and illite in blue. (e) The Geological map of the study area (the black line indicates the profile line for the geological cross section and profiles of the RTM outputs shown in Figure 5.6).

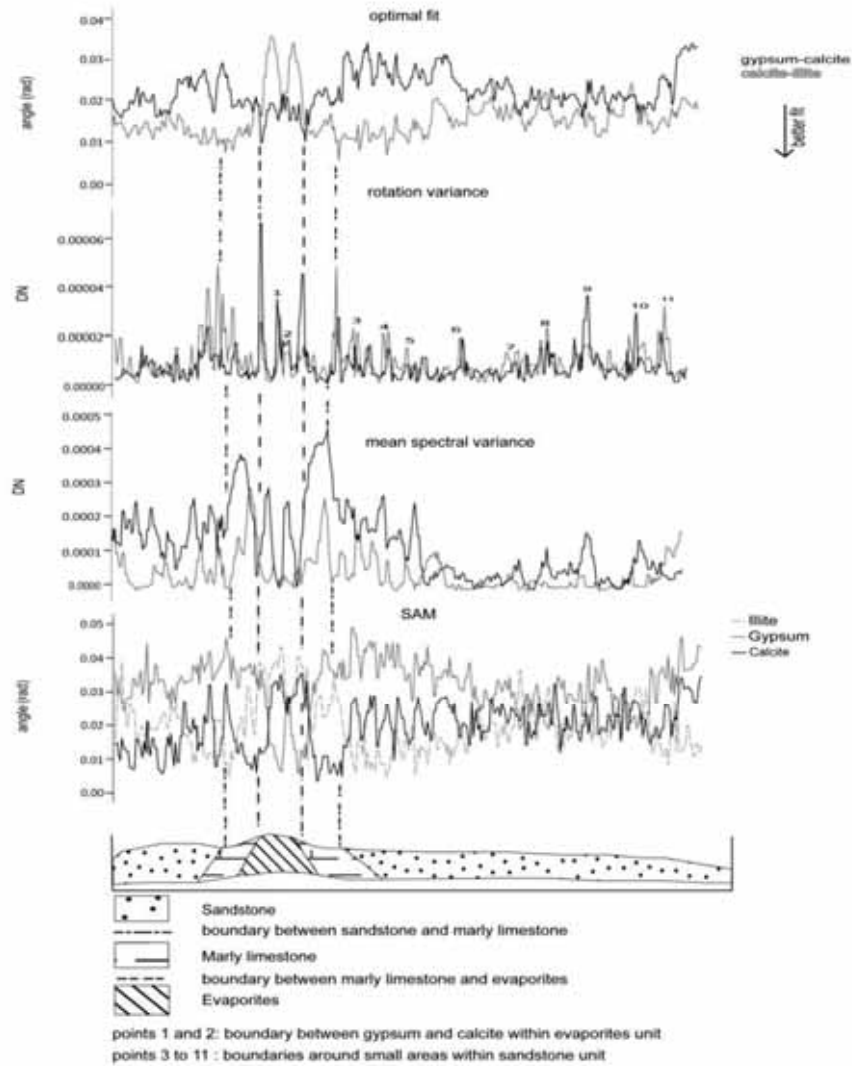


**Figure 5.5:** Profiles of outputs of the RTM algorithm. From top to bottom:  $F_{opt}$ , rotation variance, mean spectral variance, SAM results for target minerals, and schematic surface cross-section of the geological map (along the NE-SW line in figure 5.4 e).

### **5.4.3. Assessment of the spatial accuracy of detected boundaries**

Assessment of the spatial accuracy provides appropriate information for determining correspondences between the detected boundaries and those found on reference sources. The spatial accuracy of detected lithological boundaries was assessed using two sources of references; the published geological map (scale: 1:100,000), and boundaries determined by interpretation of aerial photographs (1:50,000). Subsections (4.3.1 to 4.3.3) describe the results of the assessment.

#### **5.4.3.1. Confidence region**

Confidence region was determined by summing the values of inherent map error and registration error and adding them to the obtained distances of line uncertainty. To determine line uncertainty in the aerial photographs, five experts with geological backgrounds interpreted lithological boundaries from a stereo photo pair of the study area (Figure 5.6). Boundary zones were defined as the area connecting the error ellipses of endpoints of the interpreted boundaries.

The aerial photo scale used for this study was 1:50,000, which produced an inherent map error of 25m. The RMS error value was 3m for the aerial photo registration. The sum of these values was added to the boundary zone obtained by measuring line uncertainty to obtain the confidence region around interpreted boundaries. Similarly, the geological map of scale 1:100,000 produces an inherent map error distance of 50m. The sum of the inherent map error and registration error (2.5m) provided the confidence region for the boundaries of the geological map.

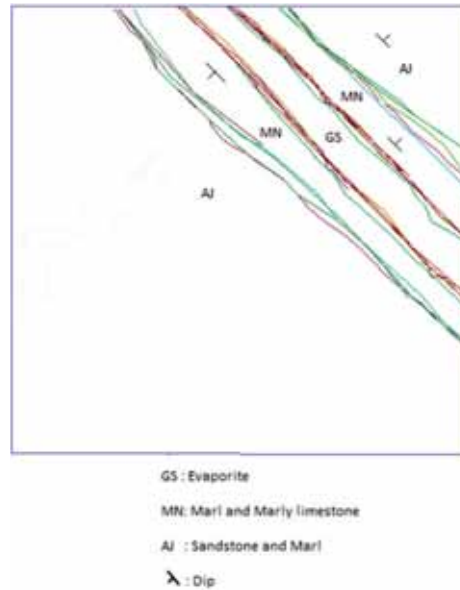


**Figure 5.6:** Lithological boundaries interpreted by five experts.

#### **5.4.3.2. Inferring boundary pixels**

The rotation variance images were processed by the Getis-Ord local spatial autocorrelation method (Figures 5.7a, and b) to cluster boundary pixels. Positive spatial autocorrelation occurs when nearby locations have high DN values. Boundary regions, including the clustered pixels with positive  $G_i$  were extracted from the image (Figures 5.7c, and d). The boundary region of Gachsaran-Mishan Formations contained 1971 pixels at the eastern end of the anticline and 2765 pixels at the western end. Each of the eastern and western boundary regions of Aghajari-Mishan Formations contained 3307 pixels.

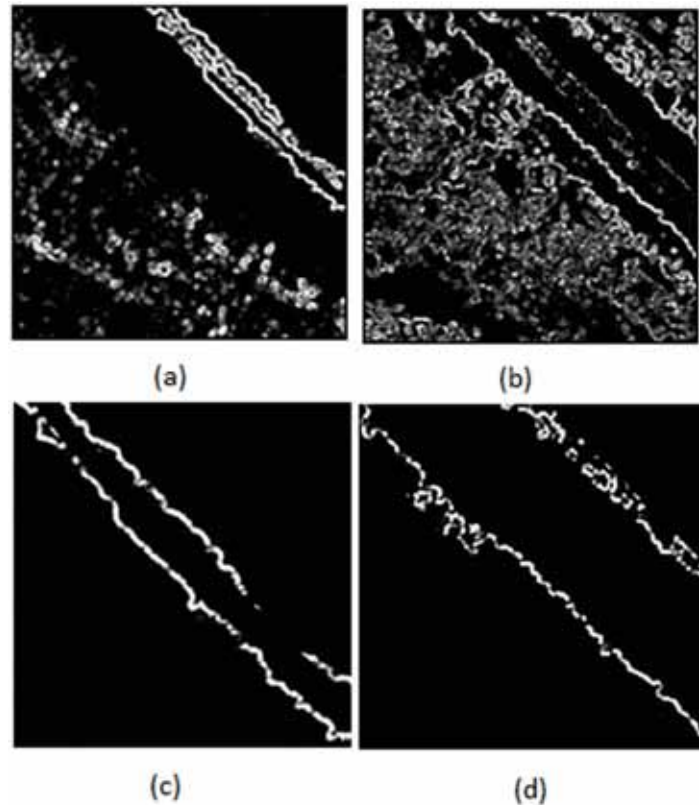


**Figure 5.7:** Rotation variance ( $v_r$ ) images for the template gypsum-calcite. (a) and calcite-illite. (b) as processed by Getis-Ord local spatial autocorrelation. (c) Extracted boundary pixels detected between evaporites and marly-limestone. (d) Extracted detected boundary pixels between marly-limestone and sandstone.

#### 5.4.3.3. Fuzzy membership function

The fuzzy membership function (Eq. 9) was applied to the confidence region of boundaries in reference sources to assign membership grades to a series of distances. The fuzzy set for the reference boundaries was combined with the detected boundary pixels (Figures 5.8a, and b, and Figures 5.9a, and b); black tones represent the confidence region of the reference sources. A comparison of boundaries verified that detected boundaries corresponded more closely with the boundaries obtained by aerial photo interpretation than those of the geological map.

Figure 5.8c presents the fuzzy membership scores of detected boundary pixels between Mishan and Aghajari Formations at every location on the reference sources. The confidence region of the geological map at the eastern end of the

anticline accounted for 37% of the 3307 RTM boundary pixels, while the confidence region of the boundary of aerial photo accounted for 58% of the RTM boundary pixels. At the western end of the anticline, the confidence region of the geological map accounted for 21% of the 3307 detected pixels, while 39% of the pixels were within the confidence region of the aerial-photo boundary map (Figure 5.8c).

Figures 5.9a and b show the comparison of the detected boundaries with confidence region for the references sources for the Gachsaran and Mishan Formations. The confidence region of the aerial photomap included more detected pixels than the confidence region of the geological map. At the eastern end of the anticline, 62% of the 1971 detected pixels showed the same boundary location as the boundary zone on the aerial photomap (Figure 5.9c). At the western end of the anticline, 47% of the 2765 detected boundary pixels had the same location as the boundary zone of the aerial photomap (Figure 5.9c). The boundary zones of the geological map included 6% of the detected pixels at the eastern end of the anticline and only 0.5% of the detected pixels at the western end (Figure 5.9c). There is, therefore, a significant difference between detected boundaries and the boundary zones of the geological map.

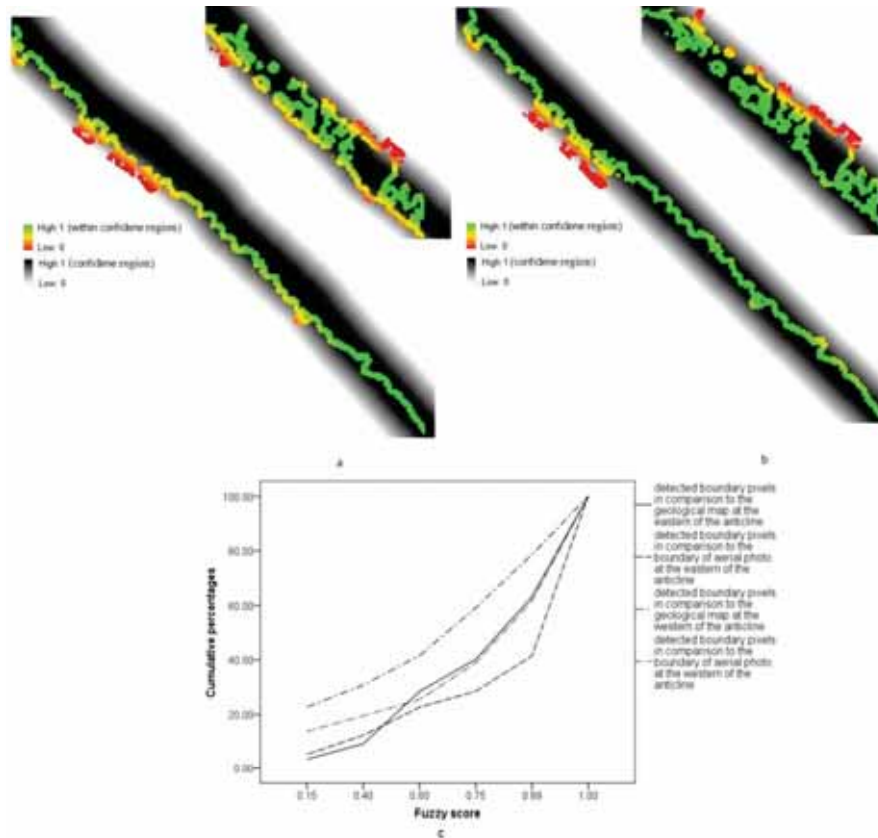


**Figure 5.8:** (a) Fuzzy assessment of spatial accuracy of the detected boundary between the Mishan and Aghajari Formations and the geological map. (b) Fuzzy assessment of spatial accuracy of the detected boundary between the Mishan and Aghajari Formations the map derived from aerial-photo interpretation. (c) Fuzzy membership scores assigned to the cumulative percentage of the detected pixels.

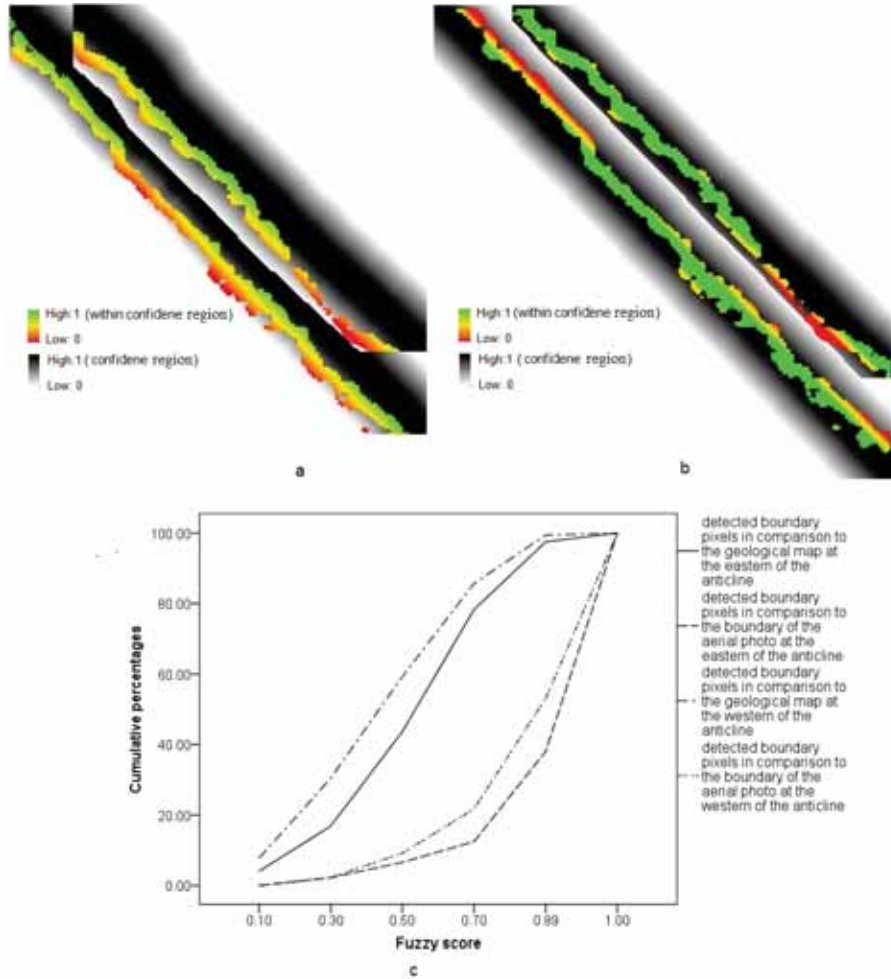


**Figure 5.9:** (a) Fuzzy comparison of detected boundary between Mishan and Gachsaran units with the geological map. (b) Fuzzy comparison of detected boundary between Mishan and Gachsaran units with the map derived from aerial photo interpretation. (c) Fuzzy membership scores assigned to the cumulative percentage of the detected pixels.

### 5.5. Discussion

The results in Figure 5.4c show that templates incorporating the mineral combinations gypsum-calcite and calcite-illite successfully detected the boundaries between evaporites, marly limestone, and sandstone. In addition, Figures 5.4a and b show that combinations of the three main outputs of the algorithm allowed identification of areas having target minerals in different units.

The detected boundaries surrounding small areas within the Aghajari Formation illustrate the lithological heterogeneities resulting from differential erosion of rock units. The RTM algorithm could not detect the boundary between the Gachsaran and Mishan Formations at the southeastern end of the anticline. Erosion may influence mineral composition of rocks at these sites; thus, the boundary could not be identified by applying gypsum-calcite template.

The results in Figure 5.4c represent inter-layers within Gachsaran and Aghajari Formations, particularly on the western flank of the Garangan anticline. The RTM algorithm may even reveal boundaries between lithological members of the same formation, e.g. the boundary detected between limestone and evaporites within the Gachsaran Formation. Such Detection of boundaries between lithological members is one of the advantages of the RTM algorithm, making it useful for producing large-scale geological maps.

The greatest advantage of the RTM algorithm over other methods of delineating lithological boundaries such as object oriented and pixel-based classification methods is that the template used is based on expert knowledge of lithological boundaries in the area under investigation. Lithological units are mainly heterogeneous, so their boundaries can only be identified by experts with local knowledge of relations between the spectral and spatial characteristics of pixels that form those boundaries.

To assess the spatial accuracy of detected boundaries a fuzzy set-based method was chosen because it can combine information of different scales, thus producing results that allow the incorporation of uncertainty. Defining a confidence region allows handling of errors of positional issues that are important for applications such as mineral and hydrocarbon explorations, water resource surveys, and natural hazard evaluation. Assessment using confidence regions provided an indication of the spatial accuracy of detected boundaries, as shown in Figure 5.8 and Figure 5.9. The main differences between the RTM results and boundaries on the geological map were due to the greater amount of details produced by the RTM algorithm.

There are always concerns about the quality of geological maps since they are obtained from a combination of field observations and expert interpretation of aerial photos. The RTM algorithm detects boundaries by distinguishing between the spectral and spatial characteristics of minerals present in the rock formations. Therefore, the detected boundaries follow changes in mineral composition between lithological units; these boundaries are not straight lines, as shown on geological maps. This is another advantage of automated detection of lithological boundaries with the RTM algorithm.

Since no ground truth data on the mineral composition of the study area were available, no quantified evaluation could be made of the quality of the RTM

algorithm outputs. Assessment of the accuracy of boundaries detected by the RTM algorithm with those of reference sources is only indicative of the spatial correspondence between RTM results and reference boundaries.

## **5.6. Conclusion**

We demonstrated that the RTM algorithm successfully detected the lithological boundaries of the study area (in the Dezful embayment) using ASTER data. It reduces bias inherent in decision-making by expert interpreters, as well as improving reliability in lithological mapping. The high level of detail about the lithological units and their associated members provided by the RTM algorithm makes it an attractive tool for producing geological maps.

Fuzzy set theory provides a useful approach for the assessment of the spatial accuracy of detected lithological boundaries. This assessment of the spatial accuracy verified that there was greater correspondence of the detected boundaries with those derived from aerial-photo interpretation than those on the geological map. The higher degree of detail in the RTM results indicates that the algorithm can be used to update existing published geological maps.

## **6. Detecting onshore gas seep-induced alteration from ASTER and WorldView-2 data<sup>5</sup>**

---

<sup>5</sup> This chapter is based on the following paper: Sanaz Salati., Frank van Ruitenbeek., Freek van der Meer, Babak Naimi., 2013. Detection of alteration induced by onshore gas seeps from ASTER and WorldView-2 data: Remote Sensing-open access journal (under review after revision)

## **Abstract**

Hydrocarbon seeps cause chemical and mineralogical changes at the surface, which can be detected by remote sensing. This paper aims at the detection of mineral alteration induced by gas seeps in a marly limestone formation, SW Iran. For this purpose, the multispectral Advance Spaceborne Thermal Emission and Reflection Radiometer (ASTER) and the high spatial resolution WorldView-2 (WV-2) data were utilized for mapping surficial rock alterations and to determine if VNIR bands of WV-2 and its high spatial resolution can improve the spatial accuracy of alteration mapping. Band rationing, principal component analysis, data fusion and the boosted regression trees (BRT) were applied to enhance and classify the altered and unaltered marly limestone formation. The alteration zones were successfully identified and mapped by remote sensing analyses. Integrating the WV-2 into the ASTER data improved the spatial accuracy of the BRT classifications. Results showed that the BRT classification of the multiple band imagery (created from ASTER and WV-2) using ROIs around field data provide the best discrimination between alterations and unaltered areas. It is suggested that WV-2 dataset can provide a potential tool along higher spectral resolution data for mapping alteration minerals related to hydrocarbon seeps in arid and semi-arid areas.

## 6.1. Introduction

Hydrocarbon seep-induced alterations have been spectrally studied by different researchers around the world, mostly in USA, Brazil, and China because of their potential values for petroleum exploration (Abrams, 2005; Khan and Jacobson, 2008; Petrovic et al., 2008; Petrovic et al., 2012; Saunders et al., 1999; Shi et al., 2012; van der Meer et al., 2002). Escaped hydrocarbons from subsurface reservoirs change the oxidation-reduction environment at the surfaces and thereby initiate diagenetic Eh/pH controlled reactions in the rocks and soils. Such changes favor the formation of mineralogical alterations such as red bed bleaching, clay formation, and formation of secondary carbonates, sulfides, and magnetic minerals (Schumacher, 1996). The interpretation of remotely sensed images cannot reveal depth, size, quality, and presence of hydrocarbon in reservoirs, but it is cost effective and could increase the probability of success in exploration (Saunders et al., 1999).

The Advanced Spaceborne Thermal Emission and Reflection Radiometer (ASTER) records solar radiation in 14 spectral bands and has provided geologists with a useful sensor in space (Etiopie and Klusman, 2010). ASTER data have been successfully used for lithological mapping (Rowan and Mars, 2003; Rowan et al., 2005) and for mineral mapping to aid in exploration (Gomez et al., 2005; Hewson et al., 2005; Hubbard et al., 2003; Khan and Mahmood, 2008; Mars and Rowan, 2010). In the VNIR and SWIR bands, iron bearing minerals, carbonates, hydrate and hydroxide minerals such as gypsum and clays display molecular absorption features related to their overtones and combination tones (Hunt, 1977). Those minerals are some of the most common alteration related minerals induced by hydrocarbon seeps (Schumacher, 1996). ASTER data have been successfully applied to mapping such alterations by Petrovic et al (2008), Lammoglia et al (1996; 2008), and Shi et al (2012). Although those alterations can be mapped with ASTER data, the spatial scale of alteration zones in some basins is smaller than the spatial resolution of ASTER data (less than 30 m of the SWIR bands). High spatial resolution imageries such as IKONOS, QuickBird, and the relatively new WorldView-2 (WV-2) provide the opportunity to map mineral variation at small scales. The WV-2 data have 8 spectral bands in the VNIR with 2 m resolution and one panchromatic band with 0.5 m resolution. This new dataset has not yet been applied for lithological and/or mineralogical mapping. With 8 bands in VNIR wavelength ranges, the WV-2 can provide us important information about transition elements, especially iron and about elemental sulfur. The use of WV-2 imagery poses a new challenge in minerals mapping because some minerals such as carbonates, hydroxides such as gypsum, and some clays do not exhibit diagnostic spectral responses in VNIR wavelength ranges. However, WV-2 data would allow us to enhance the bleaching effect of hydrocarbon seeps in sediments.

Although spectral resolution is the main support in image classification of surface materials, spatial resolution is the main factor to the provision of spatial context of target minerals identified with image classification techniques. In areas with sparse ground data, it is difficult to assess the spatial correspondence of minerals identified from imagery with field measurements because these measurements may only cover few pixels of the moderate spatial resolution imagery such as ASTER. One promising approach in image classification is integrating high spectral resolution data with high spatial resolution data to solve the challenging task of detailed mineral mapping using both datasets. Integration of ASTER and WV-2 data for mineral classification would allow us to determine if the addition of the high spatial resolution of WV-2 and its multispectral bands in VNIR will improve the classification of target minerals.

This study is an attempt to explore the potential of high spatial resolution WV-2 satellite imagery and relatively high spectral resolution ASTER in the SWIR region for identifying gas-induced alterations in the Mishan Formation in the Dezful Embayment, SW Iran (Figure 6.1). There are many locations in the Dezful Embayment where escaped hydrocarbons from the subsurface reservoirs induced alterations mostly in evaporites and marly limestones (Salati et al., 2013). The studied area is an arid area without vegetation covers and hosts several oil and gas seeps. An area of marly limestones affected by the gas seep has been chosen for this study. The alterations related to hydrocarbon in this area include formation of gypsum and elemental sulfur.

For this study, ASTER data was first used to map alteration related minerals such as gypsum and non-alteration minerals such as clay and calcite; then the potential of WV-2 imagery for highlighting the bleaching effect of the gas seep was assessed. In addition, the effect of combining the data of the two sensors on improving classification of target minerals was investigated. The prime objectives of this study are: (1) to map gas-induced alterations in marly limestones by ASTER and WV-2; and (2) exploring the potential of using high spatial resolution WV-2 imagery for enhancing alteration zones and improving the spatial accuracy of alteration mapping. The later focuses on integrating the WV-2 VNIR bands into the ASTER VNIR-SWIR bands to discriminate alteration zones from unaltered areas.

## **6.2. Hydrocarbon seep-related alterations in the Mishan marly limestone**

Onshore hydrocarbon seep-induced alterations in the Zagros belt are poorly studied. Thomas (1952) used the term Gach-e-tursh for one of the products of alterations induced by hydrocarbon seep in the Zagros. In the Persian language, Gach means chalk and tursh means sour. Thomas (1952) mentioned that the Gach-e-tursh represents an association of oxidizing petroleum seep, gypsum,

jarosite, sulphuric acid, and sulphur. By using spectral and geochemical tools, Salati et al (2012) proposed generalized models of spectral and geochemical alterations in the Dezful Embayment. In this petroleum basin, hydrocarbon seeps and their associated alterations are spatially associated with the Gachsaran cap rock and the Mishan Formation (Salati et al., 2013). In the present study, an area within the Mishan Formation (the Mamatin area) that was affected by macro (visible) gas seeps was chosen to be investigated by multispectral ASTER and WV2 remote sensing. The alteration zone covers an area of about  $55 \text{ m} \times 20 \text{ m}$  within the marly limestone formation (Figure 6.2). Within this formation, gas-induced alterations have distinctive spectral and geochemical signatures (Salati et al., 2012). The reaction between  $\text{H}_2\text{S}$  and calcite lead to precipitation of gypsum and native sulfur. The  $\text{H}_2\text{S}$  originates from bacterial reductions of sulfate minerals in the Gachsaran cap rock underlying the Mishan Formation. Gas-induced alterations were spectrally characterized by the presence of gypsum, while unaltered marly limestones showed spectra that are typical of calcite (Figure 6.2).

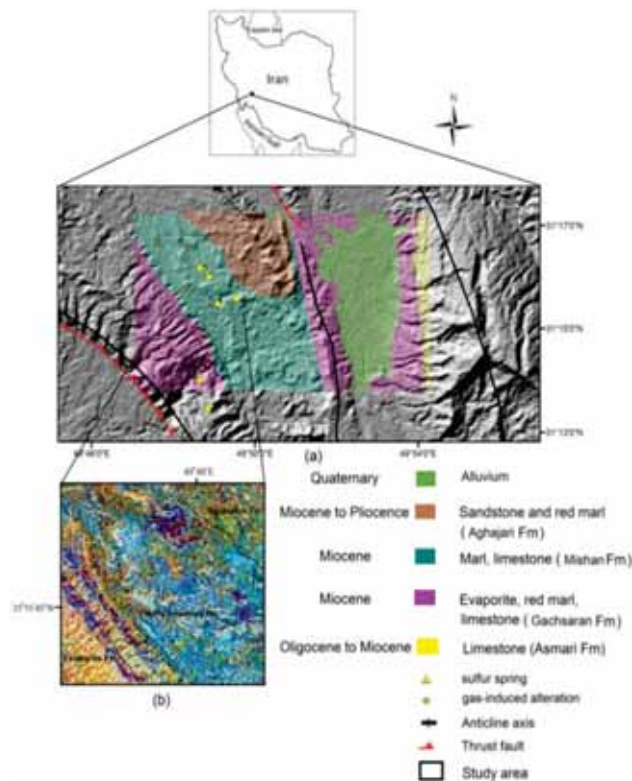


**Figure 6.1:** Study area (a) Geological map of the study area overlaid on the hill-shaded ASTER GDEM. (b) An ASTER (RGB:468) false color composite image of the study area.



### 6.3.3. Spectral measurements

Field samples were collected from the alteration zone and the surrounding unaltered rock, described in chapter 5. Spectral characteristics of altered and unaltered rock samples were measured with an Analytical Spectral Devices (ASD) FieldSpec-Full resolution spectroradiometer. Results of the field study showed that unaltered samples were spectrally characterized by (a) presence of absorption features near 2.35  $\mu\text{m}$ , diagnostic of calcite; (b) presence of absorption features near 0.4-0.45 and 0.8-0.9  $\mu\text{m}$  indicative of iron bearing minerals; and (c) presence of absorption features at 2.2  $\mu\text{m}$ , and between 2.34 and 2.44  $\mu\text{m}$  indicating the presence of Al-OH containing clays.

Altered samples were spectrally characterized by; (a) sharp decrease in the reflectance gradient between the visible red and the visible green-blue due to bleaching effects; (b) presence of absorption features at around 1, 1.4, 1.75, 1.9, 2.215, and 2.27 $\mu\text{m}$  diagnostic of gypsum; (c) absence of absorption features near 2.35  $\mu\text{m}$ , typical of calcite, which is the dominant absorption features in unaltered rocks; and (d) decrease in absorption intensities of iron bearing minerals absorption features at around 0.4-0.45 and 0.8-0.9  $\mu\text{m}$ .

## 6.4. Methods

### 6.4.1. ASTER data processing

The 30 m SWIR bands were resampled to 15 m VNIR data and the dataset was corrected for atmospheric effects on surface reflectance using the Log Residuals Method (Green and Craig, 1985). The VNIR-SWIR ASTER bands were analyzed following 3 steps. Spectral characteristics of altered and unaltered rocks were first analyzed to identify minerals from the ASTER imagery and to compare ASTER image spectra with ASD reflectance spectral. A false color composite of relative absorption-band depth (RBD) (Crowley et al., 1989) and ratio images were used to select spectral categories of gas-induced alterations and unaltered rocks. RBD images are used for highlighting  $\text{CO}_3$ , Al-O-H, Mg-O-H and  $\text{SO}_4$  absorption intensities prior to spectral analysis (Rowan and Mars, 2003). Table 6.1 shows ASTER band ratios used for enhancing mineral features in the study area.

**Table 6.1** ASTER band ratios for enhancing mineral features.

Mineral feature	ASTER band combinations
Ferric iron	2/1
Ferric oxide	4/3
Ferrous iron	1/2
Calcite	(7+9)/8
Clays	(7+5)/6
Gypsum	4/(9+6)

Source of data: ([http://www.ga.gov.au/image\\_cache/GA7833.pdf](http://www.ga.gov.au/image_cache/GA7833.pdf).)

After analyzing spectral characteristics of alteration minerals and unaltered areas, mineral mapping was applied on the ASTER imagery. With digital image classification, image pixels are assigned to classes based on similarities between spectral signatures of each image pixel and spectral signatures of end-members. Reference spectra were extracted from spectral measurements of field samples (resampled to the ASTER) and from ASTER image pixels. The known alteration zone (55 m) covers 3-4 ASTER pixels (with 30 m resolution); therefore, pure image pixels having similar spectral characteristics with pixels co-located with the known alteration zone were selected to derive end-members.

To enhance the visualization of spectral features of minerals, ASTER bands were pan-sharpened with WorldView- 2 panchromatic image using PC Spectral Pan-Sharpener. Pan sharpening can be used as a pixel-level fusion technique to increase the spatial resolution of multispectral image (MS). In pan sharpening techniques, a PAN (single band) image is used to sharpen an MS image with preserving spectral information. The PC Spectral Sharpener method (Chavez et al., 1991) was applied to sharpen VNIR-SWIR bands of the ASTER with the high spatial resolution WV-2 panchromatic image (0.5 m resolution) in order to spectrally and spatially enhance the alteration zone. In this technique, the principal component transformation is performed on multispectral ASTER data, which are then resampled to high resolution WV-2 pan data.

### 6.4.2. WorldView-2 data processing

The WV-2 Geo Tiff data was converted to WV-2 radiance in ENVI 4.8 software. The WV-2 bands were corrected for atmospheric effects on pseudo surface reflectance using the Log Residuals Method (Green and Craig, 1985). Pan-sharpened WV-2 was created by fusing the MS WV-2 imagery (with spatial resolution of 2 m) with 0.5 m pan WV-2 imagery using the method of Gram-Schmidt (GS) Spectral Sharpening. The GS spectral Sharpening technique has been successfully used for mapping land cover (Padwick et al., 2010) and urban tree species (Pu and Landry, 2012). The GS algorithm uses the spectral response function of a given sensor to estimate what the panchromatic data look like (WV-2 panchromatic). The GS pan sharpening is spectrally stronger than other sharpening techniques for fusion of multispectral bands of WV-2 with the panchromatic band (Padwick et al., 2010). The pan-sharpened imagery was used in ratioing, PCA, and classification analyses.

### 6.4.3. Data integration

The high resolution multispectral WV-2 data and the multispectral ASTER were integrated and treated as an independent multiple band imagery in order to carry out the boosted regression trees (BRT) classification. The new multiple band imagery has the same spatial resolution as the fused WV-2 (0.5 m) and contains 17 spectral bands of WV-2 (8 bands in VNIR) and of ASTER (3 bands in VNIR and 6 bands in SWIR).

### 6.4.4. Boosted regression trees classification (BRT)

Boosted regression tree (BRT) (Friedman and Meulman, 2003) is a nonparametric supervised classification (and regression) algorithm that fits complex nonlinear relationship by combining two algorithms of classification and regression tree (CART) (Breiman et al., 1984) and boosting. In the BRT technique, the CART algorithm relates the response to the predictor variables (spectral bands) by recursive binary splits, and the boosting method combines large numbers of simple tree models (generated by iteratively varying the training sample) to improve predictive performance (Elith et al., 2008). The conventional CART algorithm itself has been used successfully for classification of remote sensing images e.g. (Friedl and Brodley, 1997; Lawrence and Wright, 2001). Boosting is one of ensemble classification methods that can be applied in conjunction with supervised classification algorithms and improves classification accuracy (McIver and Friedl, 2001).

Combination of these two techniques (i.e. BRT) has been shown to be effective in improving the accuracy of satellite image classifications (Lawrence et al., 2004; McIver and Friedl, 2001). This method estimates local probabilities of

class membership for the classified map and has several advantages including: (a) it represents information in a way that is easy to visualize, (b) preparation of predictors is simple and they can be of any type (numeric, binary, categorical, etc.) with any types of distribution (normal and non-normal), (c) irrelevant predictors are seldom selected, and (d) trees are insensitive to outliers (Elith et al., 2008). This method has also been successfully applied for predictions in the other fields such as economics (Schonlau, 2005), computer sciences (Tyree et al., 2011) and ecology (Elith et al., 2008). A working guide on the BRT analysis can be found in Elith et al (Elith et al., 2008).

In this study the BRT algorithm was used to classify the ASTER, WV-2, and the multiple band imagery created from the ASTER and WV-2 datasets to detect alteration minerals related to the gas seeps. Six scenarios were defined for the BRT classifications based on three datasets and three selected groups of ROIs:

- (a) The ASTER imagery using a group of ROIs which were chosen from the purest pixels of ASTER imagery.
- (b) The WV-2 imagery using; (1) a group of ROIs selected from the purest pixels of the WV-2, and (2) a group of ROIs chosen from imagery pixels co-located with ground measurements.
- (c) The new multiple band imagery using; (1) ROIs co-located with the purest pixels of the ASTER, (2) ROIs co-located with the purest pixels of the WV-2, and (3) ROIs chosen from imagery pixels co-located with ground measurements.

The BRT classification using a group of ROIs co-located with ground measurements was not possible for the ASTER imagery because these measurements only cover few pixels of the ASTER, which cannot provide adequate samples for the classification.

The models were fitted in R version 2.15.3 (R development Core Team 2006), using generalized boosted regression models (gbm) package version 2.0-8 (Ridgeway, 2006). The learning rate and number of trees are two important parameters controlling prediction errors. The learning rate shrinks the contribution of each tree as it is added to the model. The lower learning rate and 1000 trees were used to deal with over fitting of BTR for small number of samples (Elith et al., 2008).

One of the most important outputs of the BRT algorithm is the relative influence of predictors, which is measured based on the number of times a variable is selected for splitting, weighted by the squared improvement to the

model as a result of each split and averaged over all trees (Friedman and Meulman, 2003). This output is a valuable measure to investigate the potential impact of WV-2 VNIR bands on classification of the image. The main purpose of the classification was detecting target minerals and evaluating the spatial correspondence between classified areas and field measurements; thus, an accuracy method involving the field measurements was applied to evaluate the spatial allocation of the categories. The classification accuracy performance was evaluated by Area Under Curve (AUC) of a receiver operating characteristic (ROC) plot, (hereafter AUC (Fielding and Bell, 1997)). This provides a provision of spatial correspondence between field measurements and classification results.

A ROC curve is constructed from false positive rates ( $x$  axis) and true positive rates ( $y$  axis) for all thresholds which reclassify the estimated local probability of a class into binary values (presence and absence of the class). AUC is a threshold-independent method and provides a single measure of model performance (accuracy) varying from 0 to 1. AUC score of 1 shows the best model (perfect discrimination), a score of 0.5 indicates random predictive discrimination, and a score of less than 0.5 indicates discrimination worse than chance. Based on laboratory spectral and geochemical analysis, sampling points were classified into two groups; altered and non-altered. Then the accuracy of the BRT classification in distinguishing altered areas was evaluated using AUC method.

## **6.5. Results**

### **6.5.1. ASTER data processing**

Spectral reflectance of altered and unaltered samples taken from field was resampled to the ASTER scene and spectral reflectance curves of ASTER pixels co-located with sampling points were derived and compared with laboratory data (Figure 6.3a). There are some differences between the laboratory spectra of unaltered marly limestone and image-derived spectra. The laboratory spectra of all unaltered samples displayed absorption features at around 2.3  $\mu\text{m}$  to 2.35  $\mu\text{m}$  indicative of the presence of calcite. However, reflectance spectra derived from ASTER imagery pixels co-located with field sampling points do not show any absorption features indicative of calcite but illustrate absorption features at 0.8  $\mu\text{m}$ , 2.15  $\mu\text{m}$ , and 2.2  $\mu\text{m}$  indicating the presence of iron-bearing minerals and clays. This difference, however, is because of the spatial scale of data.

Since analysis of the reflectance spectra revealed that the predominant gas seep alteration-related mineral in the marly limestone formation is gypsum, the image-derived spectra indicative of calcite, gypsum, and clay spectra were chosen for the classification (Figure 6.4). Gypsum has been used as an index

mineral to enhance gas seep-induced alterations in the marly limestone formation, while calcite and clays have been used to map unaltered marly limestone formation.

Band ratios were adapted to spectrally enhance gypsum in the marly limestone formation. Figure 5 shows the surface manifestations of hydrocarbon seeps that band ratios emphasized. The results (Figure 6.5) illustrate a consistent correlation between the gas seeping area and areas rich in ferrous iron and gypsum, lacking in carbonates and low amounts of clays. The results agree with the generalized spectral and geochemical model which was proposed by analyzing field data. To spatially enhance gas-induced alterations, the VNIR-SWIR bands of ASTER were pan-sharpened with 0.5 m panchromatic band of WV-2 (Figure 6.6) by PC spectral sharpening. The fusion of both dataset was used in order to determine if further spatial differentiation of the alteration zones were possible. The alteration zones in the marly limestone (consisting of gypsum) can be identified as dark brown in pan-sharpened ASTER VNIR (Figure 6.7a) and purple in pan-sharpened ASTER SWIR bands (Figure 6.6b).

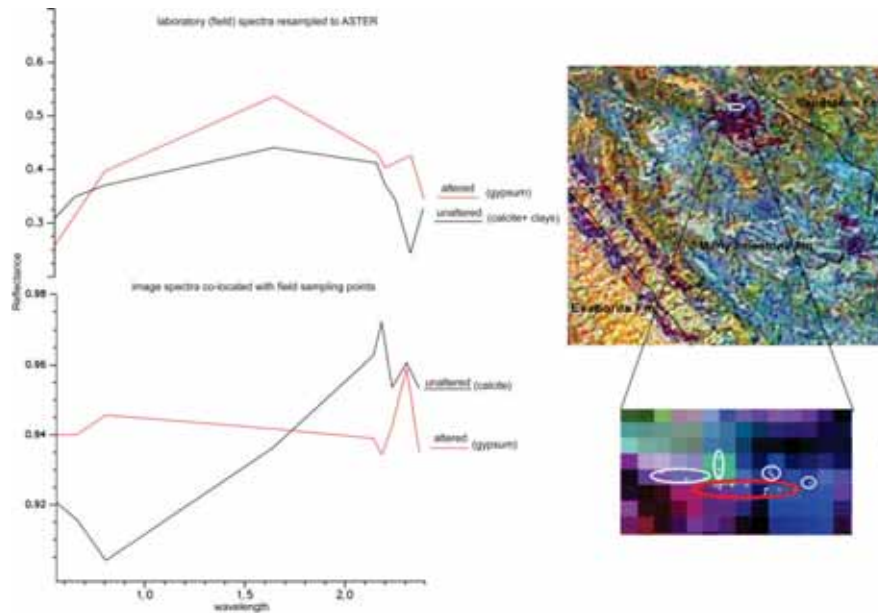


**Figure 6.3:** (a) Spectral reflectance curves for selected marly limestone and altered marly limestone from the Mishan Formation resampled to the ASTER imagery and pseudo reflectance spectra of ASTER pixels co-located with field sampling points. (b) FCC of the ASTER overlaid by lithological boundaries. Band combination used is (RGB) 4-6-8. (c) Enlargement showing location of field measurements. The red ellipse displays pixels co-located with samples which were identified as alteration with field spectral and geochemical measurements and white ellipse illustrates pixels co-located with samples which were identified as unaltered with field.

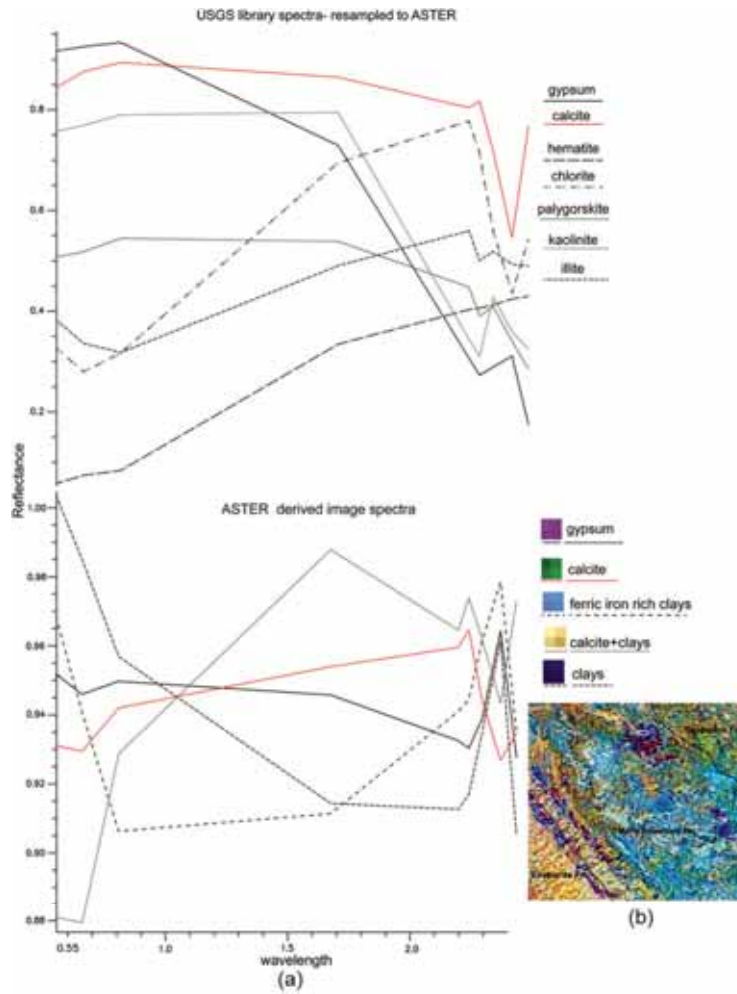


**Figure 6.4:** (a) Mean spectra derived from ASTER imagery compared to the USGS spectral library re-sampled to the ASTER. (b) FCC image created from ASTER bands (The area is located inside the black box in Fig. 6). Band combination used is (RGB) 4-6-8.

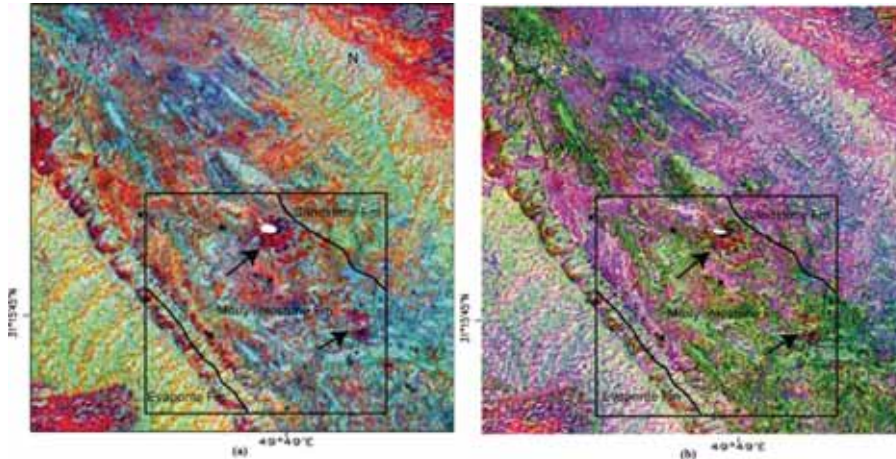


**Figure 6.5:** (a) False color composite created from RBD and band ratios:  $b4/(b6+b9)$  for enhancing gypsum (Red),  $(b7+b9)/b8$  for enhancing calcite (Green), and  $(b5+b7)/b6$  for enhancing clays (Blue). (b) False color composite created from  $b4/(b6+b9)$  for enhancing gypsum (Red),  $b4/b3$  for enhancing ferric iron (Green), and  $b3/b1$  for enhancing ferrous iron. The black arrows point to the alteration zone in the Mishan marly limestone Formation. The black box shows the extension of the ROI selected for ASTER classification and WV2 image processing and the arrows point to alterations induced by gas in the marly limestone formation. The white circles show field observations. The asterisks and plus symbols show the gas seeps indications in the geological map of the study area.

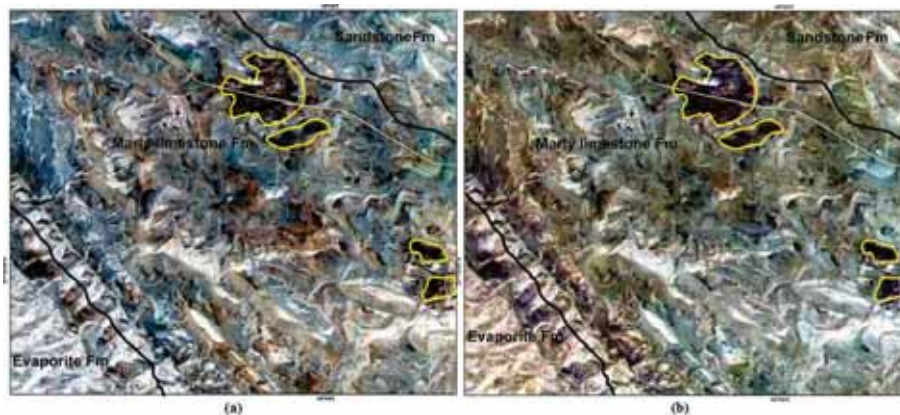


**Figure 6.6:** (a) False color composite created from pan-sharpened ASTER VNIR bands (15 m resolution) with WV2 0.5 m panchromatic image, (b) false color composite created from ASTER SWIR bands with WV2 0.5 m panchromatic image. Band combination used in (a) is (RGB) 1-2-3 and in (b) is (RGB) 4-6-8. Yellow polygons show alteration zones enhanced by fusion (the extension of this image is shown as a black box in Figure 6.5).

### 6.5.2. WorldView-2

A false color composite of WV-2 image was created for band 6 (red), band 3 (green), and band 2 (blue) and overlaid with lithological boundaries and field observation points (Figures 6.7a and b). Spectral reflectance curves of pixels collocated with sampling points were derived from WV-2 imagery (Figure 6.7c). There are subtle differences between spectra of altered zone and unaltered zone in VNIR bands of the WV-2. The reflectance spectra of altered marly limestone show subtle absorption feature in the 0.4-0.5  $\mu\text{m}$  which could be related to the presence of elemental sulfur and/or ferric iron bearing minerals (Figure 6.7c). Sulfur has diagnostic feature in the VNIR wavelength range. It shows a strong decrease in reflectance in the 0.4-0.5  $\mu\text{m}$  range towards shorter wavelengths. This results from the semiconductor behavior of sulfur that creates a strong absorption at higher level energies (Gleeson et al., 2010). The spectra of image pixels covering altered area have shallow absorption features around 0.720  $\mu\text{m}$  indicating the presence of iron bearing minerals in the Mishan formation. The prominent  $\text{Fe}^{2+}$  absorption bands occur near 0.9-1.2  $\mu\text{m}$  (Crowley et al., 2003). The presence of absorption bands near 0.9-0.95  $\mu\text{m}$  is indicative of  $\text{Fe}^{2+}$  bearing minerals in image pixels covering field data.

Based on spectral features of unaltered marly limestone and the alteration zone (Figure 6.7c), two band ratios and one RBD images were created to enhance the alteration minerals in the Mishan marly limestone. The band ratio 2/1 (0.480  $\mu\text{m}$  /0.420  $\mu\text{m}$ ) can be used to enhance native sulfur and band ratio 4/7 (0.660  $\mu\text{m}$  /0.950  $\mu\text{m}$ ) can be used to detect the distribution of ferrous iron bearing minerals. To enhance the distribution of ferric iron bearing minerals, an RBD image was created from band5 (0.660  $\mu\text{m}$ ) +band3 (0.545  $\mu\text{m}$ )/band1 (0.420  $\mu\text{m}$ ). The false color composite (FCC) of RBD and ratio images shows the distribution of pixels with absorption by native (in red), ferric iron bearing minerals (in green), and ferrous iron bearing minerals (in blue) (Figure 6.8a). The alteration zones are exposed in whitish yellow color, which shows the presence of sulfur and ferric bearing minerals. The altered areas appear in bright color in PCA results because of the high reflected radiance of bleached areas (Figure 6.8b).

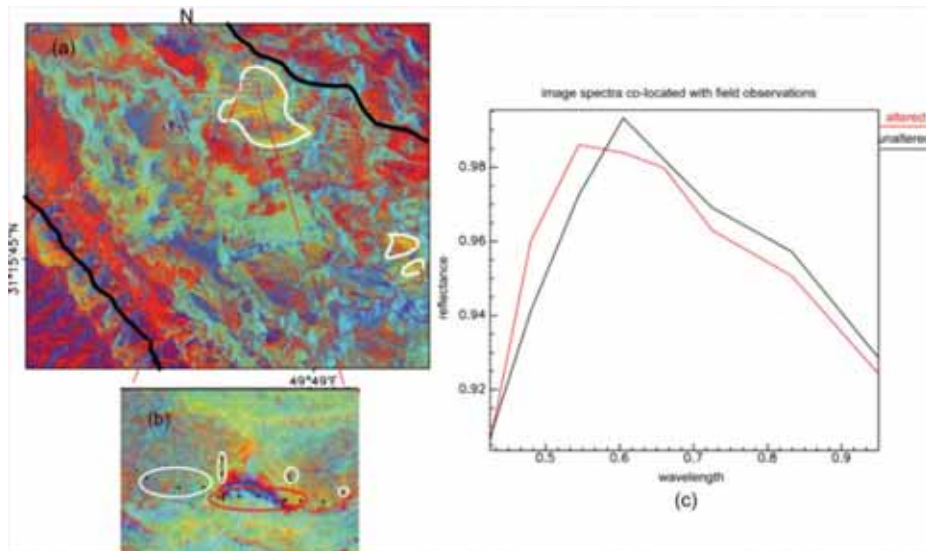


**Figure 6.7:** (a) Color composite image (R: 6, G: 3, B: 2) created from WV-2 imagery. (b) Enlargement showing location of field measurements. Black crosses indicate locations of samples, red ellipse surrounds samples which were identified as altered by field measurements, and white ellipses are around samples identified as unaltered by field measurements. (c) Mean spectra derived from image pixels covering field data.

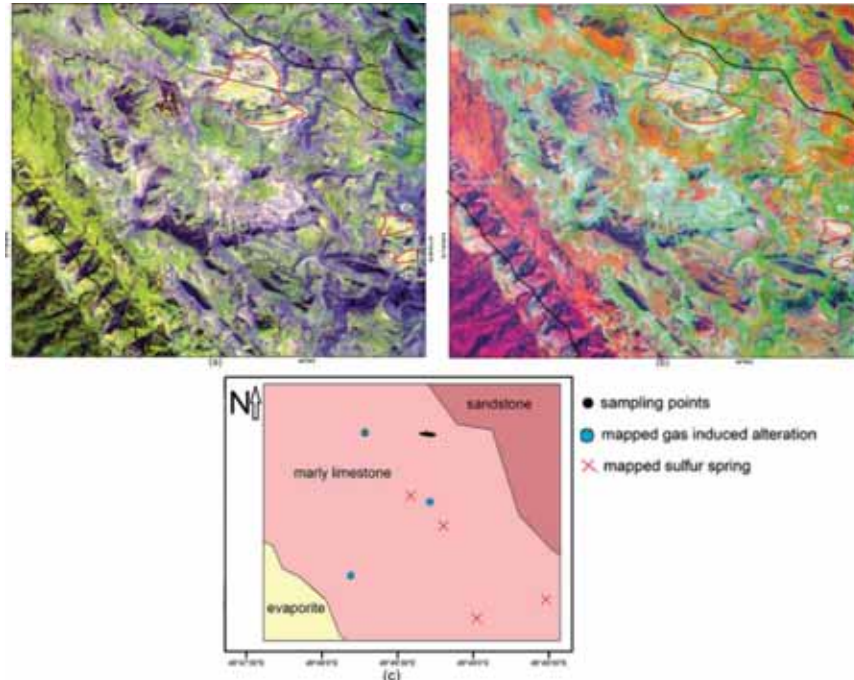


**Figure 6.8:** (a) FCC image created from band 2/band1 (in red), band5+band3/band1 (in green), and band4/band7 (in blue); (b) illustrates a FCC of PCA123 from WV2 bands. Red ellipses surround alteration zones and black lines display lithological boundaries; (c) shows the geological map of the study area.

### 6.5.3. The BRT classification

Figure 6.9 shows the classification of the ASTER data set obtained with the BRT method. The predicted power of the classification is fair; the AUC has mean values of 0.62 (Table 2- scenario 1). The results show that the BRT is able to classify altered areas using ROIs of purest pixels of the ASTER imagery indicating of gypsum (gas-induced alteration product in marly limestone in red color), calcite, clays, and iron bearing minerals. There are some misclassifications for image pixels co-located with field samples because of the different scale of field measurements and pixel size of the ASTER. Each of the field samples is only indicative of one point on the ground and do not represent the mixed nature of a pixel. ASTER SWIR bands 4 (1.6-1.7  $\mu\text{m}$ ), 8 (2.295-2.365  $\mu\text{m}$ ), 5 (2.145-2.185  $\mu\text{m}$ ), and 6 (2.185-2.225  $\mu\text{m}$ ) indicative of the presence of gypsum and calcite have the most contributions in distinguishing of the alteration zone (Table 6.2- scenario 1). The VNIR bands of ASTER showed less contribution on the classification of the altered area.

In the southwestern quadrant of the image there are some areas close to the lithological boundary between evaporite and marly limestone formations contain gypsum which transported by erosion mainly by streams from the higher elevation of the evaporite Fm toward lower elevations of the marly limestone Fm.

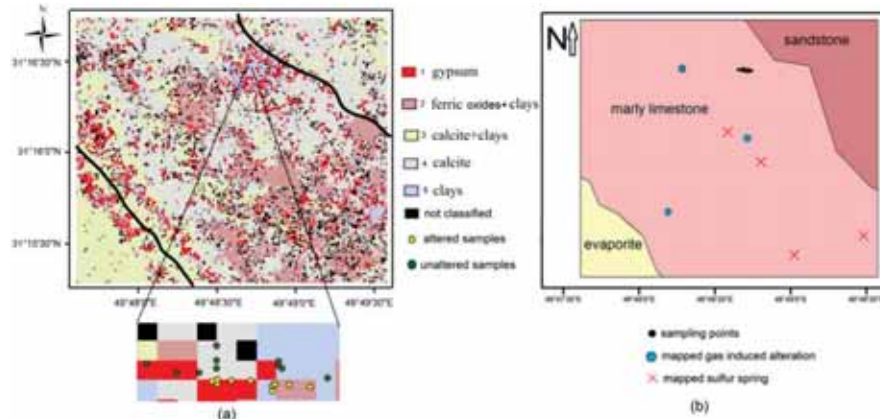


**Figure 6.9:** (a) Results obtained by the BRT classification with end-members extracted from the purest image pixels of ASTER. (b) Geological map of the study area.

Results of the BRT classification of the WV-2 using ROIs of pure pixels of the WV-2 and ROIs co-located with sampling points are shown in Figures 10a and b. It is notable that the classification is only based on spectral features of pixels in VNIR wavelengths range. The predicted power of the classification using ROIs of pure pixels is fair; the AUC has mean values of 0.68 (Table 6.2-scenario2). Bands 3 (0.54  $\mu\text{m}$ ), 5 (0.66  $\mu\text{m}$ ), 8 (0.95  $\mu\text{m}$ ), 4 (0.6  $\mu\text{m}$ ), and 1 (0.42  $\mu\text{m}$ ) have the most contributions on the classification of pixels co-located with ground truth (Table 6.2- scenario2). Bands 3, 5, and 4 indicate the presence of ferric iron bearing minerals while band 8 can be related to the presence of ferrous iron bearing minerals.

The importance of band 1 (0.42  $\mu\text{m}$ ) can be related to sharp fall of spectra at this wavelength range related to Fe-OH. Class 1 (red color) is indicative of alterations related to gas seeps, which mostly represents bleached areas. Some of the image pixels co-located with altered samples have not been classified in class 1. The reason is these pixels are co-located with areas near the gas flames covered by ash and are darker than bleached areas. Class 3 does not only indicate areas having iron bearing minerals, but it also shows roads, roofs, and asphalts and class 5 with no distinct absorption features can be related to shadow (Figure 6.10a).

Figure 6.10b shows the results of BRT classification using ROIs around sampling points. Altered (red color) and unaltered pixels linked to the ground

truth have been successfully classified based on their absorption features in VNIR of the WV-2. The predicted power of the classification using ROIs of pixels co-located with ground truth is very good; the AUC has mean values of 0.93 (Table 6.2- scenario3).

Bands 3 (0.54  $\mu\text{m}$ ), 1 (0.42  $\mu\text{m}$ ), 4 (0.6  $\mu\text{m}$ ), 2 (0.480), 8 (0.95  $\mu\text{m}$ ), and 5 (0.66  $\mu\text{m}$ ) have the most contributions on the classification of pixels co-located with ground truth (Table 6.2- scenario3). The classification was also successful in highlighting other altered areas displayed in the geological map as indications of gas seeps. Classes 1, 2, and 4 are classified as unaltered areas. Image pixels co-located with altered samples were classified as Class 3 (red color). Since spectral features of these pixels showed the presence of ferric iron bearing minerals (Figure 6.7c), class 3 represents ferric iron bearing minerals in Figure 6.10b. Bands 6 (0.725) and 7 (0.835) have the lowest contribution in distinguishing classes because most classes show very shallow absorption depth at 0.725  $\mu\text{m}$  and do not have any distinct feature at 0.835  $\mu\text{m}$ .

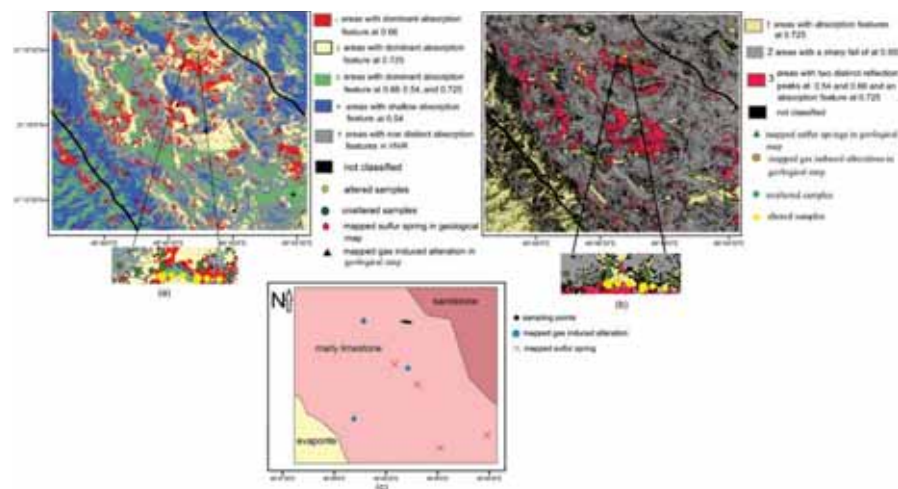


**Figure 6.10:** (a) Results obtained by the BRT classification with end-members extracted from the purest image pixels of WV-2. (b) BRT classification using ROIs co-located with ground samples. (c) Geological map of the study area.

The result of the BRT classification of the multiple band imagery is shown in figure 6.11. Three sets of ROIs were used for the classification of the multiple band imagery; classification using ROIs co-located with the purest pixels of ASTER (Figure 6.11a), classification using ROIs co-located with the purest pixels of the WV-2 (Figure 6.11b), and classification using ROIs co-located with ground truths (Figure 6.11c). The idea of using three ROIs for the BRT classification of multiple band imagery was to learn with, which ROIs altered and unaltered areas can be better distinguished and to what degree spatial

resolution of the WV-2 and its multispectral VNIR bands improve the classification of alteration. Class 1 displays the alteration zones in figures 6.11a and b, and class 3 is indicative of altered areas in figure 6.11c.

The predicted power of the classification using ROIs of pixels co-located with purest pixels of the ASTER is fair; the AUC has mean values of 0.62 (Table 6.2- scenario4). Two VNIR bands of the WV-2 and 4 SWIR bands of ASTER have the most contribution on the classification of altered areas. Using ROIs co-located with the purest pixels of the WV-2, the predicted power of the classification is fair; the AUC has mean values of 0.7 (Table 6.2- scenario5). The best discrimination among altered and unaltered areas was obtained by the BRT classification using ROIs co-located with ground truths. The predicted power of this classification is excellent; the AUC has mean values of 1 (Table 6.2- scenario6).

The SWIR bands of ASTER have higher contributions on three sets of classifications of alteration zone than WV-2 VNIR bands. Gypsum (shown in red color) is the alteration product of gas seep and the marine marly limestone formation composites of calcite and clays, which have diagnostic features in the SWIR range. This might be the reason why SWIR bands of ASTER have more influences on the classifications. However, sharp decreasing in the reflectance gradient between the visible red and the visible green-blue due to bleaching effects could be classified by the VNIR bands of the WV-2. It is worthwhile to comment that WV-2 bands 1 (0.425  $\mu\text{m}$ ) and 3 (0.545  $\mu\text{m}$ ) show high importance in all three classifications. The importance of band 1 (0.42  $\mu\text{m}$ ) can be related to sharp fall of spectra at this wavelength range related to Fe-OH and the importance of band 3 can be referred to the bleaching effects of the gas seep.

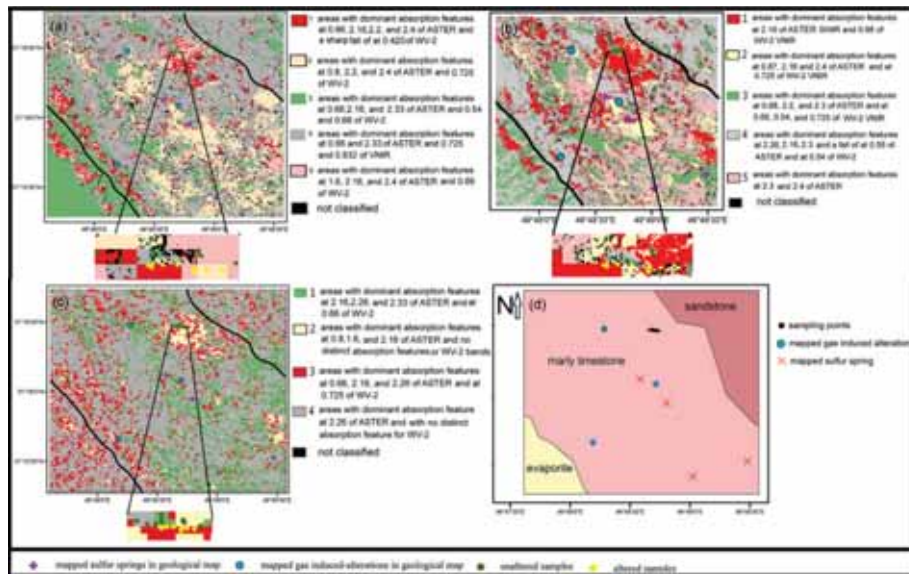


**Figure 6.11:** Results obtained by BRT classification of multiple band imagery created from ASTER and WV-2. **(a)** The BRT classification using ROIs co-located with the purest pixels of ASTER. **(b)** The BRT classification using ROIs co-located with the purest pixels of WV-2. **(c)** The BRT classification using ROIs co-located with sampling points. **(d)** The geological map of the study area.

**Table 6.2** Relative contributions (%) of predictor variables and AUC values for the BRT classifications of various scenarios.

Classification scenario	dataset	ROIs	Predictor variables with their relative contributions (%)	AUC (%)
1 (Figure 6.9)	ASTER	ROIs co-located with the purest pixels of the ASTER	b4 (42), b8 (22), b5(8), b6 (7.7), b2 (5.3), b9 (5.3), b3 (5), b1 (3), b7 (1.5)	62
2 (Figure 6.10a)	WV-2	ROIs co-located with the purest pixels of the WV-2	b3 (33), b5 (25), b8 (22), b4 (10), b1 (9.5),	68
3 (Figure 6.10b)	WV-2	ROIs co-located with ground samples	b3 (34), b1 (29), b4 (15), b2 (9), b8 (7), b5 (5.4)	93
4 (Figure 6.11a)	ASTER-WV-2	ROIs co-located with the purest pixels of the ASTER	WVb4 (38), WVb8 (16), ASb8 (12.5), ASb2 (8), ASb5 (7), ASb4 (5.8), ASb6 (4), WVb1 (2.5), WVb3 (2.5), ASb3 (2)	62
5 (Figure 6.11b)	ASTER-WV-2	ROIs co-located with the purest pixels of the WV-2	WVb3 (27.5), WVb8 (19), ASb9 (18), WVb5 (17.8), ASb6 (5), WVb4 (4), WVb1 (3.5), ASb2 (1.4),	70
6 (Figure 6.11c)	ASTER-WV-2	ROIs co-located with ground samples	ASb4 (25.5), ASb1 (22), ASb5 (20), ASb2 (11.11), ASb9 (9.4), ASb6 (5.3), WVb3 (3.6), WVb1 (2)	100

AS=ASTER, WV=WV-2, b=band, numbers inside parenthesis shows the relative contributions (%) of variables.

## 6.6. Discussion

The affected areas by the gas seep showed a larger extension in the satellite imageries than field observations. Results obtained by the BRT classification of ASTER using ROIs co-located with purest pixels of ASTER (Figure 6.9) showed a fair match with altered sampling points. Nevertheless, assessing the spatial correspondence between alterations mapped by image analyses of ASTER and ground truth is problematic because of the low spatial resolution of ASTER.

This research showed that SWIR bands of ASTER have been successful in mapping alteration minerals such as gypsum; however, the WV-2 would

increase the accuracy of such mapping (Figure 6.11) by enhancing the bleaching effect of hydrocarbon seeps (brightness) and providing detailed information about the presence of iron bearing minerals. Even though there are subtle differences among WV-2 spectral features of image pixels covering altered and unaltered samples, the classification accuracy can still be improved by integrating this dataset with higher spectral resolution. Among VNIR bands of WV-2, bands 2 (0.480  $\mu\text{m}$ ), 6 (0.725  $\mu\text{m}$ ), and 7 (0.835  $\mu\text{m}$ ) showed the lowest influence on the classification of the multiple band imagery (Table 6.2).

As some other objects on the ground have similar spectral features with iron bearing minerals, the results of the WV-2 classification should be interpreted with detailed study of land cover of an area of interest. In this research, the study area is without vegetation cover and roads, asphalt roofs, bituminous soil, and shadow are objects, which could be confused with target minerals. Image pixels covering altered samples (from field data) were classified as class 1 in the BRT classification of WV-2 using ROIs of purest pixels of the imagery (Table 6.2- scenario 2) and classified as class 3 in the BRT classification of WV-2 using ROIs co-located with sampling points (Table 6.2-scenario 3). The class 1 in the former classification represents the brightness (bleaching effects in seeps area) and the class 3 in the later classification illustrates the presence of ferric iron bearing minerals. Thus, those classes are not unique to the alteration zone.

WV-3 is planned for launch in 2014 with 8 spectral bands in VNIR (similar to WV-2) and additional 8 bands in the SWIR (Kruse and Perry, 2013). Four bands of SWIR WV-3 would be ranged between 1.2  $\mu\text{m}$  to 1.7  $\mu\text{m}$  and another four bands would be ranged between 2.165  $\mu\text{m}$  to 2.33  $\mu\text{m}$  (Worldview-3, 2013). As many alteration minerals have diagnostic features in SWIR particularly between 2-2.5  $\mu\text{m}$ , geologists would get more benefits from this unique dataset with more bands in this wavelength range. WV-3 can compensate site specific limitations of hyperspectral airborne and provides geologists with a super-efficient dataset in space for mineral mapping. This study showed that few VNIR bands of the WV-2 are useful in classification of alteration minerals. There is decreased capability to define key spectra of alteration minerals with decreasing spectral resolution. If the spectral bands are inadequate, neither spatial resolution matters for mineral mapping. It is expected that SWIR bands of WV-3 can potentially improve geological applications of remote sensing.

In practice, ground truths and geological maps are two traditional ways to obtain information about the accuracy of a classification with geological purposes. However, geological maps are limited to general information of geological formations and do not provide detailed information about highly heterogeneous nature of lithological units. Ground truths are usually collected around a site of interest and do not provide complete coverage of entire areas. It

is significant to note that in geological applications such as studying alterations assessing the local spatial correspondence between ground truths and identified minerals by image analysis provides geologists a better understanding of the potential of a specific technique for mapping the spatial distributions of target minerals. Therefore, the classifications of this research were assessed using the AUC technique that take into account the spatial correspondence between ground truths and the classified imagery.

## **6.7. Conclusion**

This research utilized remote sensing techniques to detect alterations related to gas seeps and explore the potential of the WV-2 for enhancing the bleaching effects of seeps. The results of this study demonstrated that alterations related to the gas seeps in the Mamatin area can be mapped by ASTER and WV-2 imageries. In addition, altered areas displayed in the geologic map and two other new areas with similar spectral features to the alteration product (gypsum) in the marly limestone formation were identified by remote sensing techniques. Integrating of the WV-2 into the ASTER improved the spatial accuracy of alterations mapping. It is suggested that WV-2 dataset can provide a potential tool along higher spectral resolution data for mapping alteration minerals related to hydrocarbon seeps in arid and semi-arid areas.

Study of alterations often focuses at a local scale and a method estimating the accuracy of classified areas against ground truths has more benefits for geologists than evaluating accuracy assessment of the entire imagery. The AUC accuracy assessment method provided us a statistic measure to evaluate the correctness of classified alterations. The BRT classification of the multiple band imagery using ROIs around field observations showed the perfect discrimination. It is expected that coming WV-3 dataset would be a promising dataset in studying hydrocarbon seep-induced alterations particularly in places where alterations cover small areas.

## **7. Synthesis**

## 7.1 Introduction

The objective of this thesis was the characterization and remote detection of hydrocarbon seep-induced alteration. Integration the results obtained from remote sensing study with geological and geochemical data led to a better understanding of processes that caused such alteration. This chapter summarizes the achievement and results of chapters 3 to 6 and discusses the results with respect to research objectives. The objectives were defined as:

- Modelling of the occurrence of hydrocarbon seeps in relation to their associations with geological features at a regional scale (Section 7.2)
- Spectral and geochemical characterization of alteration associated with different types of seeps (oil and gas) and various lithologies and getting a better understanding of the migration of oil and gas through the stratigraphy in relation to the various types of seeps in the Zagros belt (Section 7.3)
- Mapping boundaries between zones of compositional variations within evaporite cap rock in the Zagros petroleum system with ASTER imagery using a mineralogical boundary detection algorithm, named Rotational Template Matching (RTM) (Section 7.4)
- Detection of hydrocarbon seep-induced alteration from ASTER and WV-2 data and exploration of the potential of using high spatial resolution WV-2 imagery for mapping the alteration zone and improving the spatial accuracy of mapping (Section 7.4)

The following sections discuss the outcomes of the investigation of the spatial distribution of seeps at a regional scale, of studies in the field/laboratory and the spaceborne domain and new findings that came out of the research. The final section gives recommendations for future research.

## 7.2 Spatial pattern of hydrocarbon seeps

Chapter 3 showed that the studies of spatial pattern and spatial association of hydrocarbon seeps in a petroleum basin is instructive to determine the *most probable* migration pathways of hydrocarbon seeps from the *possible* one. An advantage of spatial analyses was the provision of empirical evidence for establishing a conceptual model of geological controls on hydrocarbon seep occurrences. The results of spatial analyses provided geo-information that was used as scientific basis for selecting potential areas for investigation of hydrocarbon entrapment in subsequent chapters. The results of the application of spatial analyses methods presented in chapter 3 can be undermined by the (lack of) quality and completeness of the datasets used and by the scale compatibility between the datasets. However, they provided insights into the kind of geological features that control the localization of hydrocarbon seeps at the surface and they brought important clues as to the importance of weighing of each feature on seeps occurrences. The results obtained from chapter 3

illustrated strong positive spatial associations of oil and gas seeps with the Gachsaran cap rock and the Mishan formation, implying upward migration of hydrocarbons through permeable micro-fractures and micro-pores in their strata. It was concluded that NW-SE and NNE-SSW faults and folds related fractures provided migration pathways for escaping hydrocarbons. Two scenarios were proposed for oil seep occurrences at the surface.

In the first scenario, the migration of oil from the reservoir to the evaporite cap rock and localization in the cap rock structures likely happened during the Miocene syntectonic deposition of the cap rock. Later, the reactivation of basement faults due to ongoing shortening of the Zagros produces fractures which provided migration pathways. The second scenario could have happened when N-S and NE-SW trending fractures formed by the shortening of the Zagros and reactivation of basement faults that led to breaching of the seal formation or superimposing the former structures. Based on the conceptual model proposed in chapter 3, marly limestone and evaporite formations were selected for further investigations in the field.

### **7.3 Field and laboratory studies**

After demonstrating that oil and gas seeps predominantly migrate upward in the stratigraphy through permeable micro-fractures and micro-pores, the next research objective involved the collection of field observations and spectral and geochemical analyses on rock samples taken from the Mishan and the Gachsaran Formations. The minerals within alteration facies showed distinctive spectral signatures, chemical compositions, and isotope ratios in the Gachsaran (cap rock) and the overlying Mishan Formation in the Zagros oil fields. Isotopic data successfully identified the origin of seeps and showed that surface alterations are related to subsurface reservoirs.

With regard to geological aspects, field observations confirmed the conceptual model proposed in chapter 3 in which micro-fractures and micro-pores are the most probable migration pathways of hydrocarbon seeps in the Zagros belt. In addition, the results of chapter 4 showed that chemistry of the evaporite cap rock is the main controlling factor on the type of hydrocarbon seeps occurring at the surface and the density of hydrocarbon seeps in the stratigraphy. The field observations showed that when the evaporite cap rock has a high clay and limestone content then the oil seeps could reach the surface. In contrast, in areas where the cap rock is rich in gypsum it acts as a more efficient seal which causes the density of gas seeps in the cap rock to be higher than the density of oil seeps. This may suggest that the density of hydrocarbon seeps are not decreased in the stratigraphy where the evaporite cap rock contains its other members than gypsum and anhydrite because those members are more prone to fracturing and can affect the permeability of the cap rock in relation to

hydrocarbon seeps. The results of field measurements showed that the compositional variation within the cap rock unit influenced the types of seeps and associated alteration at the surface. However, all interpretations are only based on surface observations. Subsurface data about the compositional variations within the cap rock would provide useful additional information.

In terms of the study of reflectance spectra of seep related alteration, attention was paid to the analysis of spectral characteristics of altered and unaltered samples such as the depth of absorption features, which has often been overlooked in spectral studies of hydrocarbon seep-induced alteration. Within the Mishan marly limestone formation, gas induced gypsum and sulfur were easily identified using their spectral signatures. Separation of oil induced secondary calcite from marine calcite was not possible because of their similar spectral signatures. Within the Gachsaran evaporite, secondary gypsum was successfully identified and differentiated from marine gypsum by evaluation of differences in depths of gypsum-related absorption features. Oil-induced calcite was also spectrally identified within the evaporite formation.

Chapter 4 presented the Boosted Regression Trees (BRT) method to predict alterations from depth of spectral absorption features. The influence of each absorption feature on the recognition of alteration was calculated by the BRT algorithm. The BRT was chosen over the other commonly used predictive modeling techniques such as logistic regression, partial least square and principal component regression, as the technique is not sensitive to outliers or anomalously high values. The method assumes that the data generating processes are complex and unknown and it tries to find dominant patterns. This method is suitable because in a real geological situation, field measurements may show high concentrations of certain chemical elements or deep absorption features related to high mineral abundances. These measurements are not outliers but key factors in interpretation of geological processes such as alteration related to hydrocarbon seeps.

#### **7.4 Spaceborne study**

Chapter 5 aimed at mapping the lithological boundary of the evaporite cap rock with spaceborne data. This chapter presented the application of the Rotation Template Matching algorithm (RTM) algorithm on the ASTER imagery for mapping lithological boundaries. The RTM successfully mapped boundaries between zones of compositional variation within the cap rock formation in the Zagros belt. The algorithm has been specified to detect mineralogical boundaries. The greatest advantage of the RTM algorithm over other methods of delineating lithological boundaries such as object oriented and pixel-based classification methods is that the template used is based on expert knowledge of lithological boundaries in the area under investigation. The spatial

correspondence of detected boundaries from the RTM with two series of reference boundaries was assessed by fuzzy set-based method. Results showed a higher spatial correspondence between RTM results and reference boundaries extracted from aerial photo than references boundaries extracted from geological maps. The added value of the assessment of spatial corresponds between detected boundaries and references was the possibility to define confidence regions around reference boundaries to handle errors of positional issues that are important for applications such as mineral and hydrocarbon explorations, water resource surveys, and natural hazard evaluation.

The RTM showed success in mapping compositional variation within lithologies of the petroleum system. Geological maps often do not display lithological variations within units or formations. Spectral remote sensing studies of petroleum basins that aim at basin stratigraphic interpretations would get benefits from the application of such techniques for mapping compositional variations within lithologies using expert knowledge.

The last research objective involved detecting gas-induced alterations from ASTER and WV-2 satellite data. The analyses of ASTER and WV-2 imagery successfully detected alterations in areas of field sampling. In addition, alterations related to gas seeps shown in the geological map and two new potential areas of hosting gas seeps were also captured by image analyses. Such results showed a great promise to detect altered areas by satellite data even without field sampling, which gives geologists an opportunity to plan an efficient future field work.

ASTER and WV-2 data were classified by the BRT algorithm using different kind of training data. The BRT is a nonparametric supervised classification algorithm that fits complex nonlinear relationship by combining two algorithms of classification and regression tree (CART) and boosting. Altered areas could be mapped by spectral mapping of ASTER; however, assessing results with ground truths was problematic due to the different spatial scale of ASTER data and ground truths.

The result of the BRT classification for the WV-2 using training data around sampling point was very good; the AUC had mean values of 0.93. Nevertheless, some classes are not unique to the alteration zone and they were confused with asphalt roads and/or shadows. This misclassification could be identifiable using the very high spatial resolution WV-2 (0.5 m). The research showed that SWIR bands of ASTER have been used successfully in mapping alteration minerals; however, the VNIR bands of WV-2 could increase the accuracy of such mapping by enhancing the bleaching effect of hydrocarbon seeps (brightness). Even though there are subtle differences among WV-2 spectral features of pixels co-located with altered and unaltered areas, the classification accuracy is improved by integrating this dataset with ASTER.

The AUC method was chosen to evaluate the spatial correspondence between classified image pixels and ground truths. In geological applications such as study of alterations, assessing results by verification with carefully selected field samples provides geologist more reliable information about the classification than assessment using the entire image.

## **7.5 Hydrocarbon seep and alteration; progress made**

### **7.5.1 Understanding the relationship between the geology and hydrocarbon seeps**

The usage of hydrocarbon seeps as direct indicators of the presence of petroleum at the subsurface has served petroleum exploration campaigns for many years. What to do when natural hydrocarbon seeps are found? Although the presence of seeps has a great value for pre-drill exploration, seeps are not always vertically connected to subsurface reservoirs. Most attention has been paid to the value of seeps in finding subsurface reservoirs and fewer attempts have been made to use seeps as one of inputs of information for basin interpretations.

After finding a visible seep, exploration plans tend to focus on relating the seep to the subsurface reservoirs. However, questions such as: "Why seeps are localized at specific locations?", "What is the role of host rocks on the localization of seeps?", "Do the spatial pattern of seeps related to the chemistry of cap rocks at a regional scale?", "How can the composition of cap rocks and other host rocks influence the type of seeps occurring at the surface?", and "Is the density of seeps decreasing with age in a stratigraphic sequence? Why?" are often overlooked. Answers to these questions provide valuable geological and geochemical information about a petroleum basin. Offshore, seeps have been widely studied in terms of basin geology and petroleum dynamics but such studies are poorly documented for onshore basins.

The outcomes of this research demonstrated that understanding the relationship between hydrocarbon seeps and geology provides information about petroleum basins particularly about the influence of compositional variation within the cap rock formation on the types of seeps occurring at the surface and movement of hydrocarbons in the stratigraphy.

Although these indications should be carefully analyzed together with available subsurface data, they may bring clues to the petroleum basin productivity. At this specific site of the current research, Zagros, hydrocarbon seeps mostly occur in the cap rock formation; thus, they can provide us information about the permeability of cap rock. There are areas where seeps can be found in reservoirs that are exposed at the surface. In such areas, the study of diagenetic mineral

heterogeneities and their spatial pattern distribution would provide useful information about the reservoir productivity and fluid-flow migration pathways.

The obtained results in this thesis can be further improved by the use of subsurface data. It is doubtful whether subsurface migrations of hydrocarbons will be fully understood because of the complexity of the phenomena that are controlled by many factors. Most of the interpretations are only based on basic principles of science and our observations. However, surface observations and analyses of hydrocarbon seeps can help us to a better understanding of oil/gas migration in the stratigraphy. Such studies about other petroleum basins would provide valuable information about the efficiency or permeability of different types of cap rocks; thus, they can have implications for petroleum reservoirs on a global scale.

### **7.5.2 More benefits from remote sensing studies to the oil and gas industry**

Remote sensing studies of onshore hydrocarbon seeps have been focused on detection of seeps either as direct detection of seeps or detection of indirect evidences of the presence of seeps. However, there are not any new natural onshore seeps found by remote sensing tool neither any new information has been added to the database of petroleum basins. Based on published studies, remote sensing has been applied to detect what we already know about its presence. What has been done in onshore basins is trying to prove the ability of remote sensing in detecting something has been detected before by other exploration methods. It is notable that hydrocarbon seeps are often displaced from sources originate them; thus, they often are not vertically connected to the subsurface reservoirs. Remote sensing should not be thought as a black magic tool of spotting locations of seeps and/or detecting indirect evidences of seeps. Remote sensing studies provide surface information about hydrocarbon seeps and associated alteration. If such studies aimed at only spotting locations of seeps and their associated alterations, they may only prove the existence of a mature source rock in the subsurface. The application of remote sensing study of seeps in the oil and gas industry could be widened by basin interpretations at a regional scale. Figure 7.1 and Figure 7.2 show examples of three giant oil fields in the Zagros; Masjid-Soleyman oil field in the north and the Gachsaran and Bibi-Hakimeh oil fields in the south of the Dezful Embayment, respectively. Figure 7.1 shows higher densities of oil seeps in areas of the Gachsaran cap rock formation (in magenta color) where it is relatively rich in limestone and clay (green-blue colors within the magenta-colored formation). Limestone and clay are more prone to fracturing during tectonic activity; thus, they can provide migration pathways for oil to reach the surface through the cap rock formation. In contrast, the probability of finding gas seeps is higher than oil seeps in areas of the cap rock that contains more gypsum (magenta color)

(Figure 7.2). In these rocks the gypsum layers prevent the leaking oil from reaching the surface.

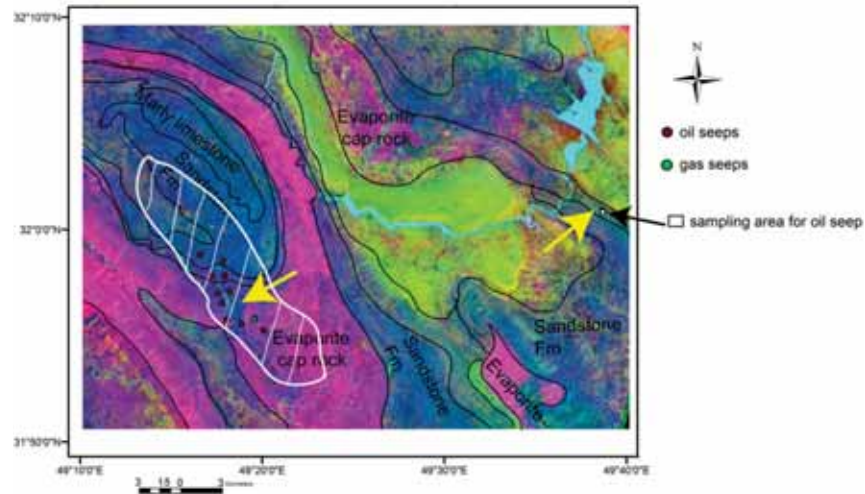


**Figure 7.1:** ASTER color composite of Masjid-Soleyman oil field (north of the Dezful Embayment) to show the spatial distribution of oil and gas seeps with different composition of the Gachsaran cap rock (in magenta color). Ratio of  $b_4/(b_6+b_9)$  enhances gypsum (magenta color),  $(b_7+b_9)/b_8$  enhances calcite (green color),  $(b_5+b_7)/b_6$  enhances clay (blue color). Yellow arrows pointing at areas of the cap rock formation that contains limestone and clay with higher number of oil seeps. Black arrow shows location of field measurements over oil seeping area. White polygon shows the extension of subsurface Masjid-soleyman reservoir.

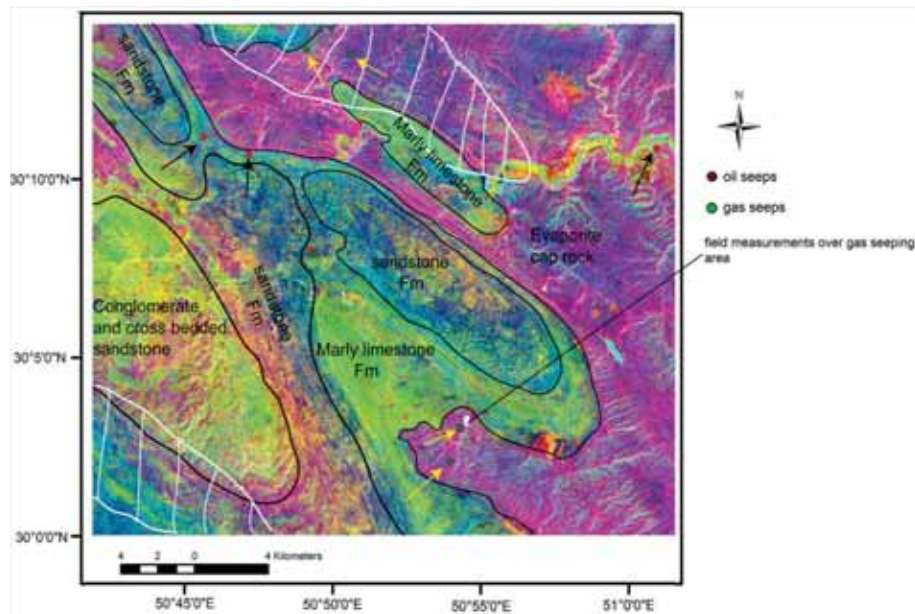


**Figure 7.2:** ASTER color composite of Gachsaran oil field (south of the Dezful Embayment) to show the spatial distribution of oil and gas seeps with different composition of the Gachsaran cap rock (in magenta color). Ratio of  $b_4/(b_6+b_9)$  enhances gypsum (magenta color),  $(b_7+b_9)/b_8$  enhances calcite (green color),  $(b_5+b_7)/b_6$  enhances clay (blue color). Yellow arrows pointing at areas of the cap rock formation that are rich in gypsum and host gas seeps. Black arrows pointing at areas of the cap rock formation and other host rocks that are rich in clay and limestone and host oil seeps. White polygons show the extension of subsurface Gachsaran and Bibi-Hakimeh reservoirs.

Figure 7.3 shows a schematic model of the influence of cap rock composition on the type of hydrocarbon seeps occurring at the surface. It is assumed that oil and gas could escape from the reservoirs through the seal based on the two scenarios proposed in chapter 3. In areas where the cap rock formation contains more limestone and clay, the probability of finding oil seeps at the surface is higher than areas where the cap rock formation contains high contents of gypsum. The oil migration gets interrupted by impermeable gypsum members while clay and limestone members provide a network of fractures for oil migration as they are more prone to fracturing during the tectonic activity. Gas seep could reach the surface through micro pores and micro fractures even when the cap rock is efficient. The seeping gas can leak directly from subsurface reservoir and/or it may be a secondary product of the interaction between hydrocarbons and sediments in the subsurface (as shown in Figure 2.2).

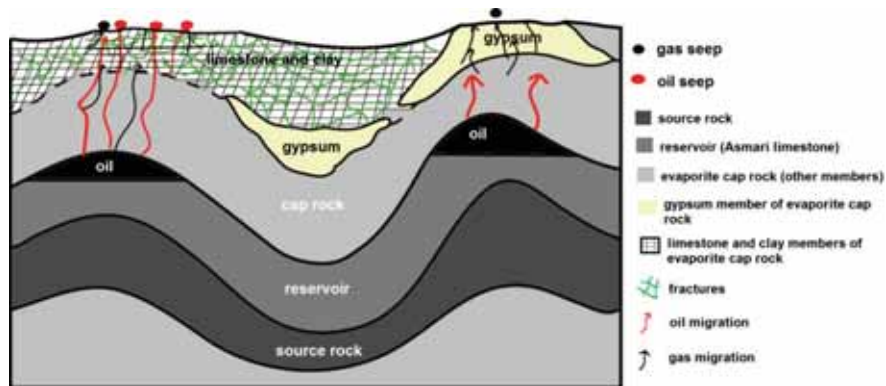


**Figure 7.3:** A schematic model of influence of cap rock heterogeneity on the type of hydrocarbon seeps occur at the surface. Red arrows show oil seep migration and black arrows display gas seep migration.

## 7.6 Future work

This research showed the importance of studying seeps and their associated alterations at a regional scale. There are a number of opportunities for further research:

- Spectral measurements of a drill core from seep alteration zones. Mineralogical and lithological logging of drill core can provide reliable information in a petroleum basin. Spectroscopy of drill core is cost effective and would allow us to map alteration mineralogy in the subsurface. Combining subsurface diagenetic mineralogy with surface alteration map can be used to a better understanding of hydrocarbons movement in the subsurface and their spatial pattern in stratigraphy, which are important factors in seeps migration modeling.
- Monitoring temporal patterns of mineralization. The Leakage of hydrocarbons to the surface can be continuous or might be episodic by interruption of impermeable barriers or tectonically driven discharge from reservoirs. Mineralization related to hydrocarbon seep may take more than two decades. In areas such as the Zagros where the discovery of seeps is back to 1920, there are high possibilities to find alterations related to paleoseeps and/or active seeps. Study of temporal pattern of mineralization with their spatial pattern would allow us to find the most probable active migration pathways, reconstruction of fluid pathways, understanding factors controlling the occurrence of seeps at the surface, investigating of hydrocarbon seeps rate, efficiency of cap rocks, factors affecting mineralization, and probably evaluating the maturity of source rocks.

- Analogue modelling. Analogue models can be used to simulate different scenarios about the influence of different compositions of cap rock on hydrocarbon seep movements in the stratigraphy. These models can provide insights into the most probable migration pathways of hydrocarbons in the subsurface and can be used to further develop the results that were obtained in this research.
- Include the Thermal Infrared (TIR) range. TIR has been applied to detect coal-fire related temperature anomalies (Gangopadhyay et al., 2005; Kuenzer et al., 2007; Zhang et al., 2004). TIR study of gas seeps has so far been overlooked in remote sensing applications for petroleum explorations. In petroleum basins such as the Zagros belt where there are some areas contain fire flames related to gas seeps, TIR holds a great promise to detect such seep-fires related temperature anomalies.
- Airborne geophysical data. Airborne geophysical data can provide useful information about boundaries of various rock types, their structures, and discontinuities caused by deformation zone in bed rocks. Aeromagnetic data can be used to detect demagnetization of sediments due to reaction between sedimentary rocks and hydrocarbon seeps.



## Bibliography

- Abdollahi Fard, M., Sepehr, M., and sherkati, S., 2011, Neogene salt in SW Iran and its interaction with Zagros folding: *Geological Magazine*, v. 148, p. 854-867.
- Abrams, M., 1996, Distribution of subsurface hydrocarbon seepage in near-surface marine sediments: In D. Schumacher and M.A. Abrams, eds., *Hydrocarbon migration and near surface expression: AAPG Memoir 66*, p. 1-14.
- , 2005, Significance of hydrocarbon seepage relative to petroleum generation and entrapment: *Marine and Petroleum Geology*, v. 22, p. 457-477.
- Alavi, M., 2004, Regional stratigraphy of the Zagros fold-thrust belt of Iran and its proforland evolution: *American journal of science*, v. 304, no. January, p. 1-20.
- Alshahrhan, A., and Nairn, A., 1997, *Sedimentary basins and petroleum geology of the middle east.*: Elsevier publishing
- Altman, D., 1994, Fuzzy set theoretic approaches for handling imprecision in spatial analysis: *International Journal of Geographical Information Systems*, v. 8, p. 271- 291.
- Bahroudi, A., and Koyi, H. A., 2004, Tectono-sedimentary framework of the Gachsaran Formation in the Zagros foreland basin: *Marine and Petroleum Geology*, v. 21, no. 10, p. 1295-1310.
- Bammel, B. H., and Birnie, R. W., 1994, Spectral reflectance response of big sagebrush to hydrocarbon-induced stress in the Bighorn Basin, Wyoming: *Photogrammetric Engineering and Remote Sensing*, v. 60, no. 1, p. 87-96.
- Berberian, M., 1995, Master "blind" thrust faults hidden under the Zagros folds: active basement tectonics and surface morphotectonics: *Tectonophysics*, v. 241, no. 3-4, p. 193-195.
- Berberian, M., and King, G. C. P., 1981, Towards a paleogeography and tectonic evolution of Iran.: *Cnadian Journal of Earth Sciences*, v. 18, p. 210-265.
- Berman, M., 1977, Distance distributions associated with Poisson processes of geometric figures.: *Journal of Applied Probability*, v. 14, p. 195-199.
- Beydoun, Z. R., Hughes, M. W., and Stoneley, R., 1992, Petroleum in the Zagros Basin: a late Tertiary foreland basin overprinted onto the outer edge of the vast hydrocarbon-rich Paleozoic–Mesozoic passive margin shelf In: R.W. Macqueen and D.A. Leckie, Editors, *Foreland basins and fold belts*, AAPG Bulletin Memoir v. 55, p. 307-336.
- Bonham-Carter, G. F., 1994, *Geographic information systems for geoscientists: modelling with GIS. Computer Methods in the Geosciences: Pergamon Press, Oxford, U.K.* , v. 13, p. 398 p.
- Bordenave, M. L., 2002, The Middle Cretaceous to Early Miocene petroleum system in the Zagros domain of Iran, and its prospect evaluation.: *AAPG Annual Meeting, Houston, Texas, March*, p. 10-13.

- Bordenave, M. L., and Hegre, J. A., 2005, The influence of tectonics on the entrapment of oil in the Dezful Embayment, Zagros foldbelt, Iran Journal of Petroleum Geology, v. 28, no. 4, p. 339-368.
- Bordenave, M. L., and Hegre, J. A., 2010, Current distribution of oil and gas field in the Zagros fold belt of Iran and contiguous offshore as the result of the petroleum systems: Geological society of London, v. 330, p. 291-353.
- Bowen, B., Martini, B. A., Chan, M. A., and Parry, W. T., 2007, Reflectance spectroscopic mapping of diagenetic heterogeneities and fluid-flow pathways in the Jurassic Navajo Sandstone: AAPG Bulletin, v. 91, no. 2, p. 173-190.
- Breiman, L., 2001, Statistical modeling: the two cultures: Statistical Science, v. 16, p. 199-215.
- Breiman, L., Friedman, J. H., Olshen, R. A., and Stone, C. G., 1984, Classification and Regression Trees. Wadsworth International Group, Belmont, California, USA.
- Cai, C., Worden, R. H., Bottrell, S. H., Wang, L., and Yang, C., 2003, Thermochemical sulphate reduction and the generation of hydrogen sulphide and thiols (mercaptans) in Triassic carbonate reservoirs from the Sichuan Basin, China: Chemical Geology, v. 202, p. 39-57.
- Carranza, E. J. M., 2009a, Controls on mineral deposit occurrence inferred from analysis of their spatial pattern and spatial association with geological features: Ore Geology Reviews, v. 35, no. 3-4, p. 383-400.
- , 2009b, Geochemical anomaly and mineral prospectivity mapping in GIS: Handbook of exploration and environmental geochemistry, Vol. 11 (M. Hale, Editor), v. Elsevier B.V. .
- Carranza, E. J. M., and Sadeghi, M., 2010, Predictive mapping of prospectivity and quantitative estimation of undiscovered VMS deposits in Skellefte district (Sweden): Ore Geology Reviews, v. 38, no. 3, p. 219-241.
- Carruba, S., Cesare, R. P., Buonaguro, R., Calabro, R., Carpi, R., and Naini, M., 2006, Structural pattern of the Zagros fold-and-thrust belt in the Dezful Embayment (SW Iran): Geological society of America, p. 11-32.
- Chapman, M. A., Alesheikh, A., and Karimi, H., 2003, Error Modeling and Management for Data in Geospatial Information Systems- In: D.R. Green and S.D. King (eds.), Coastal and Marine Geo-Information Systems: Kluwer Academic Publishers, p. 355-369.
- Chavez, J., Stuart, C., and Anderson, J. A., 1991, Comparison of three different methods to merge multiresolution and multispectral data: Landsat TM and SPOT panchromatic: Photogrammetric Engineering & Remote Sensing, v. 57, no. 3, p. 295-303.
- Clark, R. N., and Roush, T. L., 1984, Reflectance spectroscopy-quantitative analysis techniques for remote sensing applications: Journal of geophysical research, v. 89, p. 6329-6340.

- Clarke, R. H., and Cleverly, R. W., 1991, petroleum seepage and post-accumulation migration. In: petroleum migration (Eds W.A. England and A. J.Fleet). Geological Society of London, Special Publication No.59, p. 265-271.
- Cloutis, E., 1989, Spectral reflectance properties of hydrocarbons: Remote sensing implications: *Science* v. 245, p. 165-168.
- Cloutis, E. A., Hawthorne, F. C., Mertzman, S. A., Krenn, K., Craig, M. A., Marcino, D., Methot, M., Strong, J., Mustard, J. F., Blaney, D. L., Bell III, J. F., and Vilas, F., 2006, Detection and discrimination of sulfate minerals using reflectance spectroscopy: *Icarus*, v. 184, no. 1, p. 121-157.
- Crosta, A. P., Sabine, C., and Taranik, J. V., 1998, Hydrothermal alteration mapping at Bodie, California, using AVIRIS hyperspectral data: *International Journal of Remote Sensing*, v. 65, p. 309–319.
- Crowley, J. K., Brickey, D. W., and Rowan, L. C., 1989, Airborne imaging spectrometer data of the Ruby Mountains, Montana: mineral discrimination using relative absorption band-depth images.: *Remote Sensing of Environment*, v. 29, p. 121-134.
- Crowley, J. K., Williams, D. E., Hammarstrom, J. M., Piatak, N., Chou, I. M., and Mars, J. C., 2003, Spectral reflectance properties (0.4-2.5  $\mu\text{m}$ ) of secondary Fe-oxides, Fe hydroxide, and Fe-sulfate-hydrate minerals associated with sulfide bearing mine wastes: *Geochemical exploration environment analysis*, v. 3, p. 219-228.
- Cudahy, T. J., Hewson, R. D., Caccetta, M. S., Roache, A., Whitbourn, L. B., Connor, P., Coward, D., Mason, P., Yang, K., Huntington, J. F., and Quigley, M. A., 2009, Drill core logging of plagioclase feldspar composition and other minerals associated with archaean gold mineralization at Kambalda, Western Australia, using a bidirectional thermal infrared reflectance system: *Reviews in economic geology*, v. 16, p. 225-235.
- De Boever, E., Huysmans, M., Muchez, P., Dimitrov, L., and Swennen, R., 2009, Controlling factors on the morphology and spatial distribution of methane-related tubular concretions – Case study of an Early Eocene seep system: *Marine and Petroleum Geology*, v. 26, no. 8, p. 1580-1591.
- Ding, F., Spiess, V., Bruening, M., Fekete, N., Keil, H., and Bohrmann, G., 2008, A conceptual model for hydrocarbon accumulation and seepage processes around Chapopote asphalt site, southern Gulf of Mexico: From high resolution seismic point of view: *Journal of Geophysical Research*, v. 113.
- Douglas Elmore, R., and Farrand, W. R., 1981, Asphalt-Bearing Sediment in Synorogenic Miocene-Pliocene Molasse, Zagros Mountain, Iran: *AAPG Bulletin*.
- Edgell, H., 1996, Salt tectonism in the Persian Gulf Basin. In: Alsop, G. I., Blundell, D. J., and Davison, I. (eds.) *Salt Tectonics*.: Geological Society, London, Special Publications, v. 100, p. 129-151.

- Elith, J., Graham, C. H., Anderson, R. P., and al., e., 2006, Novel methods improve prediction of species' distributions from occurrence data: *Ecography*, v. 29, p. 129-151.
- Elith, J., Leathwick, J. R., and Hastie, T., 2008, A working guide to boosted regression trees: *Journal of Animal Ecology*, v. 77, no. 4, p. 802-813.
- Ellis, J. M., Davis, H. H., and Zamudio, J. A., 2001, Exploring for onshore oil seeps with hyperspectral imaging: *Oil and Gas Journal*, v. Sept. 10, p. 49-56.
- Espindola, G. M., Camara, G., Reis, I. A., Bins, L. S., and Monteiro, A. M., 2006, Parameter selection for region-growing image segmentation algorithms using spatial autocorrelation: *International Journal of Remote Sensing*, v. 27, no. 14, p. 3035 — 3040.
- Etioppe, G., 2009, A global dataset of onshore gas and oil seeps: a new tool for hydrocarbon exploration: *Oil and Gas business*, no. 2.
- Etioppe, G., and Klusman, R. W., 2010, Microseepage in drylands: Flux and implications in the global atmospheric source/sink budget of methane: *Global and Planetary Change*, v. 72, no. 4, p. 265-274.
- Etioppe, G., Papatheodorou, G., Christodoulou, D., Ferentinos, G., Sokos, E., and Favali, P., 2006, Methane and hydrogen sulfide seepage in the NW Peloponnesus petroliferous basin (Greece): origin and geohazard: *AAPG Bulletin*, v. 90, no. 5, p. 701-713.
- Falcon, N. L., 1974, Southern Iran: Zagros Mountains. In: Spencer, A. (Ed.), *Mesozoic–Cenozoic Orogenic Belts: Geological Society of London, Special Publication*, v. 4, p. 199–211.
- Ferrier, G., Wadge, G., 1996, Application of imaging spectrometry data to mapping alteration zones associated with gold mineralization in southern Spain: *International Journal of Remote Sensing*, v. 17, p. 331–350.
- Fielding, A. H., and Bell, J. F., 1997, A review of methods for the assessment of prediction errors in conservation presence/absence models: *Environmental Conservation*, v. 24, no. 01, p. 38-49.
- Filho, C., Miranda, F. P., and YAMakawa, T., 1999, Remote detection of a tonal anomaly in an area of hydrocarbon microseepage, Tucano basin, north-eastern Brazil: *International Journal of Remote Sensing*, v. 20, no. 13, p. 2683- 2688.
- Fillho, A., 2002, Remote detection of hydrocarbon microseepage induced soil alteration: *International Journal of Remote Sensing* v. 23, no. 18, p. 3523–3524.
- Foody, G., 1999, The continuum of classification fuzziness: *Photogrammetric Engineering and Remote Sensing of Environment*, v. 65, p. 443-451.
- , 2002, Status of land cover classification accuracy assessment: *Remote Sensing of Environment*, v. 80, p. 185–201.
- Friedl, M. A., and Brodley, C. E., 1997, Decision tree classification of land cover from remotely sensed data: *Remote Sensing of Environment*, v. 61, p. 399– 409.

- Friedman, J. H., and Meulman, J. J., 2003, Multiple additive regression trees with application in epidemiology: *Statistics in Medicine*, v. 22, p. 1365-1381.
- Fry, N., 1979, Random point distributions and strain measurement in rocks: *Tectonophysics*, v. 60, p. 89-105.
- Fu, B., Zheng, G., Ninomiya, Y., Wang, C., and Sun, G., 2007, Mapping hydrocarbon-induced mineralogical alteration in the northern Tian Shan using ASTER multispectral data: *Terra Nova*, v. 19, no. 4, p. 225-231.
- Gangopadhyay, P. K., Maathuis, B., and Van Dijk, P., 2005, ASTER-derived emissivity and coal-fire related surface temperature anomaly: a case study in Wuda, north China: *International Journal of Remote Sensing*, v. 26, no. 24, p. 5555-5571.
- Getis, A., 1994, Spatial dependence and heterogeneity and proximal databases: In: Fotheringham, S. and Rogerson, P. (eds), *Spatial Analysis and GIS* v. London: Taylor & Francis, p. 105-120.
- Getis, A., and Ord, J. K., 1992, The analysis of spatial association by use of distance statistics: *Geographical Analysis*, v. 24, p. 189-206.
- Gill, W. D., and Ala, M. A., 1972, Sedimentology of Gachsaran Formation (Lower Fars Series), Southwest Iran: *AAPG Bulletin*, v. 56, p. 1965-1974.
- Gleeson, D. F., Pappalardo, R. T., Grasby, S. E., Anderson, M. S., Beauchamp, B., Castaño, R., Chien, S. A., Doggett, T., Mandrake, L., and Wagstaff, K. L., 2010, Characterization of a sulfur-rich Arctic spring site and field analog to Europa using hyperspectral data: *Remote Sensing of Environment*, v. 114, no. 6, p. 1297-1311.
- Gomez, C., Delacourt, C., Allemand, P., Ledru, P., and Wackerle, R., 2005, Using ASTER remote sensing data set for geological mapping, in Namibia: *Physics and Chemistry of the Earth, Parts A/B/C*, v. 30, no. 1-3, p. 97-108.
- Gong, p., 1996, Integrated analysis of spatial data from multiple sources: using evidential reasoning and artificial neural network techniques for geological mapping: *Photogrammetric Engineering & Remote Sensing*, v. 62, no. 5, May, p. 513-523.
- Green, A. A., and Craig, M. A., 1985, Analysis of aircraft spectrometer data with logarithmic residuals.: proceedings of the airborne imaging spectromete data analysis workshop, v. April 8010 no. JPL publication, p. 111-119.
- Guo, P., and Tanaka, H., 2001, Fuzzy DEA: a perceptual evaluation method: *Fuzzy Sets and Systems*, v. 119, no. 1, p. 149-160.
- Hagen, A., 2003, Fuzzy set approach to assessing similarity of categorical maps: *International Journal of Geographical Information Science*, v. 17, no. 3, p. 235-249.

- Hessami, K., Koyi, H. A., and Talbot, C. J., 2001, The significance of strike-slip faulting in the basement of the Zagros fold and thrust belt: *Journal of Petroleum Geology*, v. 24, no. 1, p. 5-28.
- Hewson, R. D., Cudahy, T. J., Mizuhiko, S., Ueda, K., and Mauger, A. J., 2005, Seamless geological map generation using ASTER in the Broken Hill-Curnamona province of Australia: *Remote Sensing of Environment*, v. 99, no. 1-2, p. 159-172.
- Horig, B., K $\ddot{u}$ hn, F., Osch $\ddot{u}$ tz, F., and Lehmann, F., 2001, Hymap hyperspectral remote sensing to detect hydrocarbons: *International Journal of Remote Sensing*, v. 22, no. 8, p. 1413-1422.
- Horvitz, L., 1972, Vegetation and geochemical prospecting for petroleum: *American Association of Petroleum Geologists Bulletin (AAPG)*, v. 56, no. 5, p. 925-940.  
[http://www.ga.gov.au/image\\_cache/GA7833.pdf](http://www.ga.gov.au/image_cache/GA7833.pdf).  
<http://www.iso-analytical.co.uk/geochemistry.html>.
- Huang, B., Xiao, X., Li, X., and Cai, D., 2009, Spatial distribution and geochemistry of the nearshore gas seepages and their implications to natural gas migration in the Yinggehai Basin, offshore South China Sea: *Marine and Petroleum Geology*, v. 26, no. 6, p. 928-935.
- Huang, L. K., and Wang, M. J., 1995, Image thresholding by minimizing the measure of fuzziness: *Pattern Recognition*, v. 28, p. 41-51.
- Hubbard, B. E., Crowley, J. K., and Zimbelman, D. R., 2003, Comparative alteration mineral mapping using visible to shortwave infrared (0.4-2.4  $\mu$ m) Hyperion, ALI, and ASTER imagery: *Geoscience and Remote Sensing, IEEE Transactions on*, v. 41, no. 6, p. 1401-1410.
- Hunt, G. R., 1977, Spectral signatures of particulate minerals in the visible and near infrared.: *Geophysics*, v. 42, no. 3, p. 501-513.
- Hunt, G. R., Salisbury, J.W., 1975, Mid-infrared spectral behavior of sedimentary rocks: Technical Report AFRCL-TR-75-0356, US Air Force Cambridge Research Laboratory, v. Cambridge, MA.
- James, G. A., and Wynd, J. G., 1965, Stratigraphic nomenclature of Iranian oil consortium agreement area: *AAPG Bulletin*, v. 49, p. 2182-2245.
- Jin, Y. K., Kim, Y.-G., Baranov, B., Shoji, H., and Obzhirov, A., 2011, Distribution and expression of gas seeps in a gas hydrate province of the northeastern Sakhalin continental slope, Sea of Okhotsk: *Marine and Petroleum Geology*, v. 28, no. 10, p. 1844-1855.
- Jones III, V., and Burtell, S., 1996, Hydrocarbon flux variations in natural and anthropogenic seeps: In D. Schumacher and M.A. Abrams, eds., *Hydrocarbon migration and near surface expression: AAPG Memoir 66*, p. 203-221.
- Kashfi, M., 1980, Stratigraphy and Environmental Sedimentology of Lower Pars Group (Miocene), South-Southwest Iran: *The American Association of Petroleum Geologists*, v. 64, p. 2095-2107.

- Khan, S., and Jacobson, S., 2008, Remote sensing and geochemistry for detecting hydrocarbon microseepages: Geological Society of America v. 120, p. 96-105.
- Khan, S. D., and Mahmood, K., 2008, The application of remote sensing techniques to the study of ophiolites: *Earth-Science Reviews*, v. 89, no. 3-4, p. 135-143.
- Klusman, R. W., and Saeed, M. A., 1996, Comparison of light hydrocarbon microseepage mechanisms: In: Schumacher, D. & Abrams, M.A. (eds.): *Hydrocarbon migration and its near-surface expression: AAPG Memoir*, v. 66, p. 157-168.
- Kohavi, R., 1995, A study of cross-validation and bootstrap for accuracy estimation and model selection, *Proceedings of the 14th international joint conference on Artificial intelligence - Volume 2: Montreal, Quebec, Canada*, Morgan Kaufmann Publishers Inc., p. 1137-1143.
- Kruse, F., and Perry, S., 2013, Mineral Mapping Using Simulated Worldview-3 Short-Wave-Infrared Imagery: *Remote Sensing*, v. 5, no. 6, p. 2688-2703.
- Kruse, F. A., Lefkoff, A. B., Boardman, J. B., Heidebreicht, K. B., Shapiro, A. T., Barloon, P. J., and Goetz, A. F. H., 1993, The Spectral Image Processing System (SIPS) – interactive visualization and analysis of imaging spectrometer data: *Remote Sensing of Environment*, v. 44, p. 145–163.
- Kuenzer, C., Zhang, J., Li, J., Voigt, S., Mehl, H., and Wagner, W., 2007, Detecting unknown coal fires: synergy of automated coal fire risk area delineation and improved thermal anomaly extraction: *International Journal of Remote Sensing*, v. 28, no. 20, p. 4561-4585.
- Kwon, S. H., 2004, Threshold selection based on cluster analysis: *Pattern Recognition Letters*, v. 25, no. 9, p. 1045-1050.
- Lacombe, O., Bellahsen, N., and Mouthereau, F., 2011, Fracture patterns in the Zagros simply folded belt (Fars, Iran): constraints on early collisional tectonic history and role of basement faults.: *geological Magazine*, p. 1-24.
- Lakkaraju, V. R., Zhou, X., Apple, M. E., Cunningham, A., Dobeck, L. M., Gullickson, K., and Spangler, L. H., 2010, Studying the vegetation response to simulated leakage of sequestered CO<sub>2</sub> using spectral vegetation indices: *Ecological Informatics*, v. 5, no. 5, p. 379-389.
- Lammoglia, T., and Filho, C., 2013, Unraveling Hydrocarbon Microseepages in Onshore Basins Using Spectral–Spatial Processing of Advanced Spaceborne Thermal Emission and Reflection Radiometer (ASTER) Data: *Surveys in Geophysics*, v. 34, no. 3, p. 349-373.
- Lammoglia, T., Filho, C., and Filho, R., 2008, Characterization of hydrocarbon microseepages in the Tucano basin (Brazil) through hyperspectral classification and neural network analysis of Advance Spaceborne Thermal Emission and Reflection Radiometer (ASTER) data *International Photogrammetry, Remote Sensing and Spatial Information Sciences*, v. 38.

- Lawrence, R., Bunn, A., Powell, S., and Zambron, M., 2004, Classification of remotely sensed imagery using stochastic gradient boosting as a refinement of classification tree analysis: *Remote Sensing of Environment*, v. 90, p. 331–336.
- Lawrence, R. L., and Wright, A., 2001, Rule-based classification systems using classification and regression tree (CART) analysis: *Photogrammetric Engineering and Remote Sensing*, v. 67, p. 1137–1142.
- Leifer, I., and Boles, J., 2005, Measurement of marine hydrocarbon seep flow through fractured rock and unconsolidated sediment: *Marine and Petroleum Geology*, v. 22, no. 4, p. 551-568.
- , 2006, Corrigendum to: Measurement of marine hydrocarbon seep flow through fractured rock and unconsolidated sediment: [*Marine and Petroleum Geology* 22 (2005), 551–558]: *Marine and Petroleum Geology*, v. 23, no. 3, p. 401.
- Link, W. K., 1952, Significance of oil and gas seeps in world oil exploration: *AAPG Bulletin*, v. 36, p. 1505-1541.
- Liu, X. M., Bloemendal, J., and Rolph, T., 1994, Pedogenesis and paleoclimate interpretations of the magnetic susceptibility record of Chinese loess-paleosol sequences: *Geology*, v. 22, p. 858-859.
- Louis, C., and etal, 2009, Sulphur stable isotopes can distinguish trophic dependence on sediments and plankton in boreal lakes: *Freshwater Biology*, v. 54, p. 1006-1015.
- Lu, D., and Weng, Q., 2007, A survey of image classification methods and techniques for improving classification performance: *International Journal of Remote Sensing*, v. 28, no. 5, p. 823-870.
- Lucier, A., Orkhonselenge, T., and Stein, A., 2004, Texture based segmentation for identification of geological units in remotely sensed imagery. : In: *Proceedings of the 3rd International Symposium on Spatial Data Quality ISSDQ'04*, Bruck an der Leitha, Austria, April 15-17th, 2004, p. 117-120.
- Maček, I., Pfanz, H., Francetič, V., Batič, F., and Vodnik, D., 2005, Root respiration response to high CO<sub>2</sub> concentrations in plants from natural CO<sub>2</sub> springs: *Environmental and Experimental Botany*, v. 54, no. 1, p. 90-99.
- MacGregor, D. S., 1993, Relationships between seepage, tectonics and subsurface petroleum reserves: *Marine and Petroleum Geology*, v. 10, no. 6, p. 606-619.
- Machel, H. G., 2001, Bacterial and thermochemical sulfate reduction in diagenetic settings - old and new insights: *Sedimentary Geology*, v. 140, p. 143-175.
- Maher, B. A., and Thompson, R., 1992, Paleoclimate significance of mineral magnetic record of the Chinese loess and paleosols: *Quaternary Research*, v. 37, p. 150-170.

- Mars, J. C., and Rowan, L. C., 2010, Spectral assessment of new ASTER SWIR surface reflectance data products for spectroscopic mapping of rocks and minerals: *Remote Sensing of Environment*, v. 114, no. 9, p. 2011-2025.
- Matthews, M. D., 1996, Hydrocarbon migration, A view from the top: In D.Shumacher and M.Abrams,ed, *Hydrocarbon migration and its near surface expression*, Tulsa, Oklahoma, The AAPG.
- McCoy, M., Blake, J., and Andrews, K., 2001, Detecting hydrocarbon seepage using hydrocarbon absorption bands of reflectance spectra of surface soils: *Oil & Gas Journal*.
- McIver , and Friedl, 2001, Estimating pixel-scale land cover classification confidence using nonparametric machine learning methods: *IEEE Transactions on Geoscience and Remote Sensing*, v. 39, p. 1959-1968.
- McQuillan, H., 1991, The role of basement tectonics in the control of sedimentary facies, structural patterns and salt plug emplacements in the Zagros fold belt of southwest Iran: *Journal of Southeast Asian Earth Sciences*, v. 5, no. 1-4, p. 453-463.
- Metternicht, G. I., 2003, Categorical fuzziness: a comparison between crisp and fuzzy class boundary modelling for mapping salt-affected soils using Landsat TM data and a classification based on anion ratios: *Ecological Modelling*, v. 168, no. 3, p. 371-389.
- Mikhail, E. M., and Gracie, G., 1981, *Analysis and Adjustment of Survey Measurements.*: Van Nostrand Reinhold Company, New York.
- Mobasher, K., and Babaie, H., 2007, Kinematic significance of fold- and fault-related fracture systems in the Zagros mountains, southern Iran: *Tectonophysics*, v. 451, p. 156-169.
- Moore, J. C., 1999, Fluid seeps at continental margins: *Margins Newsletter*, v. 4, p. 12-14.
- Motiei, H., 1993, *Stratigraphy of Zagros: Geological Survey of Iran (in Farsi)*, p. 536p.
- Noomen, M. F., Skidmore, A. K., van der Meer, F. D., and Prins, H. H. T., 2006, Continuum removed band depth analysis for detecting the effects of natural gas, methane and ethane on maize reflectance: *Remote Sensing of Environment*, v. 105, no. 3, p. 262-270.
- Noomen, M. F., van der Werff, H. M. A., and van der Meer, F. D., 2012, Spectral and spatial indicators of botanical changes caused by long-term hydrocarbon seepage: *Ecological Informatics*, v. 8, no. 0, p. 55-64.
- O'Berian, C. A. E., 1957, Salt diapirism in south Persia: *Geologie en Mijnbouw*, v. 19, p. 357-376.
- O'Brien, G. W., Lawrence, G. M., Williams, A. K., Glenn, K., Barrett, A. G., Lech, M., Edwards, D. S., Cowley, R., Boreham, C. J., and Summons, R. E., 2005, Yampi Shelf, Browse Basin, North-West Shelf, Australia: a test-bed for constraining hydrocarbon migration and seepage rates using combinations of 2D and 3D seismic data and multiple, independent

- remote sensing technologies: *Marine and Petroleum Geology*, v. 22, no. 4, p. 517-549.
- Osorio MT, Moloney AP, Schmidt O, and FJ., M., 2011, Multielement isotope analysis of bovine muscle for determination of international geographical origin of meat: *J Agric Food Chem.*, v. 59, no. 7, p. 3285-3294.
- Otsu, N., 1979, A threshold selection method from gray-level histograms: *IEEE TRANSACTIONS ON IMAGE PROCESSING*, v. 9, p. 62–66.
- Padwick, C., Deskevich, M., Pacifici, F., and Smallwood, S., 2010, *WorldView-2 Pan-Sharpener*: ASPRS 2010: Annual Conference San Diego, California, 2010.
- Penn, B. S., Gordon, A. J., and Wendlandt, R. F., 1993, Using neural networks to locate edges and linear features in satellite images: *Computers & Geosciences*, v. 19, no. 10, p. 1545-1565.
- Petrovic, A., Khan, S. D., and Chafetz, H. S., 2008, Remote detection and geochemical studies for finding hydrocarbon-induced alterations in Lisbon Valley, Utah: *Marine and Petroleum Geology*, v. 25, no. 8, p. 696-705.
- Petrovic, A., Khan, S. D., and Thurmond, A. K., 2012, Integrated hyperspectral remote sensing, geochemical and isotopic studies for understanding hydrocarbon-induced rock alterations: *Marine and Petroleum Geology*, v. 35, no. 1, p. 292-308.
- Pinet, N., Duchesne, M., Lavoie, D., Bolduc, A., and Long, B., 2008, Surface and subsurface signatures of gas seepage in the St. Lawrence Estuary (Canada): Significance to hydrocarbon exploration: *Marine and Petroleum Geology*, v. 25, no. 3, p. 271-288.
- Plaza, A., Benediktsson, J. A., Boardman, J. W., Brazile, J., Bruzzone, L., Camps-Valls, G., Chanussot, J., Fauvel, M., Gamba, P., Gualtieri, A., Marconcini, M., Tilton, J. C., and Trianni, G., 2009, Recent advances in techniques for hyperspectral image processing: *Remote Sensing of Environment*, v. 113, no. Supplement 1, p. S110-S122.
- Premo, L. S., 2004, Local spatial autocorrelation statistics quantify multi-scale patterns in distributional data: an example from the Maya Lowlands: *Journal of Archaeological Science*, v. 31, p. 855-866.
- Pu, R., and Landry, S., 2012, A comparative analysis of high spatial resolution IKONOS and WorldView-2 imagery for mapping urban tree species: *Remote Sensing of Environment*, v. 124, p. 516-533.
- Ridgeway, G., 2006, Generalized boosted regression model: Documentation on the R Package 'gbm', version 1.5-7. <http://www.i-pensieri.com/gregr/gbm.shtml>, accessed March 2008.
- Rowan, L. C., and Mars, J. C., 2003, Lithologic mapping in the Mountain Pass, California area using Advanced Spaceborne Thermal Emission and Reflection Radiometer (ASTER) data: *Remote Sensing of Environment*, v. 84, no. 3, p. 350-366.

- Rowan, L. C., Mars, J. C., and Simpson, C. J., 2005, Lithologic mapping of the Mordor, NT, Australia ultramafic complex by using the Advanced Spaceborne Thermal Emission and Reflection Radiometer (ASTER): *Remote Sensing of Environment*, v. 99, no. 1-2, p. 105-126.
- Rudkiewicz, J. L., Sherkati, S., and Letouzey, J., 2007, Evolution of Maturity in Northern Fars and in the Izeh Zone (Iranian Zagros) and Link with Hydrocarbon Prospectivity, *in* Lacombe, O., Roure, F., Lavé, J., and Vergés, J., eds., *Thrust Belts and Foreland Basins*, Springer Berlin Heidelberg, p. 229-246.
- Sabine, C., 1999, Remote sensing strategies for mineral exploration: In *Remote Sensing for Earth Sciences: Manual of Remote Sensing*, A.N. Rencz (Ed.), v. (New York: John Wiley and Sons, Inc), p. 375-447.
- Safari, H. O., Pirasteh, S., and Mansor, S. B., 2011, Role of the Kazerun fault for localizing oil seepage in the Zagros Mountain, Iran: an application of GiT: *International Journal of Remote Sensing*, v. 32, no. 1, p. 1-16.
- Salati, S., van Ruitenbeek, F. J. A., Carranza, E. J. M., van der Meer, F. D., and Tangestani, M. H., 2013, Conceptual modeling of onshore hydrocarbon seep occurrence in the Dezful Embayment, SW Iran: *Marine and Petroleum Geology*, v. 43, no. 0, p. 102-120.
- Salati, S., van Ruitenbeek, F. J. A., de Smeth, J. B., and van der Meer, F. D., 2012, Characterization of onshore hydrocarbon seeps - induced alterations in the Zagros oil fields. : powerpoint. Presented at: GRSG Geological Remote Sensing Group of the Geological Society meeting, December 11-13, London.
- Salati, S., van Ruitenbeek, F. J. A., van der Meer, F. D., Tangestani, M. H., and van der Werff, H., 2011, Lithological mapping and fuzzy set theory: Automated extraction of lithological boundary from ASTER imagery by template matching and spatial accuracy assessment: *International Journal of Applied Earth Observation and Geoinformation*, v. 13, no. 5, p. 753-765.
- Salisbury, J. W., D'Aria, D. M., and Sabins Jr, F. F., 1993, Thermal infrared remote sensing of crude oil slicks: *Remote Sensing of Environment*, v. 45, no. 2, p. 225-231.
- Saunders, D., Burson, K., and Thompson, C., 1999, Model for hydrocarbon microseepage and related near-surface alterations: *AAPG Bulletin*, v. 83, no. 1, p. 170-185.
- Schonlau, M., 2005, Boosted regression (boosting): An introductory tutorial and a Stata plugin: *Stata Journal*, v. 5, no. 3, p. 330-354.
- Schumacher, D., 1996, Hydrocarbon-induced alteration of soils and sediments, *in* D. Schumacher and M.A. Abrams, eds., *Hydrocarbon migration and near surface expression: AAPG Memoir 66*, p. 71-89.
- Schumacher, D., 2011, Petroleum Exploration in Environmentally Sensitive Areas: Opportunities for Geochemical and Non-Seismic Geophysical Methods: Adapted from oral presentation at AAPG International

- Conference and Exhibition, Calgary, Alberta, Canada, September 12–15, 2010. Search and Discovery Article #40681 (2011), Posted January 18, 2011.
- Sella, G. F., Dixon, T. H., and Mao, A., 2002, A model for recent plate velocities from space geodesy: *Journal of Geophysical Research*, v. 107, p. 11.11-11.30.
- Sepehr, M., and Cosgrove, J. W., 2002, The major fault zones controlling the sedimentation, deformation and entrapment of hydrocarbon in the Zagros fold-thrust belt, Iran: AAPG Annual Meeting, Houston, Texas, March 10-13.
- , 2004, Structural framework of the Zagros Fold-Thrust Belt, Iran: *Marine and Petroleum Geology*, v. 21, no. 7, p. 829-843.
- Serkan Öztan, N., and Lütfi Süzen, M., 2011, Mapping evaporate minerals by ASTER: *International Journal of Remote Sensing*, v. 32, no. 6, p. 1651-1673.
- Setudenhnia, A., and OB Perry, J. T., 1966, Gachsaran, Masjid Soleyman, Agha Jari, Asmari, Banar-E-Deylam, Haft Kel, and Lali geological compilation maps 1:100,000 scale (sheet 20641 E). Iranian oil operating companies (IOOC): Center National de la Recherche Scientifique, Paris.
- Sherkati, S., and Letouzey, J., 2004, Variation of structural style and basin evolution in the central Zagros (Izeh zone and Dezful Embayment), Iran: *Marine and Petroleum Geology*, v. 21, no. 5, p. 535-554.
- Sherkati, S., Molinaro, M., De Lamotte, D. F., and Letouzey, J., 2005, Detachment folding in the central and eastern Zagros fold belt (Iran): salt mobility, multiple detachment and late basement control: *Journal of Structural Geology*, v. 27, no. 9, p. 1680-1690.
- Shi, P., Fu, B., Ninomiya, Y., Sun, J., and Li, Y., 2012, Multispectral remote sensing mapping for hydrocarbon seepage-induced lithologic anomalies in the Kuqa foreland basin, south Tian Shan: *Journal of Asian Earth Sciences*, v. 46, no. 0, p. 70-77.
- Smith, K. L., Steven, M. D., and Colls, J. J., 2004, Use of hyperspectral derivative ratios in the red-edge region to identify plant stress responses to gas leaks: *Remote Sensing of Environment*, v. 92, no. 2, p. 207-217.
- Staez, K., Secker, J., Gao, B. C., Davis, C., and Nadeau, C., 2002, Radiative transfer codes applied to hyperspectral data for the retrieval of surface reflectance: *ISPRS Journal of Photogrammetry and Remote Sensing*, v. 57, no. 3, p. 194-203.
- Stephenson, B. J., Koopman, A., Hillgratner, H., Mc Quillan, H., Bourne, S., Noad, J. J., and Rawnsley, K., 2007, Structural and stratigraphic controls on fold related fracturing in the Zagros mountains, Iran: implications for reservoir development.: From : Lonergan, L., Jolly, R. J. H., Rawnsley, K. & Sanderson, D.J. (eds) *Fractured reservoirs*. Geological society, London, special publications, v. 270, p. 1-21.

- Stocklin, J., 1968, Structural history and tectonics of Iran. A review.: AAPG Bulletin, v. 52, p. 1229-1258.
- Tangestani, M. H., Mazhari, N., Agar, B., and Moore, F., 2008, Evaluating Advanced Spaceborne Thermal Emission and Reflection Radiometer (ASTER) data for alteration zone enhancement in a semi-arid area, northern Shahr-e-Babak, SE Iran: International Journal of Remote Sensing, v. 29, no. 10, p. 2833-2850.
- Tangestani, M. H., and Moore, F., 2001, Porphyry copper potential mapping using the weights-of-evidence model in a GIS, northern Shahr-e-Babak, Iran: Australian Journal of Earth Sciences, v. 48, no. 5, p. 695-701.
- Thomas, A. N., 1952, "Gach-i-turush" and associated phenomena in southwest Persia. V11 Convegno Nazionale Del Metano E Del Petrolio Taormina, section 1, preprint.
- Tsai, D. M., and Yang, C. H., 2005, A quantile-quantile plot based pattern matching for defect detection: Pattern Recognition Letters, v. 26, no. 13, p. 1948-1962.
- Tyree, S., Weinberger, K. Q., and Agrawa, K., 2011, Parallel Boosted Regression Trees for Web Search Ranking: International World Wide Web Conference Committee (IW3C2), v. March 28-April 1. Hyderabad, India.
- van der Meer, F., 2003, Bayesian inversion of imaging spectrometer data using a fuzzy geological outcrop model: International Journal of Remote Sensing, v. 24, no. 22, p. 4301-4310.
- van der Meer, F., 2004, Analysis of spectral absorption features in hyperspectral imagery: International Journal of Applied Earth Observation and Geoinformation, v. 5, no. 1, p. 55-68.
- van der Meer, F., van dijk, P., van der Werff, H., and Yang, H., 2002, Remote sensing and petroleum seepage: a review and case study: Terra Nova, v. 14, no. 1, p. 1-17.
- van der Meer, F. D., van der Werff, H. M. A., van Ruitenbeek, F. J. A., Hecker, C. A., Bakker, W. H., Noomen, M. F., van der Meijde, M., Carranza, E. J. M., Smeth, J. B. d., and Woldai, T., 2012, Multi- and hyperspectral geologic remote sensing: A review: International Journal of Applied Earth Observation and Geoinformation, v. 14, no. 1, p. 112-128.
- van der Werff, H., 2006, Knowledge-based remote sensing of complex objects: recognition of spectral and spatial patterns resulting from natural hydrocarbon seepages: PhD thesis, Utrecht university, Utrecht, The Netherlands.
- van der Werff, H., van der Meijde, M., Jansma, F., van der Meer, F., and Groothuis, G. J., 2008, A spatial-spectral approach for visualization of vegetation stress resulting from pipeline leakage: Sensors, v. 8, no. 6, p. 3733-3743.
- van der Werff, H., van Ruitenbeek, F., van der Meijde, M., van der Meer, F., de Jong, S., and Kalubandara, S., 2007, Rotation-Variant Template

- Matching for Supervised Hyperspectral Boundary Detection: *Geoscience and Remote Sensing Letters, IEEE*, v. 4, no. 1, p. 70-74.
- van Ruitenbeek, F. J. A., Debba, P., van der Meer, F. D., Cudahy, T., van der Meijde, M., and Hale, M., 2006, Mapping white micas and their absorption wavelengths using hyperspectral band ratios: *Remote Sensing of Environment*, v. 102, no. 3-4, p. 211-222.
- van Ruitenbeek, F. J. A., van der Werff, H. M. A., Hein, K. A. A., and van der Meer, F. D., 2008, Detection of pre-defined boundaries between hydrothermal alteration zones using rotation-variant template matching: *Computers & Geosciences*, v. 34, no. 12, p. 1815-1826.
- Vicente, L. E., and de Souza Filho, C. R., 2011, Identification of mineral components in tropical soils using reflectance spectroscopy and advanced spaceborne thermal emission and reflection radiometer (ASTER) data: *Remote Sensing of Environment*, v. 115, no. 8, p. 1824-1836.
- Wang, L., and Bai, J., 2003, Threshold selection by clustering gray levels of boundary: *Pattern Recognition Letters*, v. 24, no. 12, p. 1983-1999.
- Wang, S., Ge, F., and Liu, T., 2006, Evaluating Edge Detection through Boundary Detection: *EURASIP Journal on Applied Signal Processing*, v. Volume 2006 p. 1-15.
- Wang, Y., and Ding, X., 2000, Hydrocarbon Alteration Characteristics of Soils and Mechanism for Detection by Remote Sensing in East Sichuan Area, China: *Natural Resources Research*, v. 9, no. 4, p. 295-305.
- Warren, J. K., 2006, *Evaporites*: Springer. Germany.
- Washburn, L., Clark, J. F., and Kyriakidis, P., 2005, The spatial scales, distribution, and intensity of natural marine hydrocarbon seeps near Coal Oil Point, California: *Marine and Petroleum Geology*, v. 22, no. 4, p. 569-578.
- Wennberg, O. P., Azizzadeh, M., Aqrabi, A. A. M., Blanc, E., Brockbank, P., Lyslo, K. B., Pickard, N., Salem, L. D., and Svana, T., 2007, The Khaviz anticline: an outcrop analogue to giant fractured Asmari Formation reservoirs in SW Iran: From : Lonergan, L., Jolly, R. J. H., Rawnsley, K. & Sanderson, D.J. (eds) *Fractured reservoirs*. Geological society, London, special publications, v. 270, p. 23-42.
- Woodcock, C., and Gopal, S., 2000, Fuzzy set theory and thematic maps: accuracy assessment and area estimation: *Geographical information science*, v. 14, no. 2, p. 153-172.
- Worldview-3, 2013, Available online: <https://www.digitalglobe.com/downloads/WorldView3-DS-WV3-Web.pdf> (accessed on 24 May 2013).
- Wulder, M., and Boots, B., 1997, Local spatial autocorrelation characteristics of remotely sensed imagery assessed with the Getis statistic: *International Journal of Remote Sensing*, v. 19, no. 11, p. 2223 — 2231.

- Y. Mizutani, and Rafter, T. A., 1969, Oxygen isotopic composition of sulphates—Part 3. Oxygen isotopic fractionation in the bisulphate ion–water system: *New Zealand Journal of Science*, v. 12, p. 54-59.
- Yang, H., Zhang, J., Van Der Meer, F., and Kroonenberg, S. B., 1999, Spectral characteristics of wheat associated with hydrocarbon microseepage: *International Journal of Remote Sensing*, v. 20, no. 2-4, p. 807-813.
- , 2000, Imaging spectrometry data correlated to hydrocarbon microseepage: *International Journal of Remote Sensing*, v. 21, no. 1, p. 197-202.
- Zadeh, L., 1965, Fuzzy Sets: *Information and Control*, v. 8, p. 338-353.
- Zhang, G., Zheng, Z., Shen, X., Zou, L., and Huang, K., 2011, Remote sensing interpretation of areas with hydrocarbon microseepage in northeast China using Landsat-7/ETM+ data processing techniques: *International Journal of Remote Sensing*, v. 32, no. 21, p. 6695-6711.
- Zhang, J., Wagner, W., Prakash, A., Mehl, H., and Voigt, S., 2004, Detecting coal fires using remote sensing techniques: *International Journal of Remote Sensing*, v. 25, no. 16, p. 3193-3220.

*Bibliography*

---

## Summary

A hydrocarbon seep occurs where due to different pressure in the earth's subsurface, liquid or gaseous hydrocarbons escape to the surface through fractures in the rock and planes of weakness between geological layers. Natural hydrocarbon seeps have long been used in petroleum exploration methods. They are the ends of migration pathways, which may provide indications of the presence of subsurface reservoirs and give the first clues to petroleum producing areas. Many of the oil and gas fields around the world have been discovered as a result of drilling in seeping areas. On land, hydrocarbon seep-induced alteration has been widely studied by traditional techniques such as geochemical and geophysical analyses. These methods, however, are expensive, time consuming and only applicable to some observations collected in the field, mainly around drilled areas in an active petroleum field. Thus, they cannot be used for regional mapping of alterations and their variations related to different types of seeps and various host lithologies over a large area. The use of remote sensing in hydrocarbon seep studies may have two approaches; a regional view for supporting stratigraphic and structural interpretations in sedimentary basins and direct detection of spectral features of hydrocarbon seep related alteration at the surface. The latter is caused by the fact that reservoirs are not entirely sealed and hydrocarbons could escape, reach the surface, and cause alterations in soils, rocks, and vegetation.

The emphasis of this thesis is on the geological application of reflectance spectroscopy and multispectral image analyses for the detection of seep-induced alterations and the evaluation of petroleum basins. Integration the results obtained from remote sensing studies with geological and geochemical data would allow us to understand processes that caused alterations at the surface.

The spatial pattern and spatial distribution of oil/gas seeps and their associated alterations with geological features have been quantitatively studied. The results provided insights in the links between geological structures and two subsets of hydrocarbons seeps and (b) the probability of spatial association of different geological features with two sub-sets of seeps. Two potential geological formations were chosen for subsequent field and laboratory studies.

Analyses the spectral and chemical characteristics of alteration induced by hydrocarbon seep from field data aided in (a) getting a better understanding of oil and gas migration through the stratigraphy in relation to the various types of seeps in the Zagros belt and (b) investigating the potential of detection of hydrocarbon seep-induced alteration for petroleum explorations. The field observations showed that the mineral composition of the cap rock influenced the type of seep occur at the surface and the density of seeps in the stratigraphy. The results of field and lab analyses helped us to select the best suitable test

area for image processing and to extract end-members from field observations to aid in image processing.

Boundaries between zones of compositional variations within evaporite cap rock in the Zagros petroleum system were mapped using ASTER imagery. Gas-induced alteration was detected using the WorldView-2 and ASTER imageries. Various image processing and statistical analyses of the two datasets captured the alteration zones and delineated areas that potentially host gas seeps.

The outcomes of this research demonstrated that the application of remote sensing studies of hydrocarbon seep in the oil and gas industry could be widened by basin interpretations at a regional scale. Understanding the relationship between hydrocarbon seeps and geology provides information about petroleum basins, particularly about the influence of compositional variation within the cap rock formation on the types of seeps occurring at the surface and movement of hydrocarbons in the stratigraphy. Such studies provide a framework for identifying permeable zones and evaluating the efficiency of cap rocks related to petroleum systems, which has implications for petroleum reservoir exploration.

## Samenvatting

Wanneer door drukverschillen in de ondergrond vloeibare of gasvormige koolwaterstoffen zich verplaatsen en via breuken en barsten aan het aardoppervlak ontsnappen, spreekt men van koolwaterstofsijpelingen. Natuurlijke koolwaterstofsijpelingen zijn veel gebruikt in de exploratie van aardolie en gas. Zij vormen de eindpunten van migratiepaden en ze geven mogelijke aanwijzingen over voorkomens van olie en gas reservoirs in de ondergrond. Veel olie en gasvelden op aarde zijn ontdekt door het boren in gebieden waar koolwaterstoffensijpelingen aan het aardoppervlak aanwezig waren. Chemische en mineralogische omzettingenzones, die gepaard gaan met koolwaterstofsijpelingen, zijn in het verleden bestudeerd met traditionele geochemische en geofysische methodes en gebruikt voor exploratie. Deze traditionele methodes zijn echter duur, tijdrovend en voornamelijk toepasbaar op gegevens die verzameld zijn in het veld nabij boorlocaties en in petroleum producerende velden. Zij zijn minder geschikt voor het op regionale schaal karteren van deze omzettingen.

Satellietbeelden kunnen op twee manieren gebruikt worden voor de bestudering van koolwaterstofsijpelingen; ze verschaffen een regionaal beeld voor de interpretaties van stratigrafie en structuren van sedimentaire bekkens en ze geven directe aanwijzingen voor de aanwezigheid van omzettingen die gerelateerd zijn aan het voorkomen van koolwaterstoffen aan het aardoppervlak. De laatste is het gevolg van het feit dat reservoirs niet volledig afgesloten zijn en dat koolwaterstoffen uit reservoirs lekken en aan het oppervlak omzettingen vormen van bodems en gesteenten en vegetatie beïnvloeden.

De nadruk in dit proefschrift ligt op de geologische toepassing van reflectie spectroscopie en multispectrale beeldanalyse voor de detectie van door sijpelingen veroorzaakte omzettingen en de evaluatie van sedimentaire bekkens voor petroleum voorkomens. Integratie van de gegevens, die verkregen zijn met behulp van satellietbeelden, met geologische en geochemische grondgegevens verschafte ons een beter begrip van de omzettingsprocessen aan het aardoppervlak.

De ruimtelijke patronen van olie- en gassijpelingen en hun omzettingen en de aan de voorkomens gerelateerde geologische karakteristieken zijn kwantitatief bestudeerd. De resultaten verstrekten inzicht in (a) de verbanden tussen geologische structuren en de typen van koolwaterstofsijpelingen en ( b ) de ruimtelijke samenhang tussen verschillende geologische kenmerken en de verschillende typen van sijpelingen. Twee geologische formaties werden op basis van deze analyses gekozen voor verdere veld- en laboratoriumstudies.

Analyse van de spectrale en chemische kenmerken van de door koolwaterstofsijpelingen geïnduceerde omzettingen hielpen in (a) het verkrijgen

van een beter begrip van olie en gas migratie door de stratigrafie in het Zagros gebied in relatie tot de verschillende typen sijpelingen en (b) het onderzoeken van de mogelijkheid tot detecteren van aan sijpelingen gerelateerde omzettingen voor olie en gas exploratie. Uit de veldgegevens bleek dat de mineralogische samenstelling van de deklaag boven een petroleum reservoir van invloed was of het type van de doorsijpeling aan het aardoppervlak en de hoeveelheid sijpelingen in de stratigrafie. De resultaten van de veld en laboratorium analyses hielpen ons om het meest geschikte test gebied voor beeldanalyse te selecteren en om mineraal spectra te selecteren voor beeldclassificatie.

Grenzen tussen gesteenten met een verschillende mineralogische samenstelling binnen de uit evaporieten bestaande afsluitende formaties in de petroleum systemen in het Zagros gebied, zijn in kaart gebracht met behulp van ASTER satellietbeelden. Door gas geïnduceerde omzettingen werden gedetecteerd met behulp van zowel ASTER als WoldView-2 satellietbeelden. Met behulp van diverse beeldverwerkings- en statistische technieken werden omzettingszones geïdentificeerd en werden nieuwe gebieden ontdekt waar mogelijk gassijpeling plaatsvindt.

De uitkomsten van dit onderzoek hebben aangetoond dat de toepassing van satellietbeelden door de olie-en gasindustrie voor de detectie van koolwaterstof sijpelingen kan worden uitgebreid met bekken interpretaties op regionale schaal. Het begrip van de relatie tussen koolwaterstofsijpelingen en geologie geeft informatie over aardolie bekkens, met name over de invloed van mineralogische en chemische samenstelling van de deklaagformaties op de soorten sijpelingen aan het aardoppervlak en de migratie van koolwaterstoffen door de stratigrafie. Dergelijke studies verschaffen een raamwerk voor de bepaling van permeabele zones en de efficiëntie van afsluitende formaties in petroleum systemen en hebben daardoor implicaties voor de exploratie van petroleum reservoirs.

## Biography



Sanaz Salati was born on March 05, 1979 in Tehran, Iran. She studied geology at the Tabriz University, Iran, and received a BSc in 2003. From 2003 to 2006 she studied Economic Geology at the University of Shiraz, Iran. Her MSc research focused on the urban geochemistry of the Shiraz. In 2007, she was awarded a scholarship from science and technology ministry of Iran to study a PhD in economic geology at the University of Shiraz. From 2007 to 2009 she studied the urban geochemistry of the Shiraz as well as collaborating in several research projects. In March 2009, she started her PhD research at the faculty of Geo-Information science and Earth Observation (ITC), University of Twente, with the scholarship from the European Union (Erasmus Mundus

program). Her PhD research aimed at characterization and remote detection of onshore hydrocarbon-seep induced alteration. Her main research interests are mineral and petroleum exploration, geochemistry, and application of remote sensing and GIS in earth sciences.

## Publications

### ISI journals

[1] **Sanaz Salati**, Frank J.A. van Ruitenbeek, Emmanuel John M. Carranza, Freek D. van der Meer, Majid Hashemi Tangestani. (2013) Conceptual modeling of onshore hydrocarbon seep occurrence in the Dezful Embayment, SW Iran. *Marine and Petroleum Geology*.43:102-120.

[2] **Sanaz Salati**, Frank J.A. van Ruitenbeek, Boudewijn de Smeth, Freek D. van der Meer. (2013), Spectral and chemical characterizations of onshore hydrocarbon seep-induced alterations in the Dezful Embayment, SW Iran. *American Association of Petroleum Geologist (AAPG Bulletin)*. (Accepted)

[3] **Sanaz Salati**, Frank van Ruitenbeek, Freek van der Meer, Babak Naimi. (2013), detection of alteration induced by onshore gas seep from ASTER and

WorldView-2 data. Remote Sensing-an open access journal (under review after revision)

[4] **Sanaz Salati**, Frank J.A. van Ruitenbeek, Freek D. van der Meer, Majid Hashemi Tangestani, Harald van der Werff. (2011), Lithological mapping and fuzzy set theory: automated extraction of lithological boundary from ASTER imagery by template matching and spatial accuracy assessment. International Journal of Applied Earth Observation and Geoinformation. 13: 753-765

[5] **Salati. S**, Moore. F. (2010), Assessment of heavy metal concentration in the Khoshk river water and sediment, Shiraz, Southwest Iran. Environmental monitoring and assessment. 164: 677- 689.

[6] **Sanaz Salati**, Frank J.A. van Ruitenbeek, Freek D. van der Meer. (2014). Remote sensing of hydrocarbon seep-induced alteration in onshore basins: a review: Terra Nova (**In preparation**)

### **Conference full paper**

**Sanaz Salati**, Frank J.A. van Ruitenbeek and Freek D. van der Meer. (2011). Spatial association of hydrocarbon seeps with geological features. In: Mathematical geosciences at the crossroads of theory and practice: proceedings of the IAMG 2011 : annual conference of the International Association for Mathematical Geosciences : 5-9 September 2011, Salzburg, Austria. / ed. by. R. Marschallinger and F. Zobl. Salzburg: IAMG, 2011. pp 998-1009.

### **Presentations**

[1] **Sanaz Salati**, Frank J.A. van Ruitenbeek, J. Boudewijn de Smeth, Freek D. van der Meer. (2012). Spectral and chemical characterizations of onshore hydrocarbon seeps-induced alterations in evaporite and marly limestone Formations: proceedings of the GRSG 2012, annual meeting of the Geological Remote Sensing Group:11-13 December 2012, London, England.

[2] **Sanaz Salati**, Farid Moore. (2009). Assessment of Heavy Metal Concentration in the Khoshk River Sediment, Shiraz, SW Iran, 6th European Congress on Regional Geoscientific Cartography and Information System, Munich, Germany.

[3] Moore. F, **Salati .S**. (2006) Urban geochemistry of khoshk river, Shiraz, Iran. The 7th international symposium on environmental geochemistry, Bijing, China, 25:19.

[4] Moore. F, **Salati .S. (2006)**. Investigation of heavy metals in Khoshk River by statistical method, Shiraz, Iran. Proceeding of international symposium of statistic, Shiraz, Iran (in Persian).

**ITC Dissertation List**

[http://www.itc.nl/research/phd/phd\\_graduates.aspx](http://www.itc.nl/research/phd/phd_graduates.aspx)